January 2010

Optical-Resolution Photoacoustic Microscopy

Song Hu
Washington University in St. Louis

WASHINGTON UNIVERSITY IN ST. LOUIS

School of Engineering and Applied Science

Department of Biomedical Engineering

Dissertation Examination Committee:
Lihong V. Wang, Chair
Jeffrey M. Arbeit
Dennis L. Barbour
Igor R. Efimov
Jin-Moo Lee
Younan Xia

OPTICAL-RESOLUTION PHOTOACOUSTIC MICROSCOPY

by

Song Hu

A dissertation presented to the
Graduate School of Arts and Sciences
of Washington University in
partial fulfillment of the
requirements for the degree
of Doctor of Philosophy

December 2010

Saint Louis, Missouri

ABSTRACT

Optical microscopy, providing valuable biomedical insights at the cellular and organelle levels, has been widely recognized as an enabling technology. Mainstream optical microscopy technologies, including single-/multi-photon fluorescence microscopy and OCT, have demonstrated extraordinary sensitivities to fluorescence and optical scattering contrasts, respectively. However, the optical absorption contrast of biological tissues, which encodes essential physiological/pathological information, has not yet been fully assessable.

The emergence of biomedical photoacoustics has led to a new branch of optical microscopy—OR-PAM. As a valuable complement to existing optical microscopy technologies, OR-PAM detects optical absorption contrasts with exquisite sensitivity (i.e., 100%). Combining OR-PAM with fluorescence microscopy or optical-scattering-based OCT (or both) provides comprehensive optical properties of biological tissues. Moreover, OR-PAM encodes optical absorption into acoustic waves, in contrast to the pure optical processes in fluorescence microscopy and OCT, and thus provides background-free detection. The acoustic detection in OR-PAM mitigates the impacts of optical scattering on signal degradation and naturally eliminates possible interferences (i.e., crosstalks) between excitation and detection, which is a common problem in fluorescence microscopy due to the overlap between the excitation and fluorescence spectra and imperfect extinction of the filter. Unique for high-resolution imaging of optical absorption, OR-PAM has demonstrated broad biomedical applications in fields such as neurology, ophthalmology, vascular biology, and dermatology. My doctoral research

focuses on developments and biomedical applications of OR-PAM.

The first part of my dissertation discusses the development of three generations of OR-PAM towards high-resolution, high-sensitivity, high-speed, and wide FOV *in vivo* imaging. In this section, I provide a comprehensive description of OR-PAM, including the principle, system design, system configuration, experimental procedures, laser safety, functional imaging scheme, and example biomedical applications at a variety of *in vivo* anatomical sites (i.e., skins, eyes and brains).

The second part of my dissertation focuses on the application of OR-PAM in vascular biology, with an emphasis on neovascularization. In this section, I demonstrate longitudinal OR-PAM monitoring of the morphological (i.e., vessel diameter, length, tortuosity and volume) and functional (i.e., sO_2) changes of angiogenic microenvironment at the capillary level, in both a non-disease TetON-HIF-1 transgenic mouse model and a cancer xenograft model in mouse ear.

The last part of my dissertation focuses on the application of OR-PAM in neurology, with an emphasis on cortical stimulation, Alzheimer's disease, and ischemic stroke. In this section, I use label-free OR-PAM for both acute monitoring of microvascular responses to direct electrical stimulations of the mouse somatosensory cortex through a cranial opening and longitudinal monitoring of the morphological and functional changes of cortical vasculature in a transient middle cerebral artery occlusion mouse model. I also explore the potential of OR-PAM for transcranial monitoring of amyloid plaque growth in an AD mouse model.

ACKNOWLEDGMENTS

I wish to express my sincere gratitude to my advisor, Dr. Lihong Wang, for his support, guidance, encouragement, and countless time he has spent for me through all my years as a graduate student. Without his constructive advice and discussion, I would not have accomplished this work.

I would like to thank my committee members, Dr. Jeffrey Arbeit, Dr. Dennis Barbour, Dr. Igor Efimov, Dr Jin-Moo Lee, and Dr. Younan Xia, for their invaluable advice on my research. Specially, I thank Dr. Jeffrey Arbeit and Dr Jin-Moo Lee for their great supports and guidance on applying OR-PAM for vascular biology and neurology studies. I also thank Dr. Dennis Barbour for his valuable advice on our brain stimulation study.

I am grateful to Dr. Konstantin Maslov, who has been a mentor, a colleague, and a friend throughout my PhD study. Without his ingenious design and generous instruction, this dissertation would not be possible. I am also grateful to my colleagues and collaborators, Dr. Geng Ku, Dr. Christopher Favazza, Dr. Vassiliy Tsytsarev, Dr. Bin Rao, Dr. Ping Yan, Ernie Gonzales, Sunday Oladipupo, Rebecca Sohn, Andrea Santeford, Xin Cai, and Junjie Yao for their considerable assistance. I also thank to Dr. Hao Zhang, Dr. Xinmai Yang, Liang Song, Yu Wang, Zijian Guo and other lab members for their fruitful discussions and friendship.

I appreciate my loving family in China for their endless support and love.

Finally, my one true love, Yu Zhang, deserves far more credit than I can give her.

DEDICATION

To my wife Yu Zhang, my parents, and my parents in law,

for their true love and support.

TABLE OF CONTENTS

ABBREVIATIONS

2-D:	Two-dimensional
3-D:	Three-dimensional
AD:	Alzheimer's disease
ADM:	Adrenomedullin
ANSI:	American National Standards Institute
APP/PS1:	APPswe/PS1dE9
AR-PAM:	Acoustic-resolution photoacoustic microscopy
B-scan:	Cross-sectional scan
CAIX:	Carbonic anhydrase IX
CP:	Ciliary process
cpm:	Cycles-per-min
CT:	Computed tomography
CW:	Continuous-wave
D-OCT	Doppler optical coherence tomography
DOT:	Diffuse optical tomography
DOX:	Doxycycline
DTG:	Double transgenic
FOV:	Field of view
FWHM:	Full-width-at-half-maximum
G1:	First-generation
G2:	Second-generation

G3:	Third-generation
GLUT1:	Glucose transporter-1
HbO_2:	Oxyhemoglobin
HbR:	Deoxyhemoglobin
HbT:	Total hemoglobin concentration
HIF:	Hypoxia-inducible factor
IB4:	Isolectin B4
ICG:	Indocyanine green
ISI:	Intrinsic signal imaging
IVM:	Intravital microscopy
LIC:	Lesser iris circles
L-PAM:	Longitudinal photoacoustic microscopy
MAP:	Maximum amplitude projection
MCA:	Middle cerebral artery
MIC:	Major iris circle
MPE:	Maximum permissible exposure
MRI:	Magnetic resonance imaging
NA:	Numerical aperture
NIR:	Near-infrared
NTG:	Nontransgenic
OCT:	Optical coherence tomography
OPS:	Orthogonal polarization spectral
OR-PAM :	Optical-resolution photoacoustic microscopy

PACT: Photoacoustic computed tomography

PAD: Photoacoustic Doppler

PAM : Photoacoustic microscopy

PAT: Photoacoustic tomography

PET: Positron emission tomography

PRF: Pulse repetition frequency

RBC: Red blood cell

RCB: Recurrent choroidal branch

RIA: Radial iris arteries

ROI: Region of interest

SNR: Signal-to-noise ratio

sO_2: Hemoglobin oxygen saturation

TPM: Two-photon microscopy

VE-Cadherin: Vascular endothelial-cadherin

VSDI: Voltage-sensitive dye imaging

Y^{1173}: Phosphorylated

αSMA: Alpha-smooth muscle actin

γH2AX: Gamma histone H2AX

I. INTRODUCTION

1. Background and motivation*

The past two decades have witnessed a dramatic growth in biomedical applications of optical microscopy. Mainstream microscopy technologies—including, but not limited to, confocal microscopy, multiphoton microscopy, and OCT—have greatly benefited from advances in laser technology, fluorescent labeling, scanning mechanisms, and image acquisition. However, all these technologies rely on either optical scattering or fluorescent contrast and have fundamental limitation in assessing optical absorption properties of biological tissues.[1]

The recent emergence of biomedical photoacoustics provides a promising solution for optical absorption imaging. In photoacoustics, biological tissues absorb short-pulsed or intensity-modulated optical irradiation, induce transient temperature rise, and further generate high-frequency ultrasonic waves. Photoacoustics provides an exquisite way to resolve the optical absorption distribution in biological tissue ultrasonically, leading to a new branch of optical microscopy—PAM. In PAM, the dual foci of optical excitation and ultrasonic detection are configured coaxially and confocally to maximize the imaging sensitivity. Thus, the lateral resolution of PAM is determined by the product of the two point spread functions. Taking advantage of the deep-focusing capability of ultrasound (ultrasonic scattering in tissues is 1,000 times weaker than optical scattering), AR-PAM with tight acoustic focusing and weak optical focusing has been developed for high-resolution deep tissue imaging in the optical quasidiffusive or diffusive regime (Fig. 1A).[2, 3] Although having achieved great success, AR-PAM is inadequate for examining

* Modified with permission from S. Hu, K. Maslov, and L. V. Wang, "Three-dimensional optical-resolution photoacoustic microscopy," in *Biomedical Optical Imaging Techniques: Design and Applications*, J. M. Zavislan and R. Liang, Ed., Springer (under review).

the anatomy and function of biological tissues at the cellular or subcellular level. To fill this gap, we have developed OR-PAM (Fig. 1B), where the diffraction-limited optical focus predominates over the acoustic focus to improve the lateral resolution of PAM from 45 μm (acoustical) to 5 μm or even better (optical).[4] As shown in Fig. 1, OR-PAM can clearly resolve single capillaries in an adult mouse brain through the intact skull (Fig. 1D), while AR-PAM can only resolve cortical vessels thicker than 45 μm (Fig. 1C). However, the weak ultrasonic scattering allows AR-PAM to penetrate both the scalp and the skull, while OR-PAM requires the scalp to be removed.

As a unique optical absorption microscopy technology and a valuable complement to the existing technologies, OR-PAM has demonstrated broad biomedical applications.[5-11] Taking advantage of the strong optical absorption of endogenous hemoglobin, OR-PAM enables label-free, noninvasive, volumetric microvascular imaging down to single capillaries, providing both anatomical (such as vessel diameter, connectivity, and tortuosity) and functional (such as sO_2 and blood flow) information.[5-8, 12] With the aid of exogenous molecular contrast agents, OR-PAM is also capable of molecular imaging.[10]

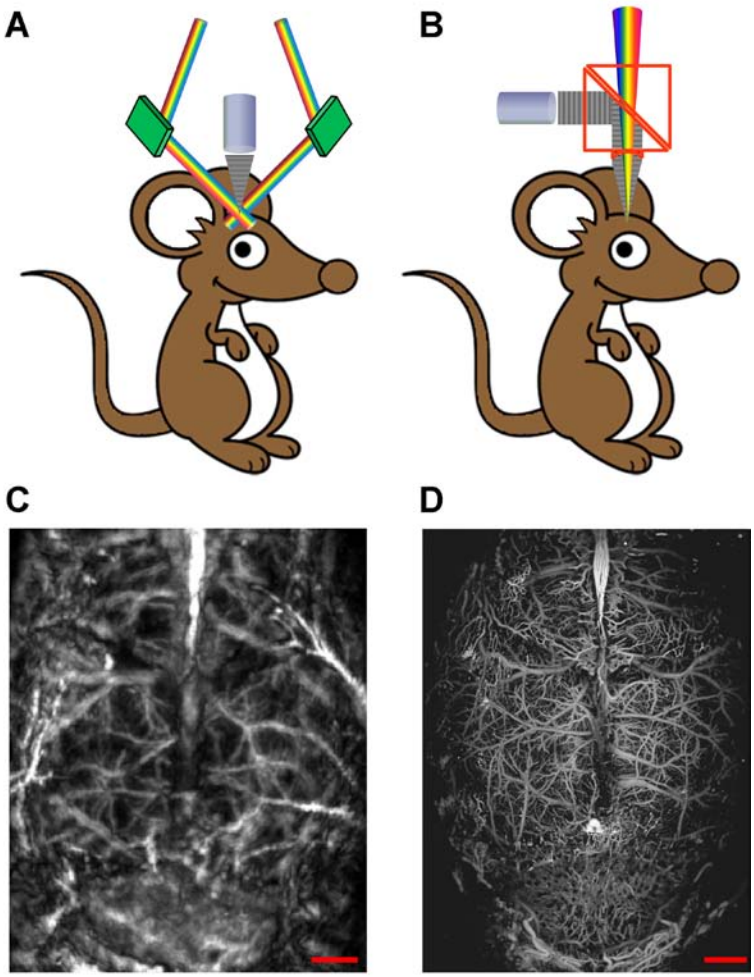

Fig. 1. Comparison of AR-PAM and OR-PAM. (A) Schematic of AR-PAM. (B) Schematic of OR-PAM. (C) AR-PAM image of the cortical vasculature in a living adult mouse with both the scalp and the skull intact. (D) OR-PAM image of the cortical vasculature in a living adult mouse with the scalp removed and the skull intact. Scale bars: 1 mm.

2. Dissertation outline

In Chapter II, I reviewed the development of three generations of OR-PAM, towards high-resolution, high-sensitivity, high-speed, and wide FOV *in vivo* imaging. Our G1 OR-PAM designed and implemented in 2007 has demonstrated, for the first time, *in vivo,*

label-free, noninvasive imaging of single capillaries.[4] Excellent spatial resolution (5 μm lateral and 15 μm axial) and adequate tissue penetration (>0.7 mm) have found G1 OR-PAM broad biomedical applications in such fields as neurology,[10, 13] ophthalmology,[8] and vascular biology[5-7] since its invention. However, the acoustic detection in G1 OR-PAM suffers significant loss.[10] Moreover, the G1 system could cover only a small FOV within a reasonable acquisition time because translating the living object for scanning must be slow enough to avoid possible disturbance to the object. In 2009, we invented G2 OR-PAM with improved detection sensitivity and imaging speed. In G2 OR-PAM, we designed a novel optical-acoustic combiner, which improves the detection sensitivity by 18.4 dB over the G1 system. Moreover, the optical-fiber-based light delivery allows scanning the imaging head rather than the living object, thereby enabling fast *in vivo* imaging (5 times as fast as the G1 system) over a large FOV (centimeters along the lateral dimensions). More valuably, instrument-scanning extends the scope of G2 OR-PAM to objects that are impractical to move mechanically for scanning (e.g., humans). Although G2 OR-PAM has a significant improvement on imaging speed over the G1 system, its maximum B-scan rate (<3 frames/s) is still far from real time. Such imaging speed is not yet adequate to catch acute microhemodynamics in such as neurovascular coupling. Recently, we developed G3 OR-PAM with combined optical-scanning and mechanical-scanning. While maintaining the large FOV made possible by mechanical scanning, G3 OR-PAM offers the option of real-time optically scanning a small ROI to visualize acute microhemodynamics and cell trafficking. Moreover, optical scanning can be potentially hybrid with mechanical scanning for high-speed, wide FOV imaging.

Chapter III focuses on the application of OR-PAM in vascular biology, with an

emphasis on neovascularization. There is a lack of methodology that combines conditional genetic approaches with longitudinal, noninvasive, label-free microvascular imaging for the study of adult neovascularization. In this section, we successfully applied OR-PAM to longitudinally study engineered adult neovascularization in a disease-free TetON-HIF-1 transgenic mouse model, wherein DOX induction of an oxygen insensitive HIF-1 mutant was targeted to basal keratinocytes using a keratin 5-rtTA driver. OR-PAM produced longitudinal images of the same microvascular network undergoing capillary angiogenesis and trunk vessel remodeling over 60-day continuous angiogenic stimulus with and without perturbations to the angiogenic pathways (e.g., VEGF receptor immunoblocking and VEGF gene deletion). Moreover, the image extraction capability of OR-PAM enabled quantitatively analyzing the sensitivity of differential microvessel subset (capillary vs. trunk vessel) to antiangiogenesis therapy and the stage-specific resistance to that treatment. OR-PAM also serially imaged capillary and terminal arteriolar and venular regression following HIF-1 withdrawal, providing unprecedented real-time images of luminal constriction and microvessel dropout. The excellent agreement between data from the noninvasive, *in vivo* OR-PAM and the "gold standard", invasive, *ex vivo* histology procedures validated, for the first time, the accuracy of OR-PAM for quantitative, functional microvascular imaging. As a valuable extension, I also reported some preliminary study on a disease model with cancer xenografts in mouse ears.

Chapter IV focuses on the application of OR-PAM in neurology, with an emphasis on cortical stimulaton, Alzheimer's disease, and ischemic stroke. First, we explored the potential of OR-PAM for longitudinal monitoring of amyloid plaque growth in an AD mouse model. Validation using conventional fluorescence microscopy and

multiphoton microscopy shows that OR-PAM has sufficient sensitivity and spatial resolution to identify amyloid plaques in living mouse brains through a cranial window. In addition, with dual-wavelength OR-PAM, the 3-D morphology of amyloid plaques and the surrounding microvasculature are imaged simultaneously without angiographic contrast agents. However, transcranial imaging of amyloid plaque growth requires further optimization of imaging parameters and improvements in the optical absorption of amyloid-specific dyes. Second, we demonstrated the potential of OR-PAM in the field of neurovascular coupling by studying microvascular responses to direct electrical stimulations of the mouse somatosensory cortex. We observed two forms of responses (vasoconstriction and vasodilatation) and the stimulation-variation-induced transition between these two forms. We also observed a marked correlation between the current-dependent responses of two daughter vessels bifurcating from the same parent vessel. Statistical analysis of twenty-seven vessels from three different animals further characterized the spatial-temporal features and the current dependence of the microvascular response. As a valuable extension, I also reported some preliminary study on ischemic stroke in a transient MCA occlusion mouse model.

Finally, in the Chapter V, the summary of my dissertation work is presented.

II. OR-PAM: SYSTEMS AND EXAMPLE BIOMEDICAL APPLICATIONS

1. G1 OR-PAM*

1.1 Introduction

The advantages of PAM over traditional optical and ultrasonic imaging include primarily the detection of endogenous optical absorption contrast at ultrasonic resolutions.[3, 14] In PAM, a pulsed laser beam is weakly focused into the biological tissue to produce emission of ultrasonic waves due to thermal expansion of the medium caused by absorbed laser radiation. The ultrasonic waves are then detected with a focused ultrasonic transducer to form high-resolution volumetric images. Among the existing photoacoustic imaging technologies, the spatial resolutions depend almost solely on the ultrasonic parameters including the frequency and the NA. For example, in the recently developed dark-field confocal PAM, a lateral resolution of 50 μm was achieved with a center frequency of 50 MHz and an NA of 0.44.[2] This resolution is adequate for many biomedical applications.[14, 15] However, to resolve smaller structures such as capillaries, which are 4–9 μm in diameter,[16] higher spatial resolution is required.

If both the lateral and axial resolutions are provided ultrasonically, the imaging penetration is limited by the frequency-dependent ultrasonic attenuation in tissue. For example, a 5-μm lateral resolution requires an ultrasonic center frequency greater than 300 MHz. At such a high frequency, the ultrasonic attenuation (~20 dB/mm in water and ~80 dB/mm in tissue) limits the penetration depth to ~100 μm, which is less than that of optical confocal microscopy. An alternative is to use fine optical focusing to provide the lateral resolution while the axial resolution is still derived from time-resolved ultrasonic

* Reprinted with permission from K. Maslov†, H. F. Zhang†, S. Hu†, and L. V. Wang, "Optical-resolution photoacoustic microscopy for *in vivo* imaging of single capillaries," Opt. Lett. 33, 929–931 (2008). † Authors contributed equally to this work.

detection. We refer to this alternative technology as OR-PAM. Although having a comparable depth penetration limit with existing high-resolution optical imaging modalities (including optical confocal microscopy, two-photon microscopy, and OCT), OR-PAM is primarily sensitive to optical absorption contrast, whereas the other modalities are dominantly sensitive to optical scattering or fluorescence contrast.

1.2 Materials and Experiments

Our OR-PAM system (Fig. 2) employs optical focusing to achieve μm-level lateral resolution. A dye laser pumped by an Nd:YLF laser is used as the irradiation source. Laser pulses (pulse duration: 7 ns) from the dye laser are spatially filtered by a 25-μm-diameter pinhole. The pinhole is then imaged to a diffraction-limited focal spot with a diameter of 3.7 μm by an objective lens (NA: 0.1; depth of focus: ~40 μm). The laser pulse energy after the objective lens is measured to be 100 nJ. Ultrasonic focusing is achieved through a plano-concave lens (radius of curvature: 5.2 mm; aperture: 6.4 mm; NA in water: 0.46) and the ultrasonic focal diameter is 27 μm. The optical objective lens and the ultrasonic transducer are configured coaxially and confocally as shown in Fig. 2.

Combination of time-resolved detection of the photoacoustic waves with a 2-D raster scanning along the *x*-*y* plane generates a volumetric image,[15] which can be viewed through direct volumetric rendering, B-scan images, or MAP images.[15]

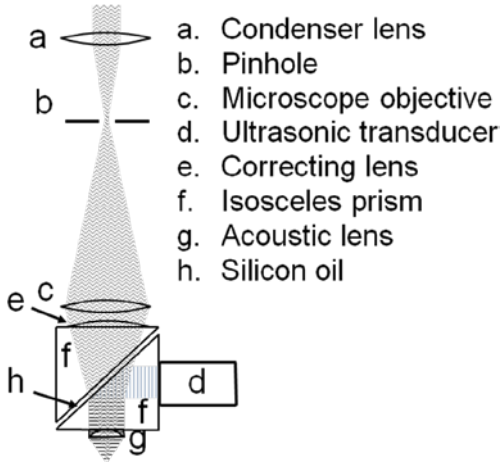

Fig. 2. Schematic of the OR-PAM system.

1.3 Results and Discussion

The imaging depth of the OR-PAM system was measured by imaging two horse hairs (diameter: 200 μm) separately placed above and below a piece of freshly harvested rat scalp. An OR-PAM image (Fig. 3A) was acquired with 32 times signal averaging at the optical wavelength of 630 nm. Both hairs are clearly visible. The B-scan image (Fig. 3B) shows that the bottom hair is 700 µm deep in the tissue. Therefore, the imaging penetration limit is at least 700 µm.

The axial resolution was estimated to be 15 μm based on the measured transducer bandwidth (100 MHz in receiving-only mode) and the speed of sound in tissue (1.5 mm/μs). The lateral resolution of the OR-PAM system was experimentally estimated by imaging an Air Force resolution test target (USAF-1951, Edmund) immersed in an optically clear medium. Images were acquired at the optical wavelength of 590 nm without signal averaging. In Fig. 3C, the highlighted well-resolved bars (group 6, element 5) have gaps of 4.9 µm (spatial frequency: 102 mm^{-1}; modulation transfer function value: 0.65). Other pairs of spatial frequency and modulation transfer function values are 64

mm^{-1} with 0.95 and 80 mm^{-1} with 0.8. Nonlinearly fitting the modulation transfer function followed by extrapolation yields a lateral resolution of 5 μm, which is 30% greater than the diffraction limit of 3.7 μm. As a further illustration of the lateral resolution, an MAP image of a 6-μm-diameter carbon fiber immersed in water is shown in Fig. 3D. The mean FWHM value of the imaged fiber is estimated to be 9.8 μm, which is 3.8 μm wider than the fiber diameter and hence in agreement with the 5-μm resolution. Since the lateral resolution is expected to deteriorate with imaging depth due to optical scattering, a 6-μm-diameter carbon fiber covered by a 0.2-mm-thick nude mouse ear is imaged. The photoacoustic amplitude profile of a cross section of this carbon fiber is shown in Fig. 3E. The FWHM value of the imaged fiber is estimated to be 10 μm. Hence OR-PAM maintains ~5 μm lateral resolution in tissue up to at least 0.2 mm depth.

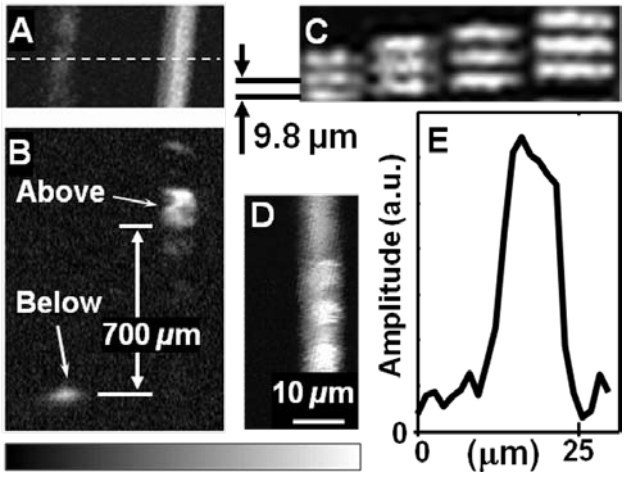

Fig. 3. Imaging depth and lateral resolution of the OR-PAM system. (A) MAP image of two horse hairs placed above and below a piece of rat skin. (B) B-scan image at the location marked by the dashed line in (A). (C) MAP image of an Air Force resolution test target group 6. (D) MAP image of a 6-μm-diameter carbon fiber. (E) Cross-sectional profile of the 6-μm-diameter carbon fiber.

The major optical absorbers in the visible spectral range in biological tissue include deoxyhemoglobin and oxyhemoglobin. Consequently, PAM, acting as a sensitive blood detector with high contrast and specificity, is suitable for imaging the volumetric morphology of subcutaneous microvasculature *in vivo*.

We applied the OR-PAM to image the microvasculature in an ear of a nude mouse (Hsd:Athymic Nude-Foxn1^{NU}, Harlan Co.; body weight: 20 g) *in vivo* at the optical wavelength of 578 nm. All experimental animal procedures were carried out in conformity with the laboratory animal protocol approved by the School of Medicine Animal Studies Committee of Washington University in St. Louis. Nude mouse ears (thickness: ~300 μm) have well-developed vasculature and have been widely used to study tumor angiogenesis and other microvascular diseases.[17, 18] During image acquisition, the animal, warmed by an infrared lamp, was kept motionless using a breathing anesthesia system (E-Z Anesthesia, Euthanex). Unlike the published study,[19] no optical clearing agent was applied to the skin surface. An area of 1×1 mm^2 was scanned with a step size of 1.25 μm without signal averaging. The scanning time for a complete volumetric dataset was ~10 min. After data acquisition, the animal recovered naturally without observable laser damage.

The OR-PAM image of the microvasculature (Figs. 4A and 4B) agrees with the photograph (Fig. 4C) taken with a transmission optical microscope at a 4× magnification; however, small vessels are only observed in the OR-PAM images. The mean ratio of the photoacoustic amplitudes between the blood vessels and the background is 20:1, which demonstrates a high endogenous optical-absorption-based contrast. Some vessels, such as the vessel labeled with CL in Fig. 4A, have diameters of ~5 μm and hence most probably

are single capillaries. A volumetric rendering of the photoacoustic data (Fig. 4B) shows the 3D spatial positions and connectivity of the blood vessels. For example, at the center of the circle in Fig. 4B, the small-diameter vessel invisible in the MAP image in Fig. 4A is clearly seen ~100 μm above the lager vessel. In addition, vessel branching is clearly observed. Therefore, OR-PAM is able to image single capillaries *in vivo* with endogenous contrast due to the optical absorption of hemoglobin.

1.4 Conclusion

The capability of OR-PAM to image physiological and pathological changes in capillaries and other microvessels has potentially broad applications. Possible applications include microscopic imaging of vasodilation and vasoconstriction in stroke, tumor angiogenesis, tumor extravasations, and tumor metabolic rate of oxygen consumption. Mouse ears were chosen as the initial organ to test OR-PAM because in this case transmission optical microscopy can be used to validate some of our results. Since OR-PAM operates in reflection mode, it can be applied to many other anatomical sites.

Several technical improvements can be made in the future. First, images can be acquired by scanning the optical-acoustic dual foci instead of the animal and the water tank to reduce possible motion artifacts. Second, it is possible to scan only the optical focus within the acoustic focusing area to reduce the image acquisition time by at least an order of magnitude. Third, besides endogenous contrast from hemoglobin, targeted exogenous contrast agents, such as ICG and nanoparticles, can be employed for *in vivo* molecular imaging.[20] Fourth, the acoustic coupling cube in the current design can be

improved to transmit photoacoustic waves much more efficiently (without transformation from *p*-waves into *sv*-waves) so that the SNR can be improved by at least 14 dB. In addition, applying acoustic antireflection coating on the lens should further increase the SNR by another 10 dB.

When the optical focus is 100 μm below the tissue surface, the surface optical fluence is close to the ANSI safety limit (20 mJ/cm^2 in the visible spectral region).[21] Although the ANSI standards regulate only the surface fluence, we compute here the spatial peak optical fluence at the focus in water, which is 500 mJ/cm^2. Even this focal fluence is still less than the damage threshold experimentally observed in small animals.[19] We believe that the optical fluence can be reduced without affecting the SNR after the aforementioned improvements are implemented.

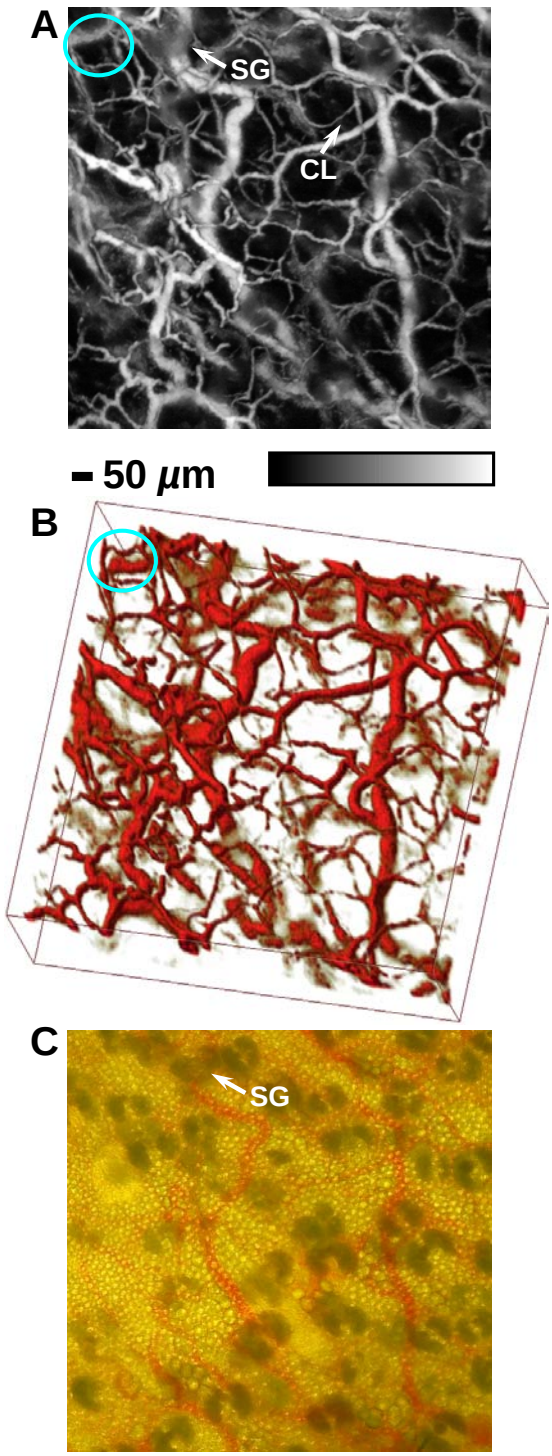

Fig. 4. Microvasculature in a nude mouse ear. (A) *In vivo* OR-PAM image. (B) 3D pseudocolor visualization of the vasculature. (C) Photograph taken with transmission optical microscopy. CL: capillary; SG: sebaceous gland.

2. G2 OR-PAM*

2.1 Introduction

OR-PAM, which can detect both physiologically specific endogenous contrasts (e.g., HbO_2 and HbR[7]) and molecular-specific exogenous contrasts (e.g., congo red labeled amyloid plaques[10]) with cellular or subcellular spatial resolution, has found broad biomedical applications in such fields as neurology,[10] ophthalmology,[8, 11] and vascular biology. In our G1 OR-PAM, the optical-acoustic combiner suffers significant acoustic loss.[10] Moreover, the G1 system could cover only a small FOV within a reasonable acquisition time because translating the living object for scanning must be slow enough to avoid possible disturbance to the object. Here, we report our G2 OR-PAM with improved detection sensitivity and imaging speed. In G2 OR-PAM, we have designed a novel optical-acoustic combiner, which improves the detection sensitivity by 18.4 dB over the G1 system. Moreover, the fiber-based light delivery allows scanning the imaging head rather than the living object, thereby enabling fast *in vivo* imaging (5 times as fast as the G1 system) over a large FOV (centimeters along the lateral dimensions). More valuably, instrument-scanning extends the scope of G2 OR-PAM to objects that are impractical to move mechanically for scanning (e.g., humans).

2.2 Materials and Experiments

Our G2 OR-PAM system (Fig. 5) employs a wavelength-tunable laser system, consisting of a diode-pumped solid-state laser (INNOSLAB, Edgewave) and a dye laser (CBR-D, Sirah), for photoacoustic irradiation at single or multiple optical wavelengths. A mirror-

* S. Hu†, K. Maslov†, and L. V. Wang, "Second-generation optical-resolution photoacoustic microscopy with improved sensitivity and speed," (Ready to submit). † Authors contributed equally to this work.

loaded piezo actuator (P-287, Physik Instrumente) is incorporated into the cavity of the dye laser for fast wavelength tuning (0.3 nm/ms). The output laser beam (pulse width: 7 ns) is reshaped by an iris (ID25SS, Thorlabs; the aperture size is set to 2 mm), and then focused by a condenser lens (LA1131, Thorlabs) before passing through a 50-μm pinhole (P50C, Thorlabs). The pinhole is positioned slightly away from the focus of the condenser lens (focal diameter: 18 μm) to match the diameters of the pinhole and the fundamental-mode beam for effective spatial filtering. The filtered beam is attenuated by a neutral density filter (NDC-50C-2M, Thorlabs) and launched into a single-mode fiber coupler (F-91-C1, Newport). The output of the single-mode fiber (P1-460A-FC-2, Thorlabs) is collimated by a microscope objective (RMS4X, Thorlabs), reflected by a stationary mirror, and fills the back aperture of another identical objective (imaging objective) to achieve nearly diffraction-limited optical focusing. A beam sampler (BSF05-A, Thorlabs) and a photodiode are inserted between the collimation objective and the stationary mirror to monitor the fluctuation in laser intensity. Different from the G1 OR-PAM system (solid-boundary inset in Fig. 5), where two right-angle prisms sandwich a thin layer of silicone oil for acoustic-optical coaxial alignment,[4] G2 OR-PAM replaces the lower right-angle prism with a rhomboid prism (NT49-419, Edmund Optics) to enhance the detection sensitivity (as discussed later). An acoustic lens (NA: 0.5) is ground in the bottom of the rhomboid prism, and provides an acoustic focal diameter of 43 μm at the 50-MHz central frequency of the ultrasonic transducer (V214-BB-RM, Olympus-NDT). The optical and acoustic foci are aligned confocally to maximize the detection sensitivity. The acoustic lens is submerged in a water-filled Petri dish (9 cm in diameter) for acoustic coupling. An imaging window is opened in the bottom of the Petri

dish and sealed with a polyethylene membrane for optical and acoustic transmission. Two-dimensional raster scanning of the imaging head (dashed box in Fig. 5), in combination with time-resolved acoustic detection, provides volumetric imaging of tissue optical absorption. A charge-coupled device camera (MEDSI3, Meade Instruments) is added to view the imaging region through the reverse path of the optical illumination.

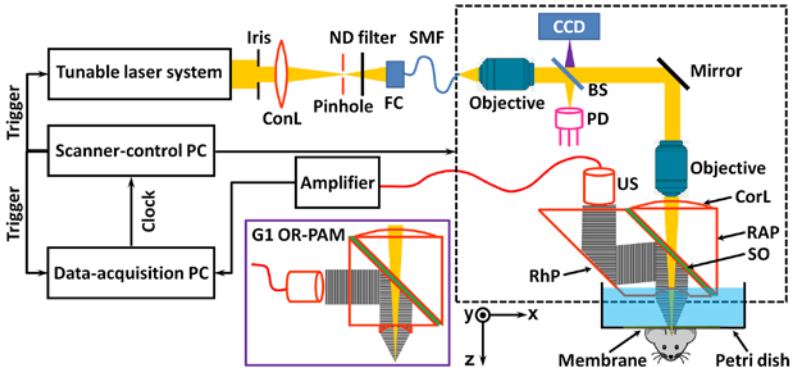

Fig. 5. Schematic of G2 OR-PAM. The solid-boundary inset shows the configuration of the optical-acoustic combiner in the G1 OR-PAM system. ConL: condenser lens; ND: neutral density; FC: fiber collimator; SMF: single-mode fiber; CCD: charge-coupled device; BS: beam splitter; PD: photodiode; CorL: correction lens; RAP: right-angle prism; SO: silicone oil; RhP: rhomboid prism; US: ultrasonic transducer.

2.3 Results and Discussion

In the G1 system, the obliquely incident (45°) acoustic signal is reflected by a single solid-liquid interface (Fig. 5), where the energy of the longitudinal acoustic wave is coupled into both shear and longitudinal waves.[22] According to the boundary conditions and Snell's Law,[23] 85.1% of the incident acoustic energy is transformed from longitudinal mode to shear mode at the interface, and only 0.8% of the acoustic energy remains in longitudinal mode. The second inclined surface provided by the rhomboid

prism in the G2 system is able to transform 97.2% of the shear-wave energy back into longitudinal waves, to which the ultrasonic transducer is much more sensitive. In comparison to the combiner in the G1 system, the new design can theoretically result in a 20-dB increase in the detected longitudinal-wave energy, which was expected to provide much higher detection sensitivity. As an experimental validation, we imaged the same 6 μm carbon fiber using both the G1 and G2 systems (Fig. 6). Our results show that, at the same optical irradiation level (6.5 nJ/pulse), the SNR of the G2 system was 18.4 dB higher than that of the G1 system. The actual improvement in SNR is in good agreement with the theoretical estimation.

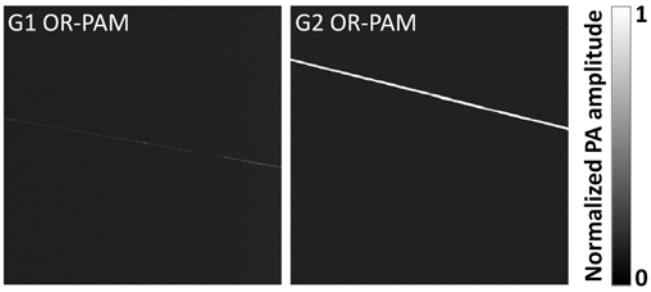

Fig. 6. Sensitivity comparison of the G1 and G2 OR-PAM systems by imaging the same carbon fiber at the same laser fluence level. PA: photoacoustic.

In the G2 OR-PAM system, the NAs of both microscope objectives are 0.1 in air. However, the imaging objective is compensated for water immersion by the correction lens, so the effective NA of the imaging objective is 0.133. Thus, the theoretical lateral resolution (measured in FWHM) of the G2 system (i.e., the diffraction-limited optical focal diameter) is calculated to be 2.14 μm at 570 nm. The lateral resolution of the G2 system was experimentally quantified by imaging an Air Force resolution test target (04TRN003, CVI Melles Griot) at 570 nm. As shown in Figs. 7A and 7B, the G2 system

is capable of resolving the finest line pairs (Group 7, Element 6) with a modulation depth of 62%. Modulation transfer function analysis[4] reveals a cutoff spatial frequency (i.e., the frequency at which the modulation depth reaches zero) of 390 cycles/mm, which corresponds to a FWHM resolution of 2.56 μm. The experimentally measured lateral resolution is slightly worse than the diffraction-limit estimate, which is likely due to imperfect aberration compensation. The maximum tissue penetration was also experimentally quantified by inserting a 250-μm-diameter black needle obliquely into a living mouse leg (Hsd:Athymic Nude-Foxn1^{NU}, Harlan). As shown in Fig. 7C, the G2 system can clearly image the needle down to 1.2 mm beneath the tissue surface. Compared with the 0.7-mm *ex vivo* penetration of G1 OR-PAM at 630 nm (where blood absorption is ~25 times lower than at 570 nm), the 1.2-mm *in vivo* penetration of G2 OR-PAM at 570 nm is much deeper, due to the enhanced detection sensitivity.

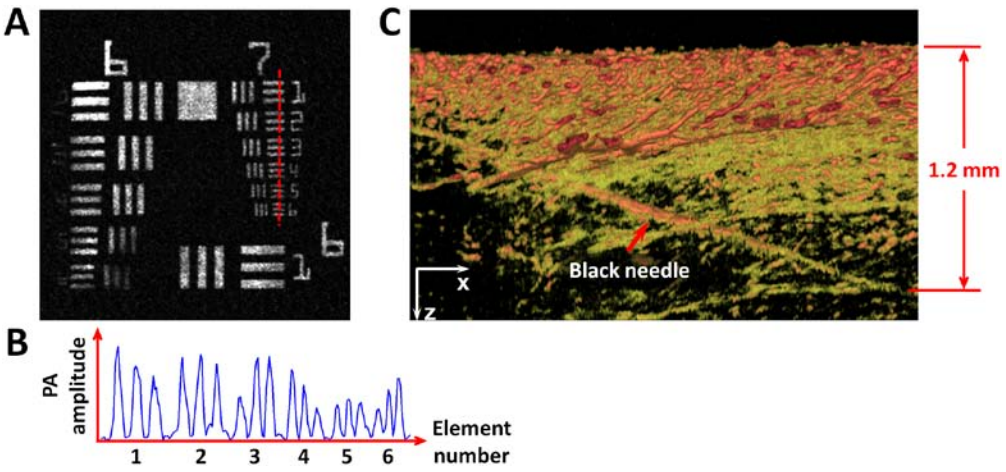

Fig. 7. Spatial resolution and *in vivo* tissue penetration of the G2 OR-PAM. (A) OR-PAM image of an Air Force resolution test target. (B) The cross-sectional profile of the 6 elements in group 7 of the resolution target, as indicated by the red dashed line in (A). (C) OR-PAM image of a black needle inserted obliquely in a living mouse leg. PA: photoacoustic.

The much improved system performance enables G2 OR-PAM to image a large FOV with single RBC resolution and sensitivity. Figure 8 shows the whole-ear vascular anatomy in a 10-week-old living nude mouse (Hsd:Athymic Nude-Foxn1^{NU}, Harlan) imaged by OR-PAM at 570 nm. The laser pulse energy after the imaging objective was measured to be 80 nJ. Since the optical focus is 150-μm beneath the skin surface, the surface laser fluence is 22 mJ/cm^2, which is close to the ANSI safety limit (20 mJ/cm^2 in the visible spectral region). Densely packed capillary beds as well as discrete RBCs traveling along capillaries are clearly resolved. The typical acquisition time of such a single-wavelength, bidirectionally scanned image (image size: 7.8 mm × 10 mm; step size: 2.5 μm × 2.5 μm) is 70 min, which is 5 times as fast as that for the G1 system. The B-scan rate of 7.8 mm across is 0.95 Hz. Because the absorption coefficient of blood at 570 nm is estimated to be 240.6 cm^{-1} and the SNR within the dual foci is 42.7 dB, the sensitivity of G2 OR-PAM in terms of the noise-equivalent absorption coefficient is 1.8 cm^{-1}. With dual-wavelength measurements (561 nm and 570 nm), G2 OR-PAM can also reveal the sO_2 of the whole-ear vasculature at the capillary level (Fig. 9). The image acquisition time of such a detailed sO_2 map is 80 min (image size: 10.6 mm ×10 mm; step size: 2.5 μm × 5 μm). Note that the scanning speed of the G2 OR-PAM system can be further improved by using a high-repetition-rate laser. Our recent experimental results show another 3-fold improvement in speed with a 40-kHz pulsed laser.

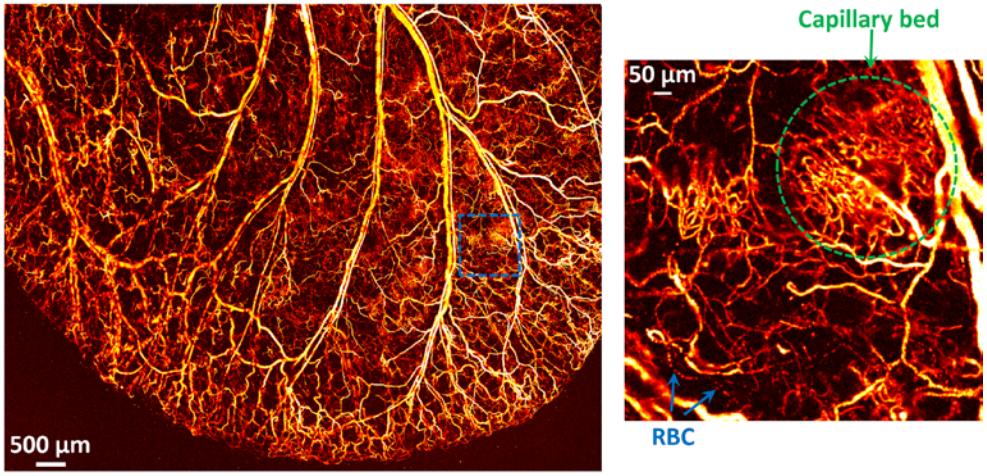

Fig. 8. OR-PAM of vascular anatomy in a living mouse ear. Insert shows a densely packed capillary bed and individual red blood cells traveling along a capillary.

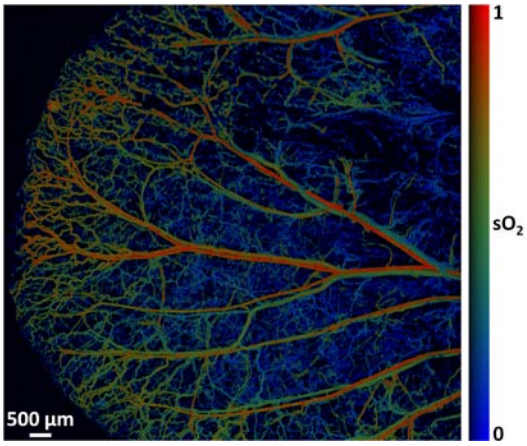

Fig. 9. Dual-wavelength (561 nm and 570 nm) OR-PAM of sO_2 in a living mouse ear.

Taking advantage of the time-resolved acoustic detection, G2 OR-PAM can clearly differentiate skull vessels and cortical vessels in living mice. As a validation, we perfused the skull vessels in a 3-month-old Swiss Webster mouse (Hsd:ND4, Harlan) with methylene blue dye. At 570 nm, both the methylene-blue-perfused skull vessels and the RBC-perfused cortical vessels provide strong photoacoustic signals, which are shown

in different colors in the depth-encoded image (Fig. 10A). At 650 nm, where hemoglobin has very low optical absorption (~40 times lower than at 570 nm), only the skull vessels remain visible (Fig. 10B), which show perfect agreement with the green-encoded skull vasculature in Fig. 10A. Note that the depth range (0–375 μm) in Fig. 10A does not reflect the maximum cortical penetration of G2 OR-PAM through the intact skull, because the maximum signal rather than the deepest signal is projected along each A-line.

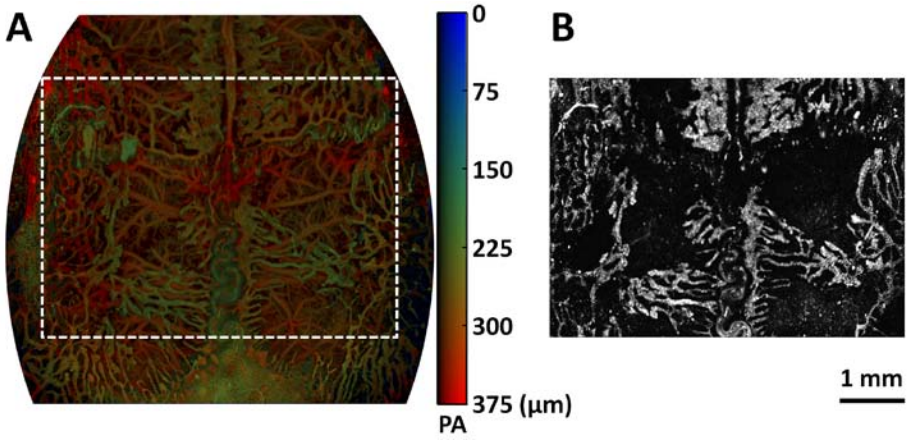

Fig. 10. Transcranial OR-PAM of a living adult mouse brain. (A) depth-encoded MAP image of both methylene-blue-perfused skull vasculature and blood-perfused cortical vasculature at 570 nm. (B) MAP image of methylene-blue-perfused skull vasculature at 650 nm. PA: photoacoustic.

2.4 Conclusion

We have developed G2 OR-PAM with high-sensitivity acoustic detection and instrument-scanning. Compared with G1 OR-PAM, the detection sensitivity and the scanning speed are improved by 18.4 dB and 5-fold, respectively. Large-FOV, volumetric microscopy of vascular anatomy and sO_2 are demonstrated. The imaging speed can be further improved without compromising the FOV by combining optical and mechanical scanning.

3. G3 OR-PAM*

Recently, we developed a prototype of G3 OR-PAM with combined optical-scanning and mechanical-scanning (Fig. 11). To implement the optical scanning, we replaced the stationary mirror in the mechanical-scanning-based G2 system with a 2-D fast steering mirror.

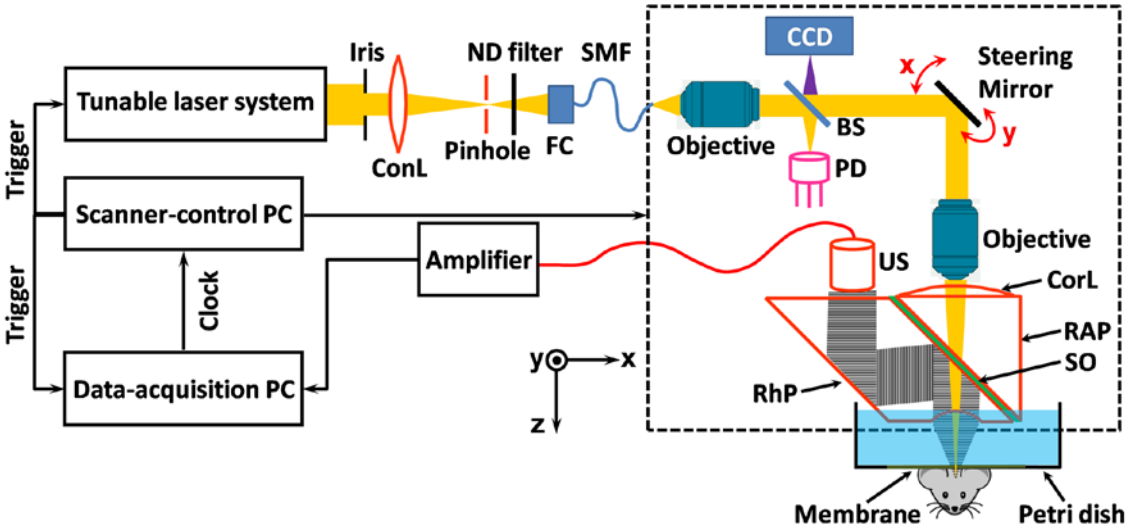

Fig. 11. Schematic of G3 OR-PAM. ConL: condenser lens; ND: neutral density; FC: fiber collimator; SMF: single-mode fiber; CCD: charge-coupled device; BS: beam splitter; PD: photodiode; CorL: correction lens; RAP: right-angle prism; SO: silicone oil; RhP: rhomboid prism; US: ultrasonic transducer.

As a proof-of-principle demonstration, we first mechanically scanned the entire ear of a nude mouse (Hsd:Athymic Nude-Foxn1NU, Harlan Co.) to create a site map (Fig. 12A), and then a ROI containing a single capillary was identified and optically scanned for 100 volumetric frames to visualize the flow of individual RBCs along the targeted capillary with relatively low laser fluence (Fig. 12B) and high fluence (Fig. 12C),

* S. Hu, et. al., Preliminary data.

successively. It is interesting that, at low laser fluence, three representative optical-scanning frames show different RBC distributions, which indicates an undergoing capillary flow. However, with increased laser fluence, different frames show identical RBC distributions, suggesting a laser-induced capillary clot. Note that other acute hemodynamics (e.g., vasomotion and vasodilation) at the capillary level are also expected to be visible to G3 OR-PAM.

This demonstration projects the great potential of G3 OR-PAM in better understanding microvascular functioning and extracting regional oxygen metabolism, which may revolutionize the study of vascular biology and neurovascular coupling. However, the current design and operation of G3 OR-PAM requires further optimization. The optical-acoustic combiner used here is not ideal for optical scanning, because the relatively long optical path within the bulky combiner may induce noticeable optical aberrations. Moreover, the tightly focused acoustic lens (focal diameter: 43 μm) seriously limits the FOV of optical scanning. A future refinement is to eliminate the optical-acoustic combiner by using a high-frequency wide-band ring transducer (center frequency: 43 MHz; 6 dB round-trip bandwidth: 36 MHz; f-number: 1.5; diameter of the inner hole: 1.92mm). The center hole in the transducer is ideal for aberration-free confocal alignment of optical irradiation and acoustic detection. Moreover, the increased acoustic focal diameter (75 μm) enlarges the FOV of optical scanning. Another future direction is to hybrid optical scanning with mechanical scanning for high-speed, wide FOV imaging.

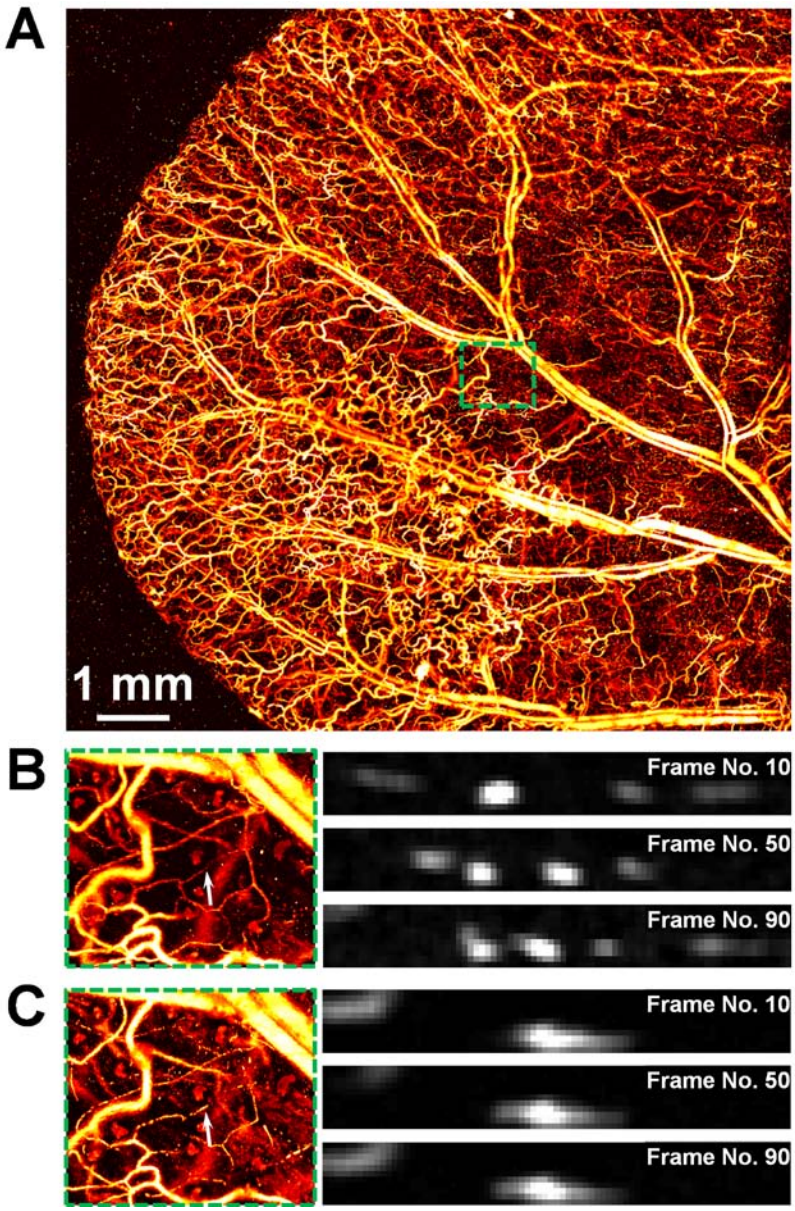

Fig. 12. Real-time OR-PAM of capillary flow in a living mouse ear. (A) Large FOV mechanical scanning of the entire ear. Green dashed box: ROI containing the capillary to be optically scanned. (B) and (C) were acquired with low and high laser fluence, respectively. In both (B) and (C), the left column is the mechanical scanning of the ROI, wherein the white arrows indicate the same capillary to be optically scanned. The right column contains three representative maximum-amplitude-projected optical-scanning frames of the capillary.

4. Example biomedical applications at a variety of *in vivo* anatomical sites

4.1 Noninvasive label-free imaging of acute microhemodynamics in mouse ears*

4.1.1. Introduction

The microcirculation plays a central role in the regulation of the metabolic, hemodynamic and thermal state of the individual.[24] Many major diseases[25-31] are manifest in the microcirculation before they are clinically evident, which provides a potential early perspective on the origin and progression of such diseases. However, established clinical imaging modalities such as CT, MRI, PET, and ultrasonography lack the resolution needed for microvascular imaging.[32] Even with iodine contrast, x-ray imaging cannot image single capillaries. Thus, optical microscopy has been widely used to assess the cellular and molecular features of the microcirculation. IVM, for example, is the gold standard for microcirculation studies. It allows quantification of vessel count, diameter, length, density, permeability, and blood flow velocity. Nevertheless, to observe capillaries *in vivo*, IVM generally requires trans-illumination and surgical preparation,[33] restricting its application to limited anatomical sites and interfering with the intrinsic microcirculatory function. Additionally, conventional IVM lacks depth resolution that is crucial for extracting the 3-D microvascular morphology. Confocal microscopy[34] and two-photon microscopy,[35] noninvasive and possessing excellent depth-sectioning capability, have difficulty in detecting microvessels without exogenous fluorescent agents, which, although having greatly facilitated laboratory research, are still facing challenges in clinical translations.[36] OPS imaging permits noninvasive microvascular imaging without the use of fluorescent dyes,[37] paving its way to the bedside. However, OPS

* Reprinted with permission from S. Hu, K. Maslov and L. V. Wang, "Noninvasive label-free imaging of microhemodynamics by optical-resolution photoacoustic microscopy," Opt. Express 17(9), 7688-7693 (2009).

provides no depth information and lacks the measurement consistency[38] required for longitudinal studies.

To overcome these difficulties, we have developed OR-PAM, a noninvasive volumetric microscopy technology capable of detecting the physiologically specific absorption signatures of endogenous chromophores, such as hemoglobin, *in vivo*. The ability to introduce hemoglobin absorption contrast into the optical-resolution microscopy regime leads to an extremely versatile technique for microcirculation studies, without the limitations of fluorescent labeling and invasiveness. Besides the morphological parameters, such as vessel count, diameter, and length, OR-PAM also validates the quantification of important functional parameters, including HbT and sO_2[39, 40] down to the capillary level. Multiple attractive features make OR-PAM a valuable tool for microcirculation studies (Table 1), which is demonstrated below by noninvasively monitoring microhemodynamic activities *in vivo*.

Table 1. Comparison of modern high-resolution microvascular imaging techniques. CM: confocal microscopy; TPM: two-photon microscopy.

Modality	3D morphology	sO_2 quantification	HbT quantification	Imaging contrast	Working manner
IVM		✓†		Scattering, fluorescence	Invasive
CM	✓			Scattering, fluorescence	Noninvasive
TPM	✓			Fluorescence	Noninvasive
OPS			✓	Absorption‡	Noninvasive
OR-PAM	✓	✓	✓	Absorption	Noninvasive

† IVM requires adopting Raman spectroscopy for sO_2 measurement.

‡ Different from OR-PAM, OPS provides negative absorption contrast.

4.1.2. Methods

Our OR-PAM system employs nearly diffraction-limited optical focusing with bright field illumination to achieve 5-μm lateral resolution. The axial resolution is calculated to be ~15 μm, based on the transducer bandwidth and the speed of sound in tissue. The B-scan rate over a 1-mm distance is ~1 frame per second. The detailed system design is described in.[41] Through time-resolved ultrasonic detection and 2-D raster scanning along the transverse plane, the OR-PAM system records the complete 3-D microvasculature of the tissue, which can be viewed in MAP image (Fig. 13a) or direct volumetric rendering (Fig. 13b). All experimental animal procedures were carried out in conformance with the laboratory animal protocol approved by the School of Medicine Animal Studies Committee of Washington University in St. Louis.

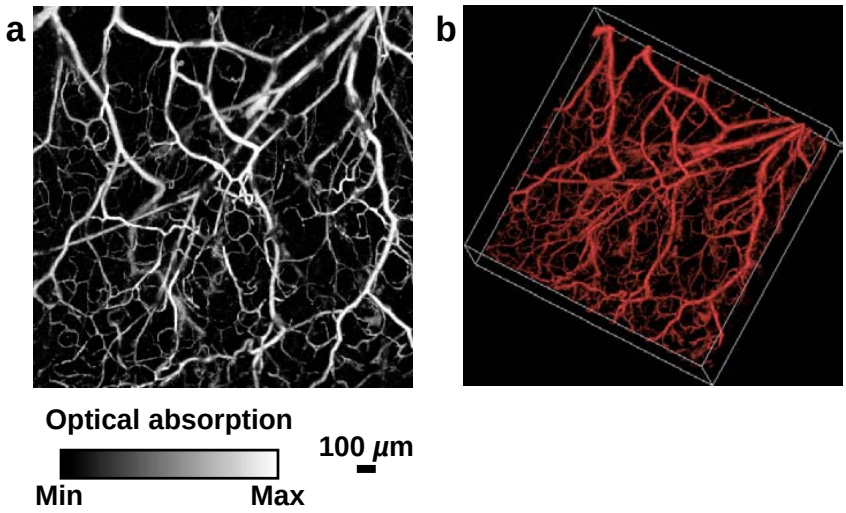

Fig. 13. A representative microvascular network in a nude mouse ear imaged *in vivo* by OR-PAM. (a) MAP image. (b) 3D morphology.

4.1.3. Results and Discussion

Vasodilation, an important vessel activity in regulating tissue oxygen delivery, refers to an increase in vessel diameter. In contrast, vasomotion is a periodic oscillation of the vessel diameter and is not a consequence of the heart beat, respiration, or neuronal input.[42] Substantive experimental work has suggested that vasomotion might serve as a protective mechanism under conditions of ischemia and be an important indicator of cardiovascular events,[43] but its physiological role and the underlying mechanism remain elusive.[44]

To explore vasomotion and vasodilation in response to tissue oxygen variation, first we selected a 1-mm-by-1-mm region in a nude mouse ear. Structural and sO_2 images (Fig. 14) were acquired by a dual-wavelength measurement under systemic normoxia. According to the sO_2 value, we selected an arteriole-venule pair (A1 and V1 in Fig. 14b), which were almost perpendicular to the B-scan direction (marked by the yellow dashed line in Fig. 14b). In this case, the B-scan image delineates the actual vessel cross section.

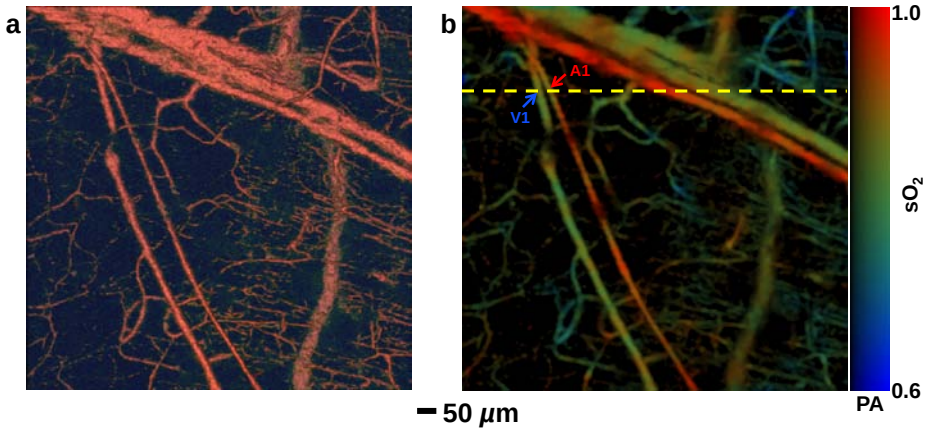

Fig. 14. Structural and functional microvascular imaging by OR-PAM in a nude mouse ear *in vivo*. (a) Structural image acquired at 570 nm. (b) Vessel-by-vessel sO_2 mapping based on dual-wavelength (570 nm and 578 nm) measurements. The calculated sO_2

values are shown in the color bar. PA: photoacoustic signal amplitude. A1: a representative arteriole; V1: a representative venule. Yellow dashed line: the B-scan position for Fig. 15.

Then, we repeated the selected B-scan continuously for seventy minutes, during which the physiological state of the animal was switched between systemic hyperoxia and hypoxia (indicated by the red and blue time segments, respectively, in Fig. 15a–c) by alternating the inspired gas between pure oxygen and hypoxic gas (5% O_2, 5% CO_2 and 90% N_2). Vasomotion and vasodilation were clearly exhibited by the diameter oscillation and expansion of the vessel cross section, respectively, in response to the changes in the physiological state (Fig. 15a, b). To provide quantitative analysis, we estimated the vessel diameter by calculating the FWHM value of the blood vessel signal in each B-scan. The time course of the arteriolar diameter change (Fig. 15c) and the corresponding Fourier transform analysis (Fig. 15d) show that arteriole A1 had a significant vasomotion under hyperoxia, with an oscillation frequency of ~1.6 cpm, which is in good agreement with the observation from a previous invasive study.[45] Compared with arteriole A1, venule V1 had a much weaker vasomotion with a similar oscillation frequency (Fig. 15c, e). To isolate the vasodilation effect, we smoothed out the diameter oscillation due to vasomotion by 60-point moving averaging (Fig. 15c). The smoothed curve clearly suggests a significant increase of 96±3% in the arteriolar diameter under hypoxia, whereas the change in the venous diameter is as small as 26±5%. Our results, again, are in good agreement with recent work done by scanning laser ophthalmoscopy with the aid of fluorescent particles.[46] The temporal resolution provided by OR-PAM also enabled us

to estimate the 10-90% full-scale response time of vasodilation to systemic hypoxia to be ~3 minutes.

4.1.4. Perspectives

In future studies, quantification of the local metabolic rate of oxygen consumption would be an exciting extension.[47] To this end, we need to measure the vessel diameter, blood oxygenation, and blood flow. The first two parameters are currently measurable with OR-PAM, and the PAD technique has been suggested for blood flow measurement in the microcirculation.[48] One of our future directions is to integrate PAD flow measurement into the OR-PAM system to assess the local metabolic rate at a microscopic level.

Another interesting direction is to combine OR-PAM with other high-resolution imaging tools, such as confocal microscopy and two-photon microscopy, for multi-modality imaging. The fruitful cellular and molecular information provided by them, based on scattering or fluorescence contrast, will be highly complementary.

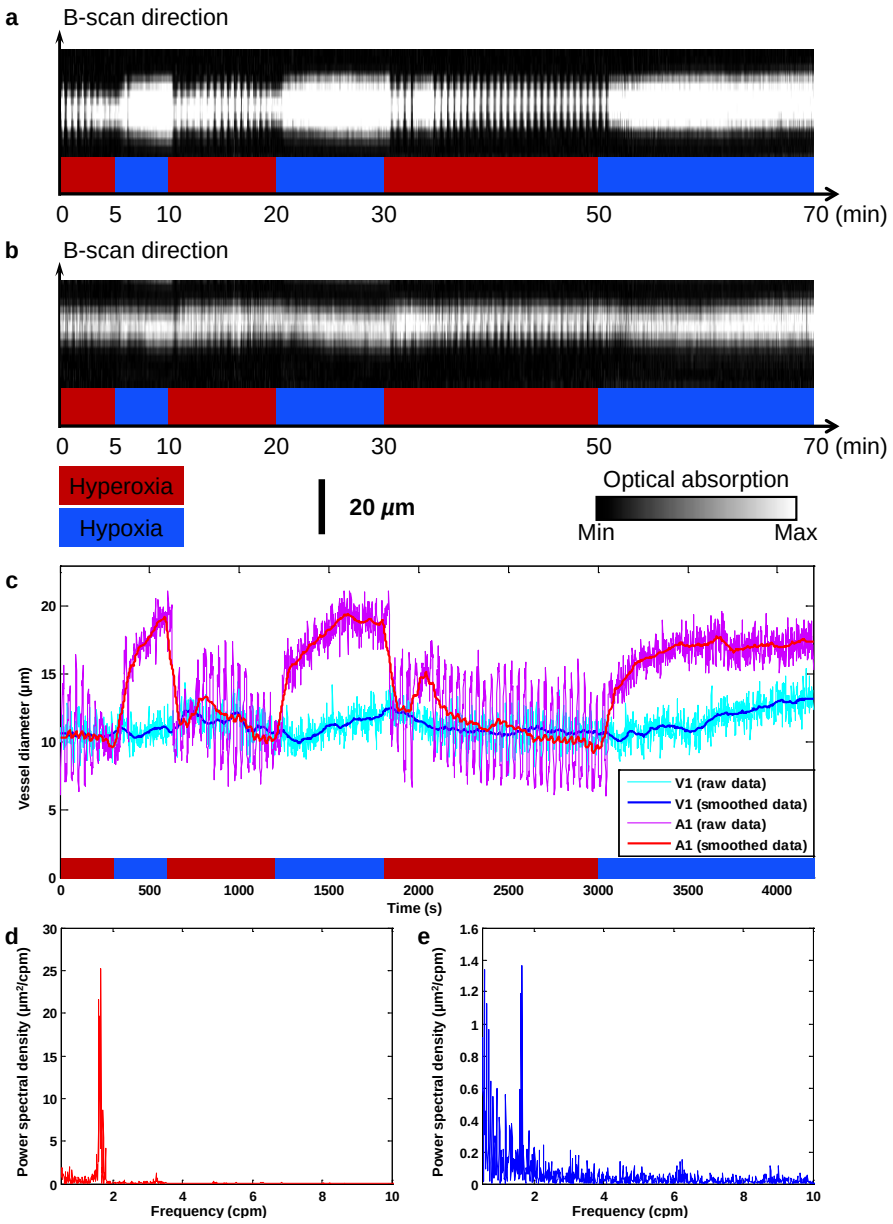

Fig. 15. Vasomotion and vasodilation in response to switching the physiological state between systemic hyperoxia and hypoxia. (a) B-scan monitoring of the changes in the cross section of arteriole A1. (b) B-scan monitoring of the changes in the cross section of venule V1. (c) Changes in arteriolar and venous diameters in response to changes in physiological state (raw data were smoothed via 60-point moving averaging to isolate the effect of vasodilation). (d) Power spectrum of the arteriolar vasomotion tone. (e) Power spectrum of the venous vasomotion tone.

4.2 Longitudinal monitoring of microvascular wound healing in mouse ears*

4.2.1. Introduction

Chronic imaging of the microcirculation *in vivo* permits direct visualization of long-term microhemodynamics, which is closely associated with disease progression,[49,50] neural dynamics,[51] and functional recovery from pathological states.[52] However, existing high-resolution microvascular imaging techniques suffer in different regards when employed for chronic studies. For example, invasive procedures[33] and fluorescence labeling[34,35] generally disturb the normal physiology of the microcirculation, discourage longitudinal studies, and impede clinical translations.

To overcome these difficulties, we have developed a bright-field PAM with optically diffraction-limited lateral resolution, called OR-PAM, for *in vivo* microvascular imaging down to the capillary level.[41] OR-PAM is highly sensitive to the physiologically specific optical absorption of hemoglobin, thereby bypassing the limitations of invasiveness and phototoxicity. By keeping the microcirculation intact, OR-PAM is ideal for chronic studies. In this letter, we report on the first demonstration of using OR-PAM for functional chronic imaging. The healing process of a laser-induced microvascular lesion was monitored over a period of twelve days. Chronic OR-PAM imaging permits direct visualization of the morphological and functional recovery of the microcirculation after laser destruction.

* Reprinted with permission from S. Hu, K. Maslov and L. V. Wang, "*In vivo* functional chronic imaging of a small animal model using optical-resolution photoacoustic microscopy," Med. Phys. 36(6), 2320-2323 (2009).

4.2.2. Methods

In our OR-PAM system (Fig. 16), the animal tissue is irradiated with a short-pulsed laser beam generated by a wavelength-tunable laser set, consisting of an Nd:YLF pump laser (INNOSLAB, Edgewave) and a dye laser (CBR-D, Sirah). Wideband ultrasonic waves—referred to as photoacoustic waves—are induced as a result of transient thermoelastic expansion due to the laser excitation, collected via an acoustic lens, and then detected by a high-frequency ultrasonic transducer (V2022 (BC), Olympus NDT). To maximize the sensitivity for *in vivo* capillary imaging, the optical illumination and the ultrasonic detection in our system are configured confocally by an acoustic-optical beam splitter. In this simple design, two right-angle prisms form a cube with a thin silicone oil layer in between. The glass and the silicone oil have similar optical refractive indices (1.1 in ratio) but very dissimilar acoustic impedances (12.7 in ratio), which makes the layer optically transmissive but acoustically reflective. The lateral resolution of this acoustic-optical confocal configuration is determined by the product of the two point-spread functions of the optical illumination and the acoustic detection. Since acoustic resolution is difficult to achieve down to the capillary level due to the frequency-dependent ultrasonic absorption, a microscopic objective lens (RMS4X, Thorlabs) is employed to achieve diffraction-limited optical resolution. For chronic study, a transmission-mode optical microscope is integrated into our system by adding a light-emitting diode beneath the animal holder. Utilizing the reverse optical path of the OR-PAM illumination, the imaging region can be viewed under an eyepiece. This addition helps us quickly target the same ROI during multi-day monitoring. The detailed system description and performance can be found in our previously published paper.[41]

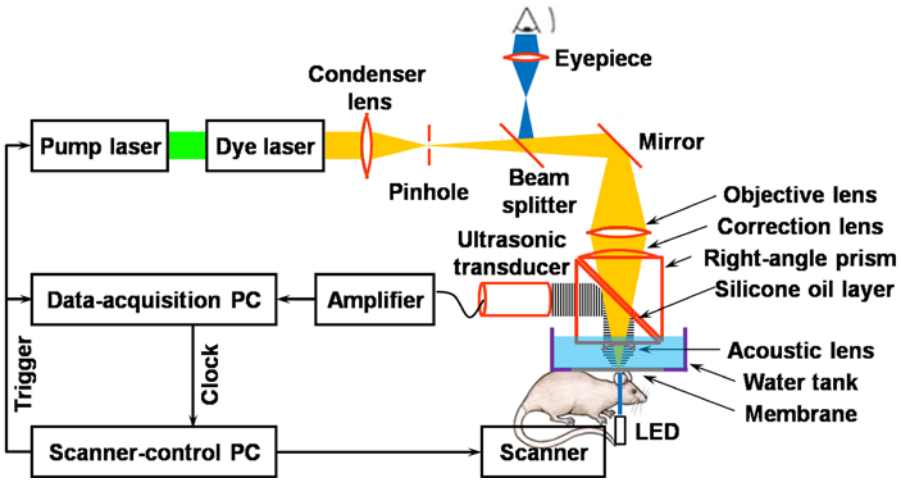

Fig. 16. Schematic of the OR-PAM system.

The advantages of OR-PAM include the following: (i) Endogenous optical absorption contrast enables direct imaging of microvessels down to capillaries, with a high signal-to-noise ratio (SNR);[41] (ii) Multi-wavelength measurement permits vessel-by-vessel mapping of blood oxygenation,[39, 40, 53] holding the potential for functional studies such as brain function mapping;[54] (iii) Time-resolved ultrasonic detection provides depth information without depth scanning; (iv) Working in reflection mode noninvasively makes the technique applicable to more anatomical sites *in vivo*, without disturbing the microcirculatory function.

4.2.3. Results and Discussion

The above advantages, along with measurement consistency, permit OR-PAM to monitor long-term microhemodynamics. One promising application lies in the realm of laser microsurgery, where OR-PAM can provide fruitful structural and functional information about the targeted microvascular lesions, such as their morphology, precise location, and blood oxygenation, which will facilitate accurate diagnosis and proper treatment. More

importantly, OR-PAM enables noninvasive monitoring of the healing process of the microvascular lesions after laser microsurgery, which has been desired for a long time.[55]

A mouse ear model was chosen to demonstrate this ability *in vivo*, because it is among the few anatomical sites that are readily imaged by transmission-mode optical microscopy, which can be used to partially validate OR-PAM. All experimental animal procedures were carried out in conformance with the laboratory animal protocol approved by the School of Medicine Animal Studies Committee of Washington University in St. Louis.

One day before the beginning of the chronic study, the hair on the left ear of a nude mouse (Hsd:Athymic Nude-Foxn 1^{NU}, Harlan Co., ~25 g) was gently removed with human hair-removing lotion (Surgi Cream, Ardell Int'l). For daily monitoring, a dose of 87 mg/kg ketamine and 13 mg/kg xylazine was administered intraperitoneally to anesthetize the animal right before transferring it to a stereotaxic imaging stage. During the experiment, a dual-wavelength (570 nm and 578 nm) OR-PAM measurement was utilized to extract HbT and sO_2. 570 nm is an isosbestic point, and the photoacoustic signal acquired at this wavelength reflects HbT. 578 nm is a local absorption peak of oxyhemoglobin, which helps differentiate it from deoxyhemoglobin. A detailed description of the method used for computing sO_2 can be found in the previously published paper.[53] Throughout each experiment, anesthesia was maintained using vaporized isoflurane (1.0–1.5% isoflurane with an airflow rate of 1 liter/min), and the body temperature of the animal was maintained at 37ºC with a temperature controlled heating pad. At the end of the chronic study, the animal was euthanized by an intraperitoneal administration of pentobarbital at a dosage of 100 mg/kg.

At the beginning of the chronic imaging, we selected and photographed a 1-mm-by-1-mm region in the mouse ear under a commercial transmission-mode optical microscope. Then we imaged the ROI using OR-PAM (Fig. 17a), after which we switched the excitation source to a CW laser (output power: 150 mW; wavelength: 532 nm) and removed the pinhole to enable the laser to create a microvascular lesion for study. The central part of the ROI (0.25 mm by 0.25 mm) was then scanned with the focused CW laser beam (diameter: ~30 μm) for ~10 min. The ROI was imaged immediately after the CW laser treatment (Fig. 17b) and in the subsequent twelve days (Fig. 17, c-1 to c-12), using both our OR-PAM system and the commercial transmission-mode optical microscope. Our results clearly show a four-step wound healing process:[56] (i) Vessel regression and hemostasis occurred right after the laser destruction (Fig. 17b); (ii) Inflammation, the second phase of wound healing, was exhibited in the form of vasodilation 24 hours after the injury and lasted for about five days (Fig. 17, c-1 to c-5). Hypoxia facilitated the synthesis of the vascular endothelial growth factor to trigger angiogenesis (Fig. 17, b and c-1 to c-5); (iii) About three days after the wound occurred, the ingrowth of new capillaries started to restore the microcirculation (Fig. 17c-3), which was previously supplied by the damaged arteriole; (iv) After 12 days, the damaged arteriole-venule pair were almost completely recovered to normal status (Fig. 17c-12). The microvascular morphology imaged by OR-PAM is partially validated by the commercial transmission-mode optical microscope; however, capillary networks are only visible to OR-PAM. The consistency in microvascular morphology during the multi-day monitoring implies the robustness of our technique.

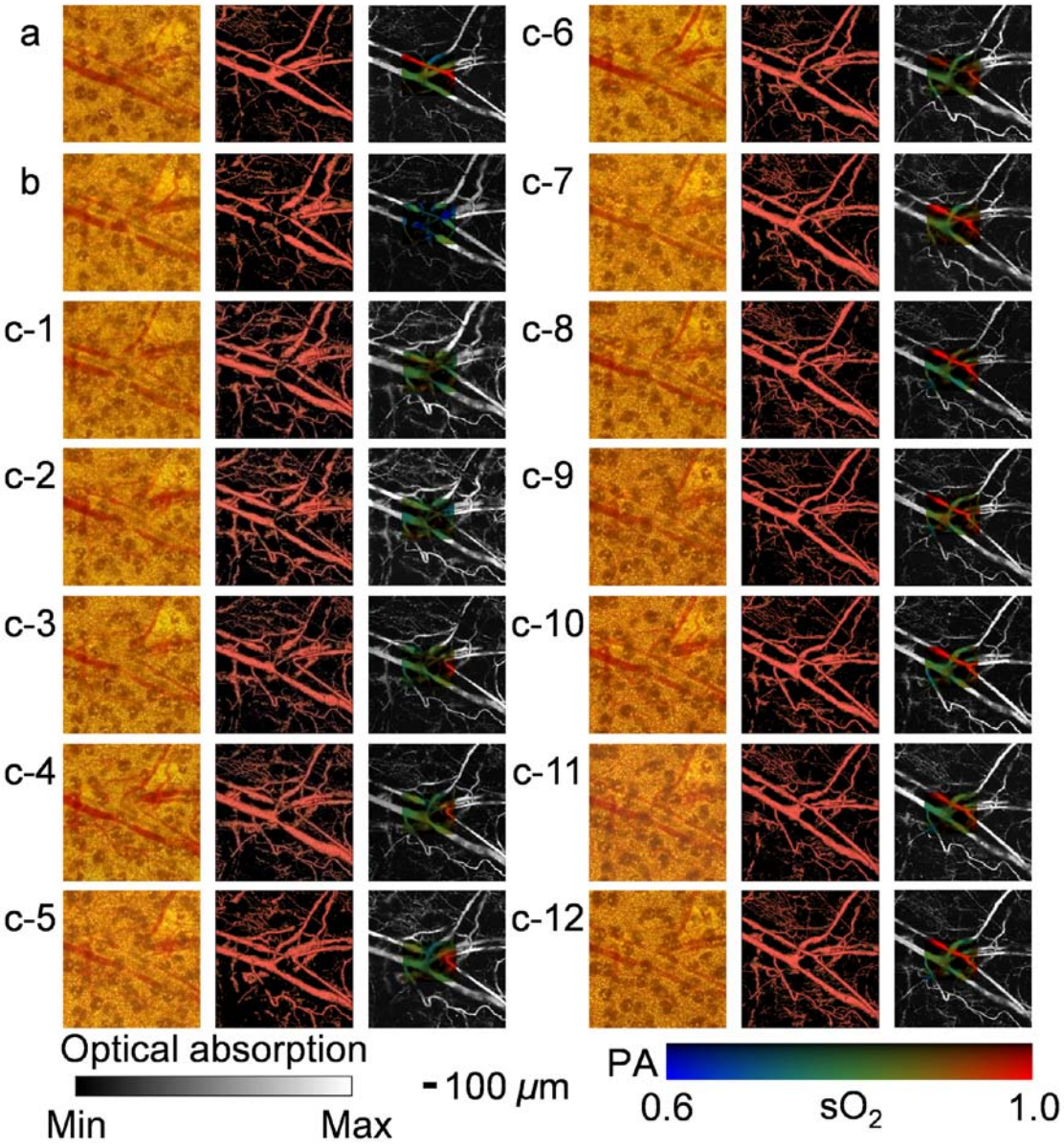

Fig. 17. OR-PAM monitoring of the healing process of a laser-induced microvascular lesion. (a) Before laser destruction. (b) Immediately after laser destruction. (c) On each of the subsequent 12 days. The left image in each part (a through c-12) is a photograph taken by a commercial transmission-mode optical microscope; the middle one is the front-view of the 3-D microvascular morphology acquired by OR-PAM at 570 nm; the right one is the MAP image overlaid by the sO_2 mapping of the laser-damaged region.

4.2.4. Conclusion

In this work, we demonstrated the capability of OR-PAM for functional chronic imaging of microhemodynamics *in vivo* noninvasively. However, this technique has potentially broader applications. In cancer research, OR-PAM can monitor tumor angiogenesis and evaluate tumor therapy.[49] In drug development for microvascular dysfunctions, such as stroke, OR-PAM can trace drug functioning and evaluate drug efficacy. In the physiological study of angiogenesis, OR-PAM can help to understand the signal transduction pathway by perturbing it and detecting the difference before and after perturbation. In laser microsurgery, surgical lasers can be readily integrated into our OR-PAM system to perform on-site high-precision microsurgery with pre-surgery diagnosis and post-surgery evaluation. In neuroscience, the noninvasive feature and fine imaging resolution make OR-PAM ideal for chronic studies of cortical plasticity[57] as well as neurovascular coupling[58] at the capillary level.

4.3 Functional transcranial imaging of adult mouse brains*

4.3.1. Introduction

Advances in brain imaging facilitate the understanding of cognitive phenomena and neurological diseases. One of the most popular techniques is to use a single electrode or a microelectrode array to record neural activities directly from cortical neurons. However, this procedure is quite invasive, thereby limiting the number of recordings and discouraging chronic imaging. Alternatively, downstream hemodynamics originating from the brain microcirculation has been recorded to retrace the brain function.[54] VSDI[59] provides direct, fast, and linear measurement of the changes in action potential of neurons; nevertheless, the use of dye labeling may cause phototoxicity. ISI avoids phototoxicity by detecting the optical scattering and absorption of biological tissues or the fluorescence of intrinsic chromophores;[60] however, it offers a spatial resolution of only ~50 μm, which is not adequate for capillary imaging. TPM, possessing micrometer spatial resolution, has been very successful in functional brain imaging,[35] but it requires the skull to be thinned or even removed, which impedes longitudinal studies of cortical plasticity and disease progression. Optical micro-angiography,[61] essentially D-OCT, has successfully demonstrated microvascular perfusion imaging through intact mouse skulls by taking advantage of the intrinsic blood flow information; however, its resolution and sensitivity are not yet sufficient to resolve single capillaries. High-resolution brain imaging through intact animal skulls remains challenging for pure optical modalities because the optical scattering and absorption of the skull degrade the imaging resolution and SNR. Photoacoustic imaging, combining light and ultrasound in a single hybrid

* Reprinted with permission from S. Hu, K. Maslov, V. Tsytsarev, and L. V. Wang, "Functional transcranial brain imaging by optical-resolution photoacoustic microscopy," J. Biomed. Opt. 14, 040503 (2009).

technology,[47] suggests a potential solution. Using AR-PAM, Stein et al. recently demonstrated mouse brain imaging through both intact scalp and skull.[62] This noninvasive feature is highly desirable for functional or chronic studies; however, with its current spatial resolution (lateral resolution: 70 μm; axial resolution: 54 μm), capillaries are not resolvable. To fill the gap, Maslov et al. developed OR-PAM capable of imaging single capillaries *in vivo*.[41] The lateral resolution of OR-PAM matches the size of a single RBC, and its sensitivity enables single RBC detection.[63]

Here, we report on the first demonstration of OR-PAM for functional brain microvascular imaging down to single capillaries through intact mouse skulls. The minimally invasive feature is favorable for chronic study of cortical plasticity. Moreover, since neuronal activity is widely assumed to spatially correlate most closely to the capillary bed response,[64] improving localization of signals down to the capillary level will enable functional brain mapping at micrometer resolution.

4.3.2. Methods

Before functional brain imaging, a Swiss Webster mouse (Hsd:ND4, Harlan Co., 25–30 g) was anesthetized by intraperitoneally administering a dose of 87 mg/kg ketamine and 13 mg/kg xylazine and transferred to a stereotaxic imaging stage. The scalp of the mouse was surgically removed, and the exposed skull was cleaned with 0.9% sodium chloride irrigation solution right before imaging. Ultrasonic gel was used for ultrasound coupling and maintaining skull hydration. Throughout the experiment, the animal was supplied with breathing-grade air and maintained under anesthesia using vaporized isoflurane (1.0–1.5% isoflurane with an airflow rate of 1 liter/min). The body temperature of the

animal was maintained at 37ºC by a temperature controlled heating pad. At the end of the experiment protocol, the animal was euthanatized by an intraperitoneal administration of pentobarbital at a dosage of 100 mg/kg.

In photoacoustic measurements of hemoglobin concentration and oxygenation, we assume that, in the visible spectral range, HbO_2 and HbR are the dominant absorbing compounds in blood.[65] Thus, a dual-wavelength measurement is adequate to image sO_2, though using more wavelengths is expected to yield more accurate results.[53] The two wavelengths chosen here are 570 nm and 578 nm, where the absorption contrast between blood and background brain tissues are high enough to enable satisfactory imaging quality.[65] According to the published absorption spectra of rat hemoglobin,[66] 570 nm is an isosbestic point, at which HbO_2 and HbR have the same molar extinction coefficients. Thus, the photoacoustic signal acquired at this wavelength reflects HbT. 578 nm is an HbO_2-absorption-dominant wavelength, which helps differentiate the two types of hemoglobin. Since blood oxygenation is highly correlated with local metabolism, the sO_2 value is generally time-variant. To minimize measurement error due to the possible temporal fluctuation in blood oxygenation, we implemented a wavelength auto-tuning program to control the dye laser, and imaged the same B-scan for each of the wavelengths before moving to the next B-scan. The ROI was scanned with a step size of 2.5 μm. The dual-wavelength measurement took approximately 20 minutes, which was mostly limited by the wavelength tuning speed of the dye laser.

4.3.3. Results and Discussion

Figures 18a and 18b are MAP images of the mouse brain microvasculature under systemic normoxia at the optical wavelengths of 570 nm and 578 nm, respectively. Since 570 nm is an isosbestic point, Fig. 18a maps the HbT, regardless of the blood oxygenation. Microvessels labeled with CL in Fig. 18a appear to be single capillaries with diameters of 5–10 μm. At the conclusion of the dual-wavelength measurement, the concentrations of HbR and HbO_2, as well as the sO_2 values, were calculated based on the model described in previously published work.[53, 65] As shown in Fig. 18c, different sO_2 levels are visualized with pseudocolors ranging from blue to red, while the HbT measured at the isosbestic point (570 nm) is represented by pixel brightness. According to known physiology, the red vessels (sO_2 values greater than 90%) are believed to be arterioles, whereas the green ones (sO_2 values as low as 60–70%) are most likely to be venules. However, in the microcirculation, there is no clear cutoff in sO_2 value between arterioles and venules.[67] The blood oxygenation is closely associated with the microvascular branching order[67] and the local metabolic activity of the tissue.[68] To demonstrate the oxygen gradients in the brain microcirculation, we selectively analyzed a post-capillary venular tree (Fig. 18d) and a pre-capillary arteriolar tree (Fig. 18e) highlighted in Fig. 18c by the blue and red dashed boxes, respectively. The vessel diameters and the corresponding sO_2 values in different branching orders are listed in Table 2. A negative correlation between the branching order and its mean sO_2 value is observed in both the arteriolar and venular trees with a linear regression analysis (arteriolar tree: $R^2 = 0.98$, $p = 0.01$; venular tree: $R^2 = 0.75$, $p = 0.14$), as shown in Fig. 19. Our results suggest that: (i) the blood oxygenation level is higher in the arteriolar tree

than in the venular tree; (ii) capillaries are not the only oxygen exchange site in the microcirculation, because the sO_2 decreases significantly with vascular branching in the pre-capillary arteriolar tree (~12% from order 1 to 4); and (iii) a diffusional shunt is present between arterioles and venules to elevate the oxygen level in "large" venules, because the sO_2 increases noticeably with blood confluence in the post-capillary venular tree (~9% from order 1 to 4). Our observation is in agreement with the published work.[67-69]

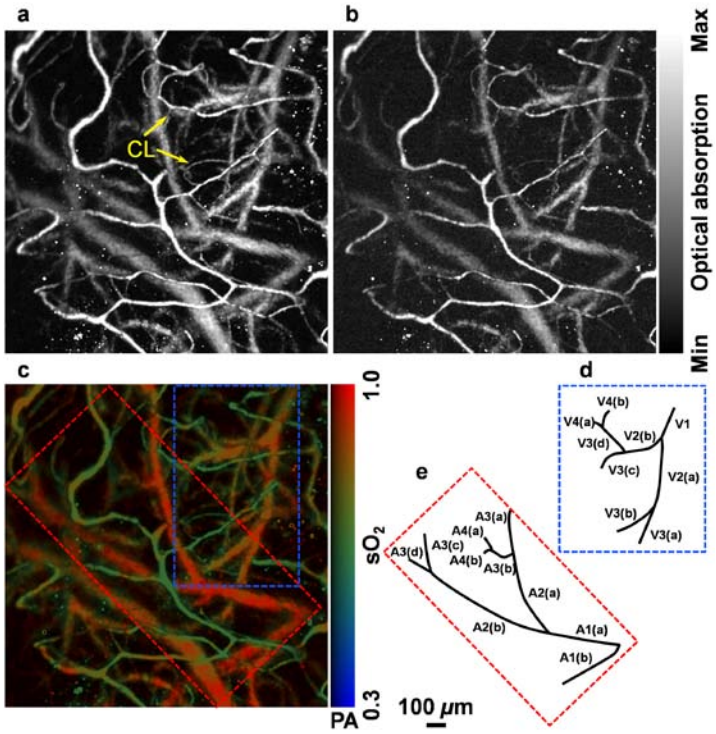

Fig. 18. *In vivo* functional OR-PAM imaging of mouse brain microvasculature through an intact skull. (a) MAP image acquired at 570 nm; (b) MAP image acquired at 578 nm; (c) vessel-by-vessel sO_2 mapping; (d) a venular tree with branching orders [boxed by blue dashed lines in (c)]; (e) an arteriolar tree with branching orders [boxed by red dashed lines in (c)]. The calculated sO_2 values are shown in the color bar. PA: photoacoustic signal amplitude. The scale bar applies to (a–c).

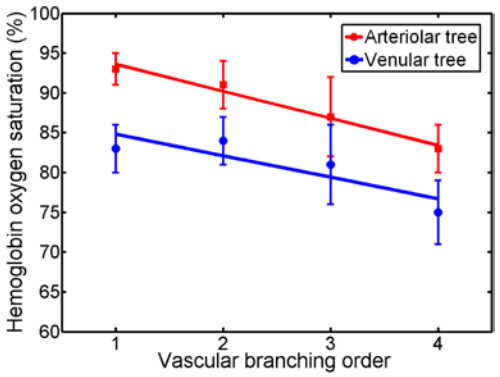

Fig. 19. The sO_2 value versus the vascular branching order in a pre-capillary arteriolar tree and a post-capillary venular tree. The square and round markers represent the mean sO_2 values in each branching order, and the error bars stand for the standard deviations of the mean sO_2 values.

Table 2(a). The vessel diameters and the sO_2 values in different branching orders in a venular tree. Values are in mean ± standard deviation format.

Branching	1	2		3				4	
Vessel ID	V1	V2(a)	V2(b)	V3(a)	V3(b)	V3(c)	V3(d)	V4(a)	V4(b)
Vessel	57±2	48±5	42±3	35±2	30±2	41±2	24±3	20±2	19±3
sO_2 (%)	83±3	83±3	85±2	86±3	83±3	78±2	75±4	74±5	76±4

Table 2(b). The vessel diameters and the sO_2 values in different branching orders in an arteriolar tree. Values are in mean ± standard deviation format.

Branching	1		2		3				4	
Vessel ID	A1(a)	A1(b)	A2(a)	A2(b)	A3(a)	A3(b)	A3(c)	A3(d)	A4(a)	A4(b)
Vessel	59±4	48±3	43±4	52±2	44±4	32±2	51±2	42±4	23±3	24±2
sO_2 (%)	93±2	93±2	91±3	91±3	89±2	88±4	87±3	79±3	85±2	81±3

According to a previous study,[70] the wavelength-dependent optical attenuation due to the intact skull affects the measurement accuracy. Here, this wavelength dependence was estimated by measuring the photoacoustic signals of a black polyethylene film attached beneath the skull of a freshly sacrificed mouse of the same type at the two operating wavelengths, respectively. The mouse skull was submerged in 0.9% sodium chloride irrigation solution to keep hydration. Since the black polyethylene film can be considered as a neutral absorber in the visible spectral range, the wavelength dependence in the photoacoustic signals is expected to be predominantly from the mouse skull. If we consider the skull to be homogeneous within the ROI,[65] such dependence can be simply compensated for by applying different calibration factors to the measured photoacoustic signals at different optical wavelengths. However, the wavelength-dependent optical scattering and absorption of brain tissues are difficult to compensate for due to heterogeneous tissue structure and composition.[71]

4.3.4. Conclusion

In summary, OR-PAM has been applied to mouse brain imaging through intact skulls with capillary-level spatial resolution. Functional information of HbT and sO_2 within single microvessels was imaged simultaneously using a dual-wavelength measurement. The ability to extract brain oxygen saturation information on a single capillary basis with minimal invasiveness makes OR-PAM a potential tool for high-resolution functional brain mapping, quantitative analysis of brain energy metabolism, and chronic studies of cortical plasticity and neurological diseases. It is worth noting that the maximum imaging depth of OR-PAM, estimated from the surface of the intact skull, is 500–600 μm when

the system is operated at the Q-band of the hemoglobin absorption spectrum (optical wavelength: ~560 nm). This penetration is slightly less than the typical imaging depth of TPM (600–800 μm) through a skull window with NIR excitation,[72] where no bone is in the optical path. NIR light sustains less brain tissue absorption and scattering than visible light. However, owing to the quadratic intensity-dependence in two-photon generation and linear dependence in OR-PAM, the light scattering and absorption within the intact skull as well as the surface scattering at the skull-brain interface decreases the fluorescence signal in TPM much faster than the photoacoustic signal in OR-PAM. As a result, TPM has not demonstrated transcranial imaging. By utilizing NIR operation and compromising the lateral resolution, D-OCT can extend the imaging depth to ~1.5 mm.[61] To enhance the penetration of OR-PAM, system SNR or imaging contrast needs to be further improved.

4.4 Label-free photoacoustic angiography of mouse eyes*

4.4.1. Introduction

Visual impairment is highly prevalent worldwide. Ten percent of the U.S. adult population has experienced vision problems,[73] many of which are manifest in the ocular circulation.[74] Fluorescence angiography is very successful in the diagnosis of ocular vascular diseases and has been well accepted as the gold standard for ocular circulation imaging. However, an inherent limitation of fluorescence angiography is the required injection of contrast agents (fluorescein or indocyanine green) that can cause pain and complications such as emesis, anaphylactic reactions, or even death.[75] Moreover, the angiographic agents may fail to perfuse if there is conspicuous vascular leakage. Thus, the development of label-free imaging techniques to avoid these problems is warranted.

Our previous work on photoacoustic tomography, an emerging hybrid technique capable of detecting optical absorption ultrasonically, has demonstrated its unique advantage of utilizing endogenous hemoglobin contrast for subcutaneous and cortical vascular imaging in living animals as well as in humans.[39, 58] With recent advances in optical illumination and ultrasonic detection mechanisms,[41] we have successfully extended the application of this technique to ophthalmology. Here, we report OR-PAM for *in vivo* label-free functional imaging of the ocular microcirculation.

4.4.2. Methods

To achieve spectroscopic measurements, our OR-PAM system (Fig. 20) employs a wavelength-tunable laser system consisting of a Nd:YLF pump laser (INNOSLAB,

* Reprinted with permission from S. Hu, B. Rao, K. Maslov, and L. V. Wang, "Label-free photoacoustic ophthalmic angiography," Opt. Lett. 35 (1), 1–3 (2010).

Edgewave) and a dye laser (CBR-D, Sirah). The laser beam is attenuated by a neutral density filter (NDC-100C-2, Thorlabs) before being spatially filtered through a 25-μm pinhole (P25C, Thorlabs), and then is focused by a microscope objective (RMS4X, Thorlabs) to achieve micrometer lateral resolution. An optical beam splitter, in combination with a photodiode (SM05PD1A, Thorlabs), is inserted between the pinhole and the microscope objective to monitor laser intensity fluctuation. A homemade acoustic-optical beam splitter, consisting of two right-angle prisms (NT32-545, Edmund Optics) and a 100-μm thick layer of silicone oil (1000cSt, Clearco Products), is placed under the objective lens to separate optical illumination and acoustic detection.[41] A 75-MHz ultrasonic transducer (V2022 BC, Olympus NDT) is attached to the vertical side of the bottom prism. An acoustic lens (NA: 0.46; radius of curvature: 5.2 mm) is attached to the bottom of the splitter and immersed in the water tank to collect photoacoustic signals. An imaging window in the bottom of the water tank is sealed with an ultrasonically and optically transparent polyethylene membrane. Typically, before imaging, an adult Swiss Webster mouse (Hsd:ND4, Harlan Co., 25–30 g) was anesthetized and transferred to a homemade stereotaxic imaging stage. Lubricating drops (Butler AHS) were gently administered to both eyes, and then ultrasonic gel was evenly applied between the imaging window and the eye for ultrasound coupling and eye hydration. The water tank had a low-pressure contact with the cornea to avoid possible disturbance to the intrinsic ocular circulation. Anesthesia was maintained throughout the experiments by an isoflurane machine (1.0–1.5% vaporized isoflurane with an airflow rate of 1 L/min). The body temperature of the animal was maintained at 37 ºC with a temperature controlled

heating pad. At the end of the experiments, the animals were euthanized by an intraperitoneal administration of pentobarbital at a dosage of 100 mg/kg.

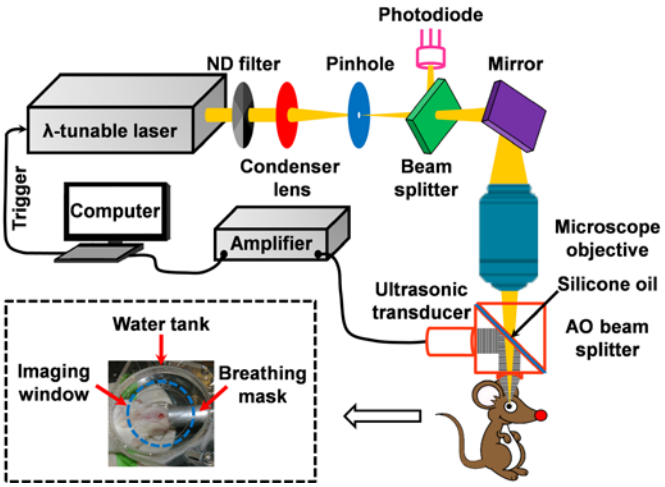

Fig. 20. Schematic of the photoacoustic ophthalmic angiography system. The inset photograph shows the animal positioning. λ: wavelength; AO: acoustic-optical; ND: neutral density.

4.4.3. Results and Discussion

Compared with conventional fluorescence angiography, OR-PAM has multiple advantages. First, hemoglobin absorption provides endogenous and functional imaging contrast. In OR-PAM, a nanosecond-pulsed laser beam is absorbed by hemoglobin molecules circulating in the ocular microvasculature. The resulting transient thermoelastic expansion induces wideband ultrasonic waves, which are detected by a high-frequency ultrasonic transducer to form a projection or volumetric angiogram (Fig. 21a). Since hemoglobin is the predominant light absorber in the intrinsic microcirculation, blood vessels detected by OR-PAM must contain RBC, the carrier of hemoglobin. This characteristic guarantees that OR-PAM images only RBC-perfused capillaries, the functional subset of capillaries responsible for supplying oxygen to the eye.

A second advantage is that tight optical focusing and the high nonradiative quantum yield of hemoglobin enable single-RBC resolution and sensitivity. The 5-µm resolution in our current design matches the average size of single RBCs. Moreover, hemoglobin is a non-fluorescent molecule, and thus almost all the absorbed photon energy is converted to heating, which elicits photoacoustic emission. OR-PAM's micrometer spatial resolution enables visualizing individual RBCs traveling along iris capillaries (Fig. 21b). The Gaussian fit of the cross-sectional photoacoustic signal profile (Fig. 21c) of a chosen particle observed by OR-PAM (crossed by the red dashed line in Fig. 21b) has a FWHM of ~6 µm. The size and high contrast-to-noise ratio (~20 dB) suggest that these particles (the yellow arrows in Fig. 21b) are single RBC disks imaged sideways. The high detection sensitivity also permits the use of a laser exposure level well within the ANSI safety standards (expanded upon later).

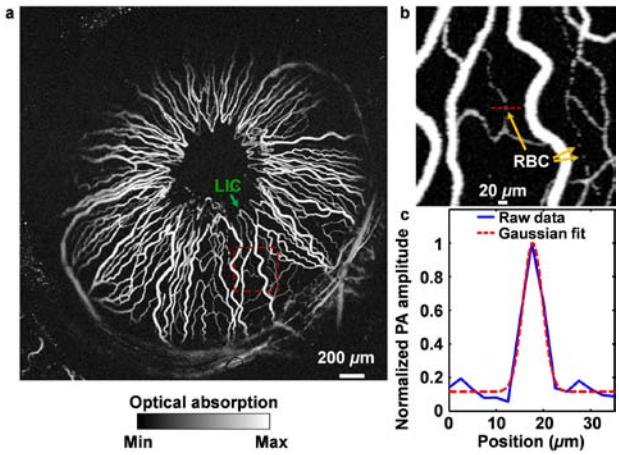

Fig. 21. Label-free photoacoustic ophthalmic angiography of the iris microvasculature of a living adult Swiss Webster mouse. (a) The MAP image acquired at 570 nm. (b) A close-up of the boxed area in panel a. The yellow arrows indicate individual RBCs in iris capillaries. (c) The profile of an RBC crossed by the red dashed line in panel b. LIC: lesser iris circle. PA: photoacoustic signal.

Third, endogenous contrast combined with low-level exposure enables repetitive imaging or chronic monitoring, which is highly desirable for treatment evaluation and drug development. As a simple demonstration, we re-imaged the same ROI shown in Fig. 21a. With the focal plane lowered towards the posterior segment, the peripheral vascular structures—the CP, RCB, and MIC that bifurcates into multiple RIA—are better visualized in Fig. 22, though the LIC are slightly blurred. Compared with Fig. 21a, Fig. 22 shows essentially no change in the general microvascular morphology.

As a fourth advantage, spectroscopic measurements offer functional characterization of blood oxygenation. Capitalizing on the distinct difference in the absorption spectra of HbO_2 and HbR, we used two excitation wavelengths (570 and 578 nm) to estimate the concentrations of HbO_2 and HbR, thereby mapping the sO_2 on a single-vessel basis (the dashed-line box in Fig. 22). Blood oxygenation levels are pseudocolored from blue to red in an ascending order. From the sO_2 mapping, we can clearly identify the RIAs, and we can also observe the transition in blood oxygenation from arteries to veins.

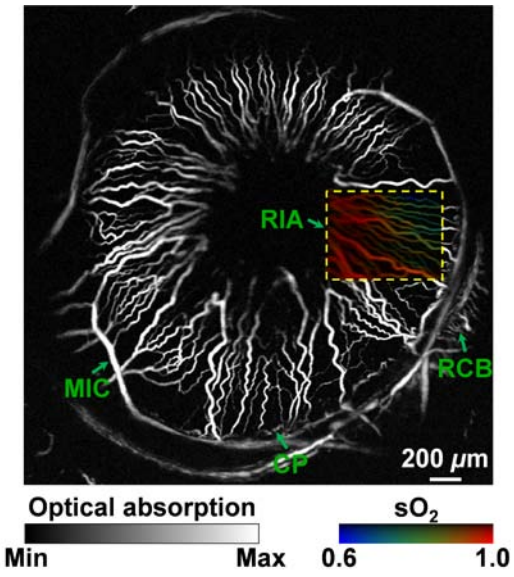

Fig. 22. Label-free photoacoustic ophthalmic angiography of sO_2 in the iris microvasculature of a living adult Swiss Webster mouse. The imaged region is the same as that shown in Fig. 21a, but with a focal plane closer to the posterior segment to better visualize the peripheral vascular structures. A dual-wavelength (570 and 578 nm) sO_2 measurement was performed on the boxed region of interest. A vessel-by-vessel sO_2 mapping was generated and overlaid on the maximum amplitude projection image acquired at 570 nm. CP: ciliary process; MIC: major iris circle; RCB: recurrent choroidal branch; RIA: radial iris artery.

For potential clinical applications, the MPE that OR-PAM can apply is subject to the ANSI safety standards for the eye.[76] Since the PRF of our OR-PAM laser is less than the critical frequency (55 kHz for wavelengths between 0.4 to 1.05 μm), three ANSI rules need to be tested. The experimental parameters used for the following calculation are listed in Table 3.

Rule 1. Single Pulse Limit. The MPE for a single laser pulse is

$$\mathrm{MPE}_{\mathrm{SP}} = 5.0 C_E \times 10^{-7} = 1.33 \times 10^{-4} \left[\mathrm{J}/cm^2\right], \quad (1)$$

where $C_E = \alpha^2 / (\alpha_{\max} \alpha_{\min}) = 267$ is the extended source correction factor. Here, α_{max} = 100 mrad is the apparent angle subtended by a source above which the thermal hazard is proportional to the radiance of the source, and α_{min} = 1.5 mrad is the apparent angle subtended by a source above which extended source MPEs apply.

Rule 2. Average Power Limit. First, consider one B-scan. During each B-scan, the OR-PAM laser sends a pulse train containing 1600 pulses with a PRF of 600 Hz. Since the B-scan exposure time (~2.7 s) is longer than 0.7 s and the wavelength is between 400

and 600 nm, dual limits due to both photochemical and thermal effects apply here. For photochemical effects, the MPE for the B-scan pulse train is

$$\mathrm{MPE}_{\mathrm{Bscan}}(photochemical) = 100\mathrm{C}_B \times (\pi/4)\alpha^2 \times 10^{-6} = 790\left[\mathrm{J}/cm^2\right], \quad (2)$$

where $C_B = 10^{0.02(\lambda-450)} = 251$ is the wavelength correction factor, and α = 200 mrad is the angular subtense. For thermal effects, the MPE for the B-scan pulse train is

$$\mathrm{MPE}_{\mathrm{Bscan}}(thermal) = 1.8C_E T_{Bscan}^{0.75} \times 10^{-3} = 1.01\left[\mathrm{J}/cm^2\right], \quad (3)$$

where T_{Bscan} = 2.7 s is the exposure duration of each B-scan as listed in Table 3. Thus, the MPE/pulse for the B-scan pulse train is

$$\mathrm{MPE}_{\mathrm{Bscan}}(thermal)/n_{Bscan} = 6.3\times10^{-4}\left[\mathrm{J}/cm^2\right], \quad (4)$$

where n_{Bscan} = 1600 is the number of pulses in each B-scan. Second, consider the total 2-hour laser exposure. For photochemical effects, the MPE for the total exposure duration is the same as that for each B-scan, as calculated in Eq. (2). For thermal effects, the MPE for the total exposure duration is

$$\mathrm{MPE}_{\mathrm{Total}}(thermal) = 1.8C_E T_2^{-0.25} \times 10^{-3} \cdot T_{\max} = 1093\left[\mathrm{J}/cm^2\right], \quad (5)$$

where T_2 = 100 s is the exposure duration beyond which the thermal MPE for an extended source is constant in terms of irradiance, and T_{max} = 7200 s is the duration of a complete exposure. Thus, the MPE/pulse for the total 2-hour laser exposure is

$$\mathrm{MPE}_{\mathrm{Total}}(photochemical)/n_{Total} = 3.1\times10^{-4}\left[\mathrm{J}/cm^2\right], \quad (6)$$

where $n_{Total} = 2.56\times10^6$ is the number of pulses in the total 2-hour exposure.

Rule 3. Repetitive Pulse Limit. The MPE is

$$\mathrm{MPE}_{\mathrm{RP}} = n_{Total}^{-0.25}\mathrm{MPE}_{\mathrm{SP}} = 3.3\times10^{-6}\left[\mathrm{J}/cm^2\right]. \quad (7)$$

Rule 3 is the most conservative of the three. Therefore, the overall MPE for each pulse is 3.3×10^{-6} J/cm^2. If the pupil diameter D is 7 mm,[76] the maximum permissible single laser pulse energy in our OR-PAM system is

$$\mathrm{MPE}_{\mathrm{RP}} \times \pi \times (\mathrm{D}/2)^2 = 1.3[\mu\mathrm{J}], \tag{8}$$

which is ~30 times greater than our experimentally used laser pulse energy of ~40 nJ.

Table 3. Experimental parameters.

λ (nm)	*PRF* (Hz)	t (s)	T_{Bscan} (s)	T_{max} (s)	α (mrad)
570 and 578*	600**	7×10^{-9}	2.7**	7200**	200***

λ: wavelength; *PRF*: pulse repetition frequency; t: duration of a single pulse; T_{Bscan}: exposure duration of each B-scan; T_{max}: duration of a complete exposure; α: angular subtense.

*Because 570 and 578 nm are close to each other and show minimal differences in terms of the safety limits, we use 570 nm throughout the calculation.

**In the experiments shown in Figs. 21a and 22, the imaged region of interest is 4 mm by 4 mm, with a scanning step size of 2.5 μm. Unidirectional B-scan is utilized to avoid the effect due to the backlash of the mechanical scanner. Each forward B-scan takes ~2.7 s, and the scanner reposition takes another ~1.8 s. The total image acquisition time is ~2 hr (7200 s), which is limited by the mechanical scanning speed.

***The angular subtense is estimated by the NA of the microscope objective, which is 0.1 in our current system.

4.4.4. Conclusion

Thus, we conclude that OR-PAM eliminates the need for injected contrast agents, offers significant promise for diagnosis and monitoring of ocular diseases, and poses essentially no radiation hazards. For clinical applicability, the next step is to improve the imaging speed of the system, through methods such as optical scanning.[77]

III. OR-PAM IN VASCULAR BIOLOGY

1. HIF-mediated multistage neovascularization with stage-specific sensitivity to VEGFR inhibitors*

1.1 Introduction

Neovascularization is a process whereby new vessels are created and existing ones remodeled to supply growing or ischemic tissues with oxygen and nutrients. While numerous studies have been performed in preclinical tumor or ischemia models, determination of the mechanisms of angiogenesis and neovascularization regulation in the absence of disease could provide insight into endothelial cell signaling and stromal cell trafficking otherwise obscured by a microenvironment altered by illness.

Neovascularization is an adult developmental program that unfolds over time, induced by a collection of angiogenic factors. However, preclinical studies of neovascularization have focused on one or a few time points in what is a continuous process, or have used vectors transiently expressing elevated levels of angiogenic factors.[78] Adult neovascularization and stromal remodeling in the absence of disease were studied using Tet-inducible VEGF.[79] However, because of the inaccessibility of organs targeted for VEGF gain of function, liver and heart, neovascular development was not studied using day-to-day analysis following transgene activation. Moreover, these organs possessed a tissue cellular organization that made spatial analysis between transgene broadcasting and receiving vascular cells challenging. Another strategy for conditional adult neovascular induction was cell autonomous regulation, within the endothelial cell

* Reprinted with permission from Sunday Oladipupo†, Song Hu†, Andrea C. Santeford, Junjie Yao, Joanna Kovalski, Ralph V. Shohet, Konstantin Maslov, Lihong V. Wang, and Jeffrey M. Arbeit, "Conditional HIF-1 induction produces multistage neovascularization with stage-specific sensitivity to VEGFR inhibitors and myeloid cell independence," Blood, (Under revision). † Authors contributed equally to this work.

itself. There, high-level transgenic overexpression of constitutive myristoylated AKT produced marked alterations of microvessel structure and stromal edema; however, the kinetics of neovascular development was not investigated.[80]

Neovascularization is also ideally suited to serial imaging. Elegant studies delineated alterations of both the microvasculature and the microenvironment using optical microscopy techniques, such as single- or multi-photon fluorescence microscopy and D-OCT.[50] However, challenges with such pure optical techniques included the requirement for repeated fluorescent dye injections, the need for tissue window construction, or the necessity for blood flow.[81, 82]

In most instances, neovascularization in disease is coordinated by induction of the HIF family, primarily HIF-1 and HIF-2.[83] These transcription factors are heterodimers of an oxygen-labile HIF-1 or -2alpha (α) subunit, each paired with the same stable HIF-beta (β) subunit. Oxygen instability is mediated by prolyl hydroxylase catalyzed hydroxylation of proline residues within the "oxygen-dependent degradation domain", ODD.[84] Non-hypoxic HIF-α induction is produced by enhanced HIF mRNA translation controlled by PI3 kinase-mTOR pathway activation.[85] HIF-1 and -2 induce expression of multiple angiogenic factors.[86] HIFs signal angiogenesis via paracrine,[18] autocrine,[87] and endocrine mechanisms.[88] HIF-1 and -2α protein overexpression has been documented in human ischemic tissues and organs, high-grade premalignant lesions, and cancers.[83, 85] HIF-1α expression levels are also prognostic in clinical malignancies.[85] Previously, we reported that germline transgenic expression of a HIF-1αΔODD mutant in skin produced hypervascularity with microvessels of normal morphology. However, the vasculature in

that model was quiescent lacking endothelial proliferation, angiogenesis, or microvascular network growth over time.[18]

Here we deployed a conditional expression strategy to create a disease-free model of HIF-1 induction in adult epithelium. We targeted a DOX-regulated, oxygen-insensitive HIF-1α transgene to mouse skin (TetON-HIF-1 mice). HIF-1 activation produced three-stages of neovascularization: development, maintenance, and transgene-dependent regression. Surprisingly endothelial proliferation was cell autonomously downregulated by a DNA damage checkpoint despite persistent VEGFR2 activation. Moreover, myeloid cells recruited to the skin stroma neither contributed to neovascularization nor to VEGF inhibitor resistance. PAM longitudinally imaged and determined microcirculatory dynamics during neovascular network development, transgene-dependent regression, and stage-specific angiogenic inhibitor responsiveness. The preclinical TetON-HIF-1 model and L-PAM technology are promising tools for studying angiogenesis and the microenvironment as they are altered during neovascularization.

1.2 Results

1.2.1. Model development, transgene, and target gene expression kinetics

Basal keratinocytes were chosen as targets for conditional HIF-1 induction in TetON-HIF-1 DTG mice because they are epithelial cells distributed along the epidermal basement membrane, ideally positioned for paracrine signaling to the stroma.[89] Ear skin was chosen for detailed investigation, because of its paucity of fur and its frequent use in several transgenic and adenoviral-mediated angiogenesis studies.[18, 78, 90, 91] However, TetOn-HIF-1 truncal skin displayed similar stromal alterations (data not shown). To

control for purported antiangiogenic and protease inhibitor activities of DOX,[92] NTG mice were fed DOX for intervals matching TetON-HIF-1 mice. As DOX day 0 (d0) TetON-HIF1 and NTG mice were phenotypically, microscopically, and molecularly similar, either genotype was used as a control in appropriate experiments. Transgene mRNA was upregulated within 24 hr of DOX provision and remained elevated during continuous induction (Fig. 23A). DOX-regulated transgene expression was slightly leaky at the mRNA level (data not shown), but tight at the protein level (Fig. 23B). The mRNAs of two canonical HIF-1 target genes, GLUT1 and carbonic CAIX, were rapidly induced and persistently elevated during continuous DOX exposure (Fig. 23A).

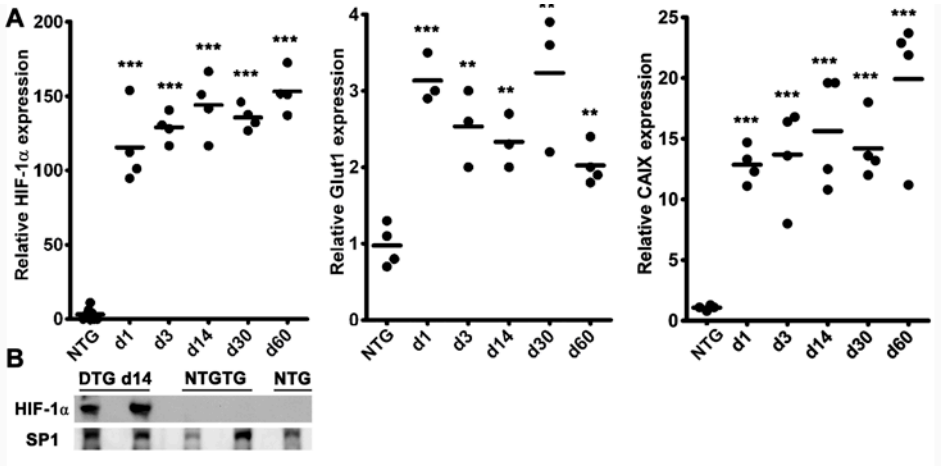

Fig. 23. DOX HIF-1α$^{P402A/P564A/N803A}$ transgene induction and target gene upregulation. (A) Real-time RT-PCR analysis of rapid and sustained elevations of transgene and "canonical" HIF-1 target gene mRNA's represented by GLUT1 and CAIX in TetON-HIF-1 transgenic (denoted as "DTG" double transgenic) compared to NTG mice during continuous DOX induction. Prior analysis demonstrated no difference between NTG and DOX d0 TetON-HIF-1 controls. (B) Transgene protein expression from Western blots of ear nuclear extracts on DOX d14 in DTG, single TRE-HIF-1α$^{P402A/P464A/N803A}$ transgenic mice (NTGTG), or NTG controls. Each dot in scatter plots represents one mouse.

Horizontal bars represent the mean. Gene expression measurements for HIF-1α, GLUT1 and CAIX were from the same samples. DTG data at each DOX day were compared with NTG or TetON-HIF-1 d0 data (data not shown), using unpaired Student's t-test (**P<0.01 and *** P<0.001).

1.2.2. Epithelial HIF-1 activation produces angiogenesis and a patterned microvasculature

DOX-induced TetON-HIF-1 mice developed skin redness and vascular prominence, noticeable on d3 of continuous DOX induction and peaking by DOX d14 (Fig. 24A). Histopathology was confined to the stroma, which displayed an increase in microvessels and mononuclear cells (data not shown). Vascular density increased four-fold by d14 (Fig. 24B, D) with microvessels decorating the undersurface of the interfollicular epidermis and the hair follicles (Fig. 24B). Whole mounts revealed development of a patterned neovasculature surrounding each hair follicle (Fig. 24C). This microvessel organization was produced by keratin-5 rtTA induction in hair follicle outer root sheath cells and sebaceous glands[93] (Fig. S1A). Endothelial tip cells with filopodia extending toward the transgene expressing epidermal cells were also detectable on d3 of continuous DOX induction (Fig. S1B).

1.2.3. Noninvasive determination of microhemodynamics during neovascularization

Label-free noninvasive L-PAM (Fig. S2) monitoring of individual DOX-induced TetON-HIF-1 transgenic mice from d0–60 demonstrated a progressive four-fold elevation in total

microvessel volume, concordant with immunofluorescent vessel density analysis (Fig. 24B, D, and Fig. S2E). L-PAM also resolved the perifollicular neovascular capillaries**,** as well as their afferent and efferent vessels (Fig. 24C, light blue and yellow arrowheads in the red boxed L-PAM close-up). 2-D projection images (Fig. 24B) further revealed extensive dilatation, tortuosity, and remodeling of large-caliber arteriovenous vessels during continuous epithelial HIF-1 activation (Fig. S2D, F–G). Using L-PAM's resolution and depth-sectioning capability, we determined the kinetics of capillary versus arteriovenous volume changes for extended intervals following HIF-1 induction, based on vessel caliber and 3-D morphology[41, 94] (Fig. S2D–E). Capillary volume tripled on d3, then abruptly increased to a 15-fold elevation by d14 predominantly due to capillary genesis. Capillary volume remained at the same elevated level from d14–60. In contrast, arteriovenous vessel volume expansion was more gradual, modest, and persistent, reaching a 3- to 4-fold elevation by d60. Arteries and veins also evidenced increased tortuosity, defined as the ratio of the vessel length to the linear distance between two adjacent bifurcation points, between d14–60 (Fig. 24B, Fig. S2D, F, G). The volume increase for the entire neovasculature was similar to that of the arteriovenous network, which comprised the majority of total vessel volume (Fig. S2E**)**. NTG mice treated with DOX from d0–60 evidenced no change in vessel density or volume either by L-PAM or immunofluorescence (Fig. S2C, E, F). Collectively, these L-PAM and vascular density data demonstrate that TetON-HIF-1 neovascularization comprises two stages following DOX-HIF-1 induction: a development stage consisting of angiogenesis, microvessel growth, and organization into perifollicular microvascular clusters, and a maintenance

stage wherein the capillary network is metastable (see below) and the arteriovenous vessels continuously remodeled.

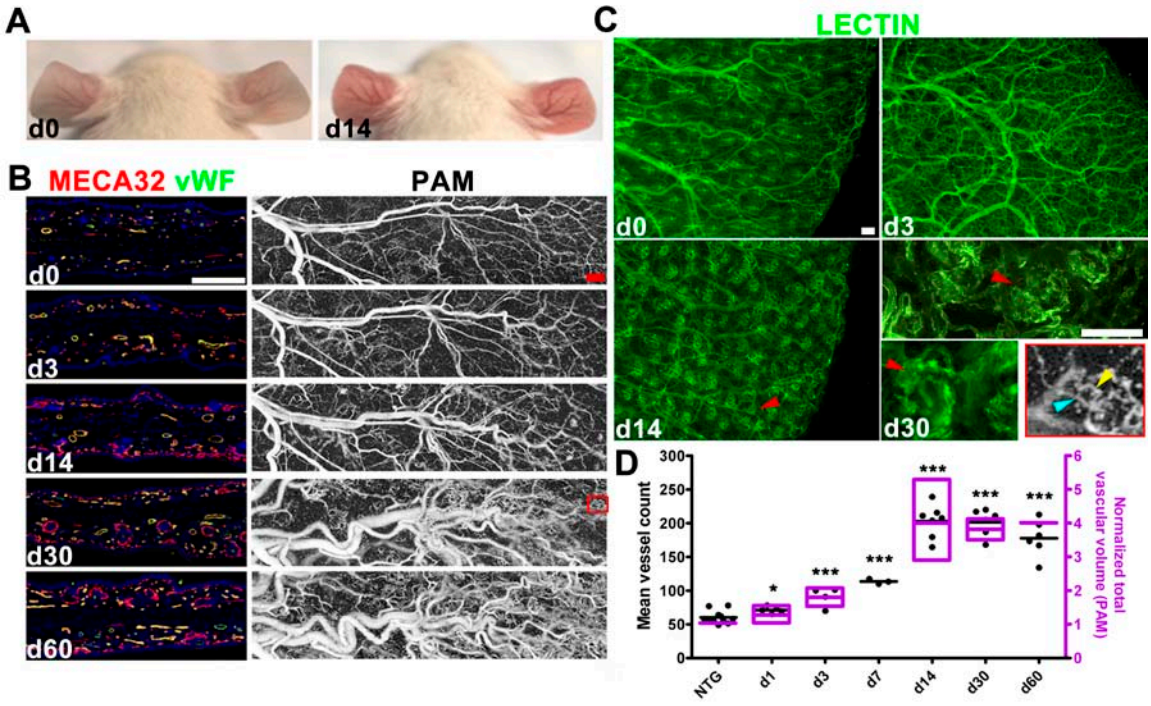

Fig. 24. Multistage angiogenesis, microvascular network patterning, and serial noninvasive imaging of neovascularization by L-PAM in TetON-HIF-1α transgenic mice. (A) Neovascular phenotype of a TetON-HIF-1 transgenic mouse with skin redness and vascular prominence developing 14 days following continuous DOX provision. (B) Comparative determination of TetON-HIF-1 neovascularization using immunofluorescent thin section microvessel markers, MECA32/vWF, with L-PAM. L-PAM was performed in the same transgenic mouse serially imaged for 60 days [red box indicates the microvascular domain magnified in (C)]. (C) Ear whole mount images of FITC-*Lysopersicon esculentum* perfused TetON-HIF-1 mice over time (red arrowheads in d14 and d30 images indicate neocapillaries surrounding each rtTA/HIF-1 expressing hair follicle). The L-PAM image insert (in gray scale) and the d30 high power whole

mount micrograph show similar conformation of the perifollicular neocapillaries. The light blue arrowhead points to the afferent vessel, while the yellow arrowhead points to the efferent vessel. (D) Microvascular density as determined by vessel counting of MECA32/vWF double immunofluorescence tissue sections *ex vivo*, and microvessel volume derived from *in vivo* L-PAM of serially imaged individual TetON-HIF-1 mice (n=1–4 for indicated time points) normalized to NTG controls, demonstrating the same trend of rapid elevation and then plateau by d14. Data for each DOX day were compared with NTG or TetON-HIF-1 d0 data (data not shown), using unpaired Student's t-test (*P<0.05, **P<0.01 and *** P<0.001 Bars: (B), 200 µm; (C), 100 µm.

1.2.4. Dynamics of microvascular regression following transgene withdrawal, independent of endothelial pericyte coverage

Temporal HIF-1 control allowed us to determine mechanisms of microvascular stability or regression following transgene and consequent angiogenic factor withdrawal. HIF-1 was DOX- induced for 14, 30, or 60 days to produce a neovasculature, then withdrawn for increasing intervals ranging from 1–60 days (Fig. 25A–B). Microvessel persistence was exquisitely dependent on continuous epithelial HIF-1 function, with a two-fold overall reduction of vascular density upon DOX withdrawal (Fig. 25B). Whole mounts demonstrated a marked dropout of perifollicular microvessels as early as post-withdrawal d3, with persistence of neovessels that developed at the greatest distance from the transgene expressing hair follicles (Fig. S3A). Overall there was a permanent 30% microvessel increment compared to controls (Fig. 25A, B, and Fig. S3A). Longer periods of transgene expression, either for 30 or 60 days, did not produce further increases in

permanent neovessels (Fig. 25B). Endothelial and perivascular cell apoptosis was activated as early as d1, peaked on d3, and fell to near baseline levels by withdrawal d14 (Fig. 25C). Apoptotic endothelial cells were most frequently detected immediately adjacent to the formerly transgene-expressing hair follicle basal cells (Fig. 25C, white arrowheads**).** These data suggested that these microvessels were "addicted" to high angiogenic factor levels, whereas microvessels developing at a distance from the transgene expressing hair follicles became angiogenic growth factor independent. DOX withdrawal experiments defined the third stage of TetON-HIF-1 neovascularization, HIF-1-dependent microvessel regression.

The high resolution and large FOV of L-PAM functionally delineated the entire process of neovascular regression (Fig. 25A, middle column). Magnified images showed the preexisting arteriolar-venular feeder loop on d0, and perifollicular neovessel establishment by d14 with feeder loop dilatation (Fig. 25A, right column). On withdrawal d3, these neovessels were intact, though of markedly decreased luminal diameter, as individual RBCs with intervening gaps, likely plasma, were delineated by L-PAM (Fig. 25A, purple arrowhead, each white dot represents a single RBC). By withdrawal d14, most of these neovessels regressed with persistence of the peripheral capillary ring.

As pericytes can convey microvascular stability, we predicted that they would be sporadically or loosely associated with TetON-HIF-1 capillary endothelial cells, given the marked microvessel transgene dependence (see next section), and the multiple potential angiogenic HIF-1 target genes.[95] Moreover, we also predicted that endothelial pericyte coverage would be lacking or sparse on development stage microvessels, as previously reported in studies of postnatal retinal vascular development.[96] However,

neither prediction was correct in TetON-HIF-1 mice. Desmin positive pericytes tightly covered each microvessel throughout neovascular development and maintenance, from d0 to d30, including vessels closest to high level multi-angiogenic growth factor expression, the perifollicular and subepidermal microvasculature (Fig. 25D, E, and Fig. S3B). We also delineated dynamic alterations in pericyte marker expression. While desmin was constitutively present in perivascular cells, PDGFRβ and NG2 expression were undetectable during DOX d1–3, then upregulated by d14, but again undetectable by DOX d30 (Fig. S3B). αSMA expression was restricted to large caliber stromal arteries and veins (Fig. 25D). These data reveal that the type of pericyte marker expressed on neovessels is temporally regulated, and in addition, controlled by the microvessel tissue and biologically context.[97]

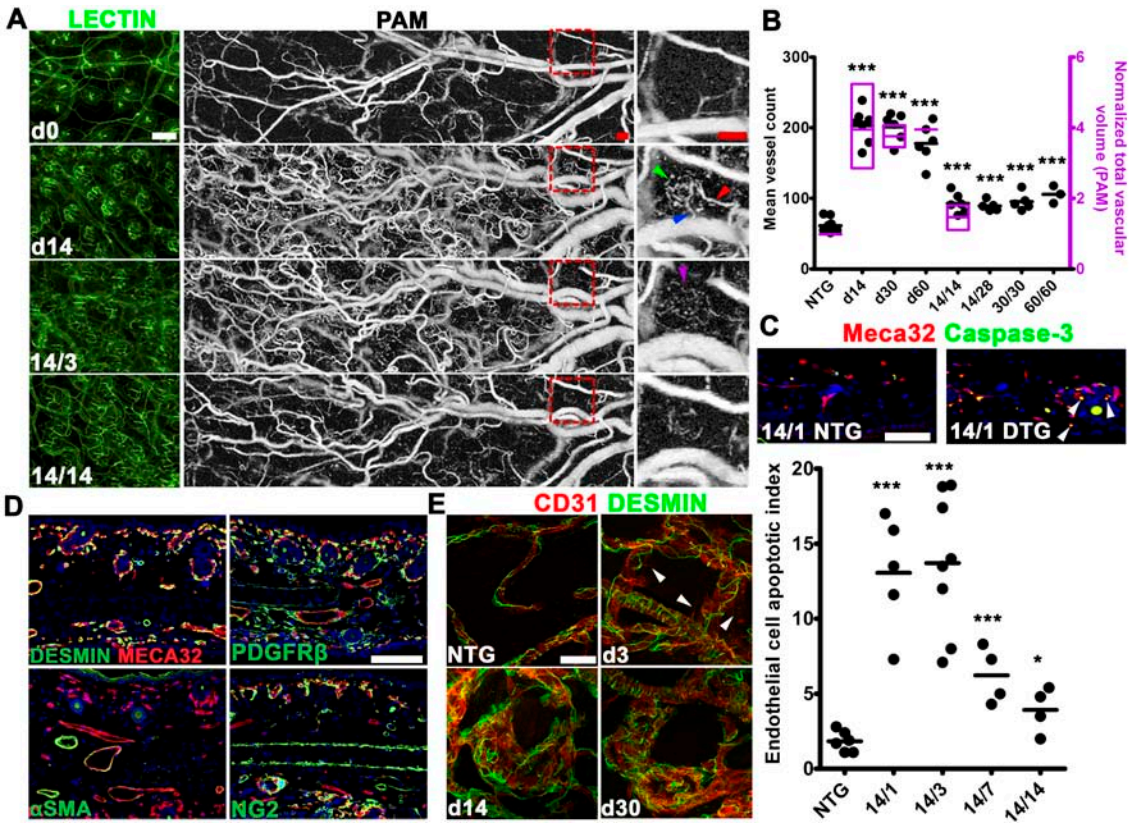

Fig. 25. Pericyte marker expression and microvessel stability following HIF-1 withdrawal. (A) Representative lectin-perfused whole mounts (left column) and L-PAM images (middle and right columns) during HIF-1 induction (d0, d14) followed by DOX withdrawal 14/3 (14d ON/ 3d OFF), 14/14 (14d ON/ 14d OFF). Neocapillaries that developed farthest from the hair follicles remain after withdrawal accounting for a persistent 30% increase in vascularity compared to DOX d0 or NTG controls. L-PAM images are obtained from the same TetON-HIF1 transgenic mouse imaged over 28 days. L-PAM detects development of perifollicular neocapillary unit (green arrowhead) with its feeder arteriole (red arrowhead) and draining venule (blue arrowhead), capillary luminal diminution with "single file" RBCs on withdrawal d3 (purple arrowhead), and involution with persistence of peripheral microdomain capillaries by withdrawal d14 (right column). (B) Quantification of microvessel density (MECA32 immunofluorescence, in black) and volume (L-PAM, in purple) in TetON-HIF-1 on DOX d14, d30, and d60, and following increasing intervals of DOX activation followed by commensurate periods of withdrawal, 14/14, 14/28, 30/30, and 60/60 (n=1–5). (C) Induction of perifollicular endothelial cell apoptosis (dual positive, $MECA32^{+}$/caspase-3^{+} cells, arrowheads right panel) following one day of DOX withdrawal (upper panel), and quantification of apoptotic indices over time (bottom panel). (D) Thin section dual endothelial (MECA32) and pericyte marker immunofluorescence demonstrates coverage of TetON-HIF-1 DOX d14 induced microvessels by desmin, PDGFRβ, and NG2. αSMA is expressed only in vascular supporting cells of deep stromal large vessels. (E) Confocal immunofluorescence demonstrates extensive and intimate microvessel coverage by desmin (+) pericytes at all time points following DOX induction (arrowheads delineate endothelial tip cells also

shown in detail in Fig. S1B). TetON-HIF-1 data at each DOX day were compared with NTG or TetON-HIF-1 d0 data (data not shown), using unpaired Student's t-test (*P<0.05 and *** P<0.001). Bars: (A) and (D), 100 μm; (C), 50 μm; (E), 20 μm.

1.2.5. Epithelial HIF-1 activation upregulates angiogenic target genes and produces persistent VEGFR2 signaling discordant with endothelial proliferative quiescence

To probe the molecular underpinnings of epithelial HIF-1-mediated neovascularization and regression, we determined DOX-induced alterations of angiogenic HIF-1 target genes (Fig. S4A–C). VEGF, PlGF, PDGF-B, and iNOS mRNAs rapidly increased, then plateaued or decreased. ADM, SDF1α, and angiopoietin-2 slowly rose, whereas thrombospondin-1, an angiogenesis inhibitor and a target of suppression by hypoxia,[98] progressively decreased. VEGF and PlGF protein were both persistently upregulated 20–60 and 4–20 fold, respectively (Fig. 26A), with a comparatively modest 1.9 fold SDF1α peak induction.

Continuous angiogenic growth factor expression led us to determine endothelial proliferation kinetics. Initiation of endothelial proliferation required 24hr of transgene activation (Fig. 26B and Fig. S4D). Proliferation peaked on d3 but exponentially decreased thereafter (Fig. 26B). As prolonged endothelial cell VEGF stimulation can produce divergent effects on VEGFR2 protein expression, either downregulation[99, 100] or induction and maintenance,[101] we hypothesized that diminution of receptor expression or activation would be associated with cessation of proliferation in TetON-HIF-1 endothelium. However, whole tissue levels of both total and Y^{1173} VEGFR2 in DOX d0–

60 TetOn-HIF-1 ears were persistently elevated 6–10 fold compared to controls (Fig. 26C and Fig. S5A). Fluorescence microscopy demonstrated persistent endothelial VEGFR2 expression and receptor upregulation in perifollicular and subepidermal endothelial cells (Fig. S5B). Confocal microscopy revealed temporally regulated VEGFR2 intracellular compartmentalization. VEGR2 was induced and localized in paranuclear vesicles on d3 (Fig. S5C, arrowheads), then redistributed throughout the cytoplasm and plasma membrane from d14–30. The major VEGFR2 signaling outputs, AKT, Src, PLCγ, and ERK phosphorylation, each persistently increased 2–6 fold, from d1 to d30 (Fig. 26C and Fig. S5A). Cyclin D1 was also persistently upregulated 2–6 fold following transgene induction (Fig. 26C and Fig. S5A). Immunofluorescence localized cyclin D1 expression to TetON-HIF-1 endothelial cell nuclei (Fig. 26D). Thus neither downregulation of VEGFR2 expression, activation, and signaling outputs, nor persistent G1 activation, was responsible for the temporally regulated, intrinsic endothelial cell proliferative resistance in the context of continuous angiogenic growth factor stimulation.

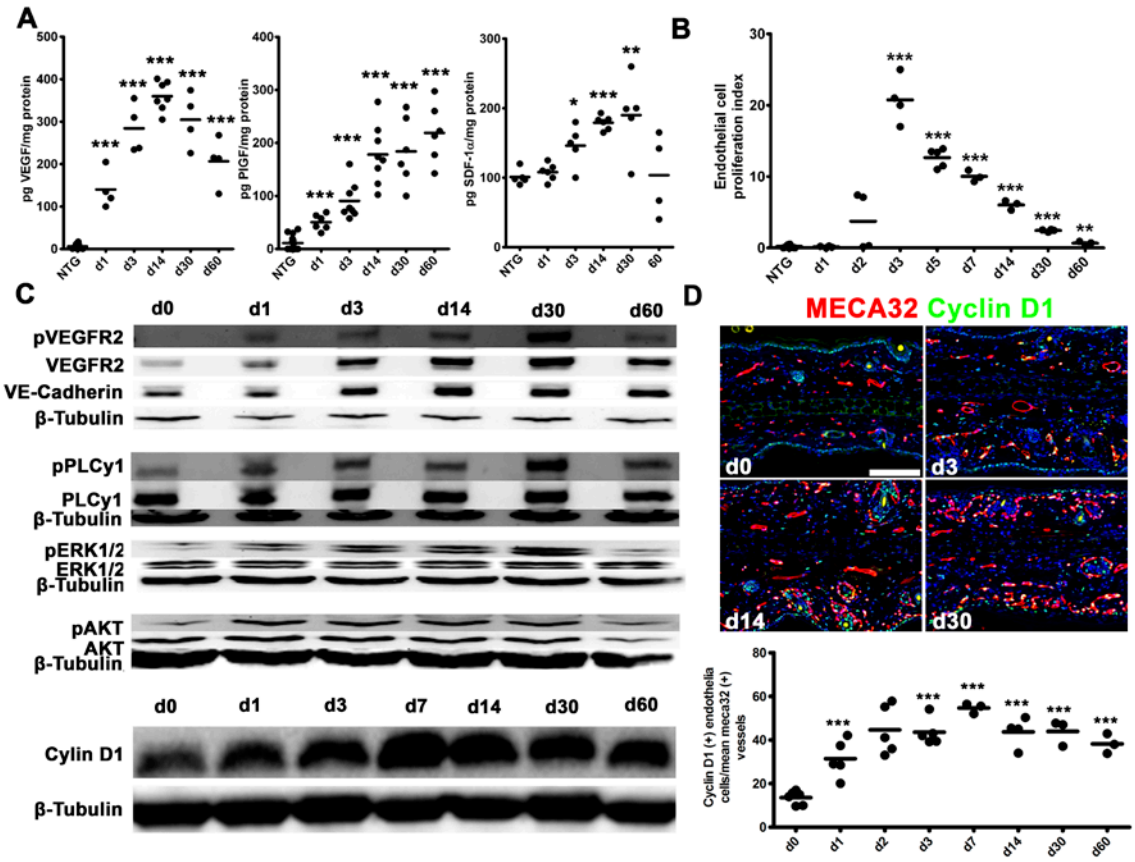

Fig. 26. Upregulation of HIF-1 angiogenic factor transcriptional targets, persistent VEGFR2 signaling and intrinsic downregulation of endothelial proliferation in TetON-HIF-1 transgenic mice. (A) Ear tissue ELISA's for VEGF (left), PIGF (middle) and SDF1 (right). Immediate d1 increase of VEGF and PlGF contrasts the gradual SDF1 induction between d3–30. (B) TetON-HIF-1 endothelial cell proliferation kinetics determined by counting double-labeled BrdU/MECA32 (+) endothelial cells in 4–6 10X fields per thin section normalized to the microvascular density. (C) Representative Western blot analysis of total ear tissue lysates for VE-Cadherin, total and phosphorylated: VEGFR2(Y1173), PLCγ(Y783), ERK1/2(T202/Y204), and AKT(S473), and cyclin D1. (D) Representative immunofluorescent images (top) and quantification (bottom) of cyclin D1. TetON-HIF-1 data at each DOX day were compared with NTG or

TetON-HIF-1 d0 data (data not shown), using unpaired Student's t-test (*P<0.05, **P<0.01 and *** P<0.001). Bar: 100 μm.

To further probe mechanisms of endothelial proliferation downregulation, we determined the kinetics of cell cycle repressors in TetON-HIF-1 tissue extracts. Activated phospho-p53^{S20} was elevated 3-fold coincident with d3 peak endothelial proliferation, and remained 3–7 fold increased to d30 (Fig. 27A and Fig. S6A). The p53 target p21 was also induced 4-fold at peak endothelial proliferation and remained persistently elevated (Fig. 27A and Fig. S6A). Immunofluorescence revealed p21 induction and persistence in endothelial cell nuclei [Fig. 27B (white arrowheads), and Fig. 27D]. As these data suggested replication stress as a mechanism for cell cycle inhibition, we probed tissue extracts for activation of the stress/DNA damage mediator γH2AX. γH2AX was induced 50-fold by d3, with further increases in protein expression between d14-30. Expression at d60 remained 16-fold elevated compared to d0 (Fig. 27A and Fig. S6A). Immunofluorescence also revealed endothelial cell nuclear γH2AX induction [Fig. 27C**,** **(**white arrowheads)]. Quantitative analysis delineated a 5-fold elevation of γH2AX positive endothelial cell nuclei by d3 and sustained at that level thereafter (Fig. 27D). Further analysis of the d0 and d3 time points using confocal microscopy, identified endothelial cells containing multiple γH2AX positive nuclear foci (Fig. S6B, and data not shown).

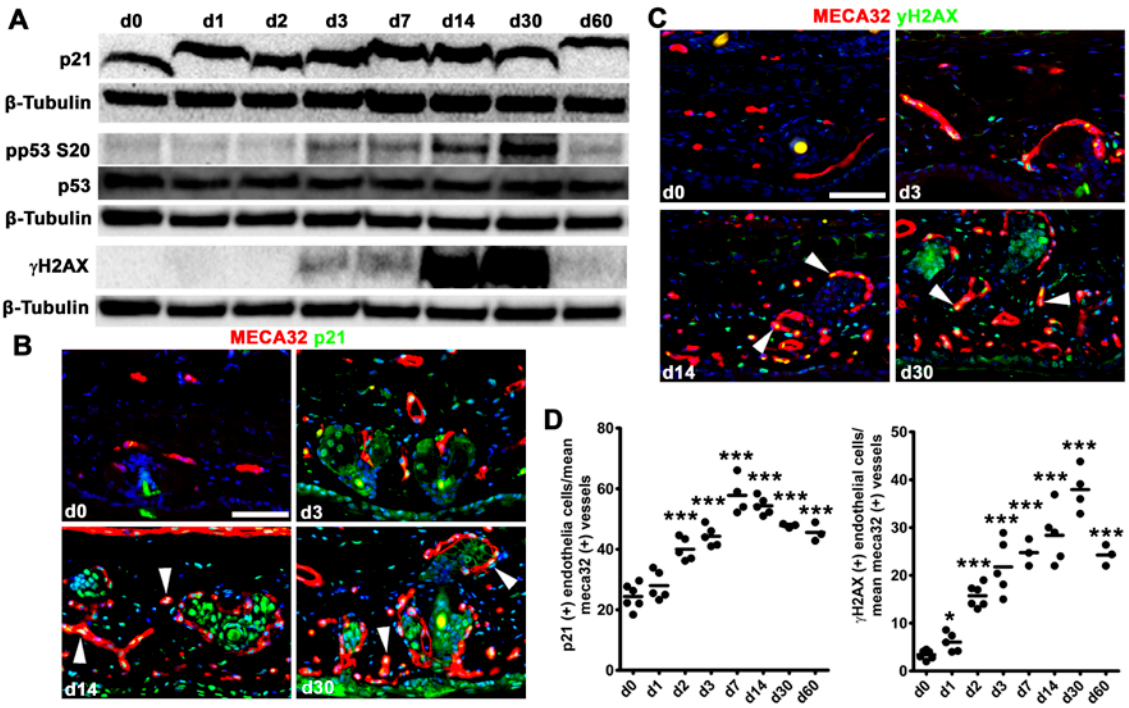

Fig. 27. Activation of epithelial HIF-1 induces a DNA damage/replication stress checkpoint. (A) Western analysis of p21, total and phosphorylated $p53^{S20}$, phosphorylated γH2AX, reveals induction of cell cycle inhibitors consistent with replication stress beginning at peak endothelial proliferation (Fig. 26). (B–C) Representative thin ear tissue immunofluorescent images of p21 (B) and γH2AX (C). White arrowheads point to p21 and γH2AX positive endothelial cells. (D) Quantification of p21 and γH2AX expression determined by vessel counting of MECA32/p21 and MECA32/γH2AX double immunofluorescence tissue sections *ex vivo*. TetON-HIF-1 data at each DOX day were compared with TetON-HIF-1 d0 data, using unpaired Student's t-test (*P<0.05, **P<0.01 and *** P<0.001). Bar: 50 μm.

1.2.6. Stage-specific differential responsiveness to VEGFR1/2 inhibitors

TetON-HIF-1 multistage angiogenesis was a unique platform to temporally dissect the

functional contributions of VEGFR2 or VEGFR1 signaling to neovascularization. Day 0–14 VEGFR2 immunoblockade with DC101[102] produced a 2.3-fold reduction in microvessel density primarily due to inhibition of perifollicular neovessel formation (Fig. 28A, B, and Fig. 29A). Western blotting revealed a 10-fold diminution of VEGFR2 phosphorylation in this same interval (Fig. 28C, and data not shown). *In vivo*, noninvasive L-PAM image extraction analysis detected a 2.9-fold diminution in capillary volume that nearly matched microvessel counting of tissue sections, whereas elevated arteriovenous and total vessel volumes were unaffected (Fig. 28B). VEGFR1 blockade by MF1[103] did not affect d0–14 microvessel density (Fig. 29A), while a DC101/MF-1 cocktail was similar to single-agent DC101 (data not shown).

In contrast to d0–14, there was resistance of the TetON-HIF-1 microvasculature to either single-agent DC101 or DC101/MF-1 cocktail deployment between d14–28 that was also evident in the L-PAM data sets (Fig. 28A, B, and Fig. 29A). Microvessel density was reduced by only 20% compared to DTG d30 (Fig. 28B, left-most bar graph). Western analysis also mirrored resistance with a 2.5-fold reduction in phospho-VEGFR2 (Fig. 28C). L-PAM microvessel subset extraction analysis revealed only a 1.9-fold reduction in capillary, and essentially unchanged arteriovenous volumes during VEGFR2 (Fig. 28B**)** or combinatorial VEGFR1/2 blockade (data not shown). MF1 increased microvascular density by 30% during d14–28 (Fig. 29A, and data not shown), consistent with VEGFR1 function as VEGF "sink" on endothelial cells.

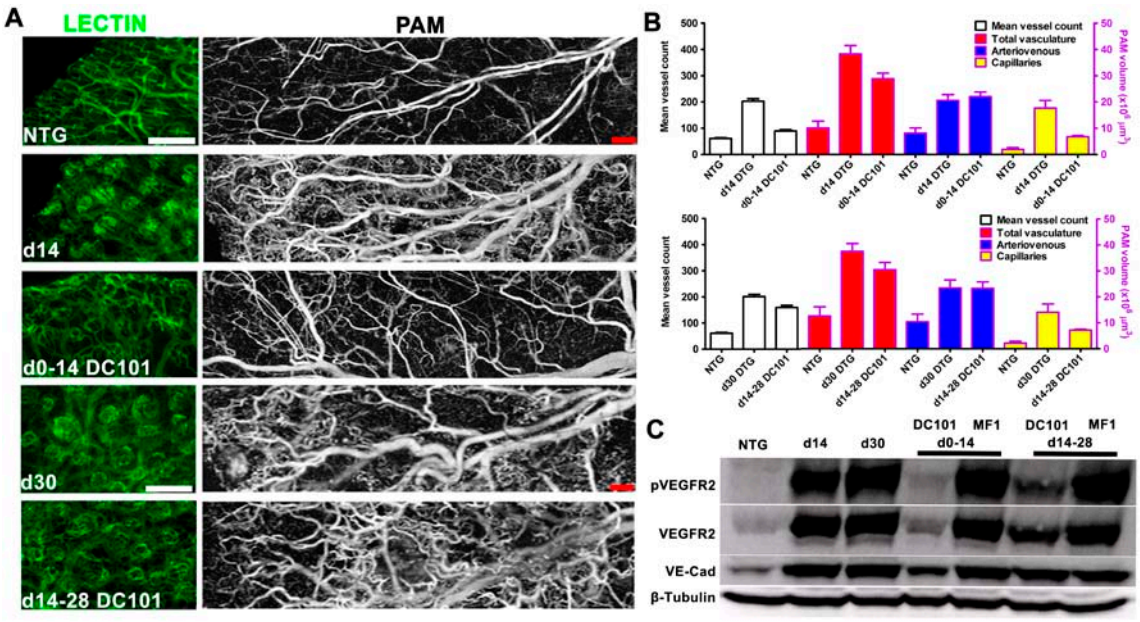

Fig. 28. Stage-specific resistance of the HIF-1 neovasculature to VEGFR1 and VEGFR2 immunoblockade. (A) Inhibition of the development (d0−14) versus resistance of the maintenance stage (d14−28) to VEGFR2 (DC101) immunoblockade as determined by lectin whole mount and L-PAM analysis. Both L-PAM and FITC-*Lysopersicon esculentum* perfused whole mounts demonstrate the marked sensitivity of perifollicular neocapillaries, while microvessels farthest from HIF-1 production are resistant to DC101. L-PAM also detected arteriolar and venular dilatation resistant to DC101 treatment in both stages. (B) Quantification of diminution of microvessel density by cross sectional MECA32/vWF immunofluorescence (white bars, immunofluorescence data not shown) or volume reduction delineated by image extraction L-PAM analysis during d0–14 (top) or d14-28 (bottom) VEGFR2 blockade (blue and yellow bars). (C) Western blotting analysis of vascular endothelial-cadherin (VE-Cadherin), VEGR2^{Y1173} and total VEGFR2 in mice treated with VEGFR1/2 blocking antibodies. Bars: 200 µm.

1.2.7. Stage-specific myeloid cell inhibitor responsiveness and dissociation of myeloid cells from neovascular development or maintenance

As myeloid cells enhance tumor or ischemic angiogenesis,[104] and contribute to angiogenic inhibitor evasion,[105] we tested for their recruitment and retention from d0–30 of HIF-1 activation. CD45, CD11b myeloid cells, mast cells and F4/80 macrophages were progressively recruited to the stroma during the TetON-HIF-1 d0–14 development stage, and were retained during the d14–30 maintenance stage (Fig. 29A, Fig. S7A, B, and Fig. S8C). Neutrophils were also recruited and retained during these stages though to a lesser extent than CD11b cells or F4/80 macrophages (Fig. S7C). Myeloid cell retention required continuous epithelial HIF-1 expression, as they rapidly disappeared from the stroma after 3 days, and returned to baseline levels by 14 days of DOX withdrawal (Fig. 29A).

To determine mechanisms of myeloid cell recruitment and retention, we first tested for endocrine angiogenic growth factor secretion from DOX-activated skin. There was a rapid 2.5- and 15-fold elevation of plasma VEGF and PIGF, respectively, on DOX d1, both falling to control levels by d30 (Fig. 29B). In contrast, plasma SDF1 was only 1.4–1.5 elevated on d3 and 14, returning to baseline by d30 (Fig. 28C, right panel). Transient elevation of these angiogenic growth factors in plasma contrasted with their continual high-level expression in tissue (Fig. 26A, and Fig. S4A–C). Peak splenic enlargement followed peak growth factor plasma levels by two days, gradually decreasing by d30; associated with an increase in red pulp and perifollicular accumulation of F4/80 and CD11b macrophages (Fig. S8A, data not shown). A bone

marrow origin for the recruited myeloid cells was suggested by autologous bone marrow transplantation using CAG-EGFP donor cells (Fig. S7D).

As previous work demonstrated the principal involvement of the VEGF/PlGF/VEGFR1 signaling module in recruitment,[106] and SDF1/CXCR4 engagement in retention,[79, 107] we tested inhibitors of these signaling axes in both the development and the maintenance stages. As expected, either MF1-mediated VEGFR1 or DC101-mediated VEGFR2 immunoblockade abrogated myeloid cell recruitment during the development stage (Fig. 29A). However, the presence of robust neovascularization in the absence of stromal myeloid cells revealed by VEGFR1 blockade was unexpected (Fig. 29A). CXCR4 blockade by AMD3100 did not alter development stage myeloid cell recruitment or neovascularization (Fig. 29A). While maintenance stage myeloid cell retention was unaffected by either single-agent DC101 or MF-1, it was nearly abrogated by a DC101/MF1 “cocktail” (Fig. 29A, and Fig. S8C). Potent inhibition of myeloid cell retention again revealed a striking disconnection between loss of stromal myeloid cells and persistence of the HIF-1 neovasculature. AMD3100, used at doses previously shown to decrease tumor and VEGF-mediated myeloid cell retention and hypervascularity,[79, 88] failed to affect either myeloid cell or microvascular density in the maintenance stage (Fig. 29A, and Fig. S8C). Consistent with its low level induction by ELISA and AMD3100 treatment resistance, SDF1, though upregulated in TetOn-HIF-1 basal keratinocytes (Fig. S8B) was rarely detectable in perivascular[79] or endothelial cells.[107]

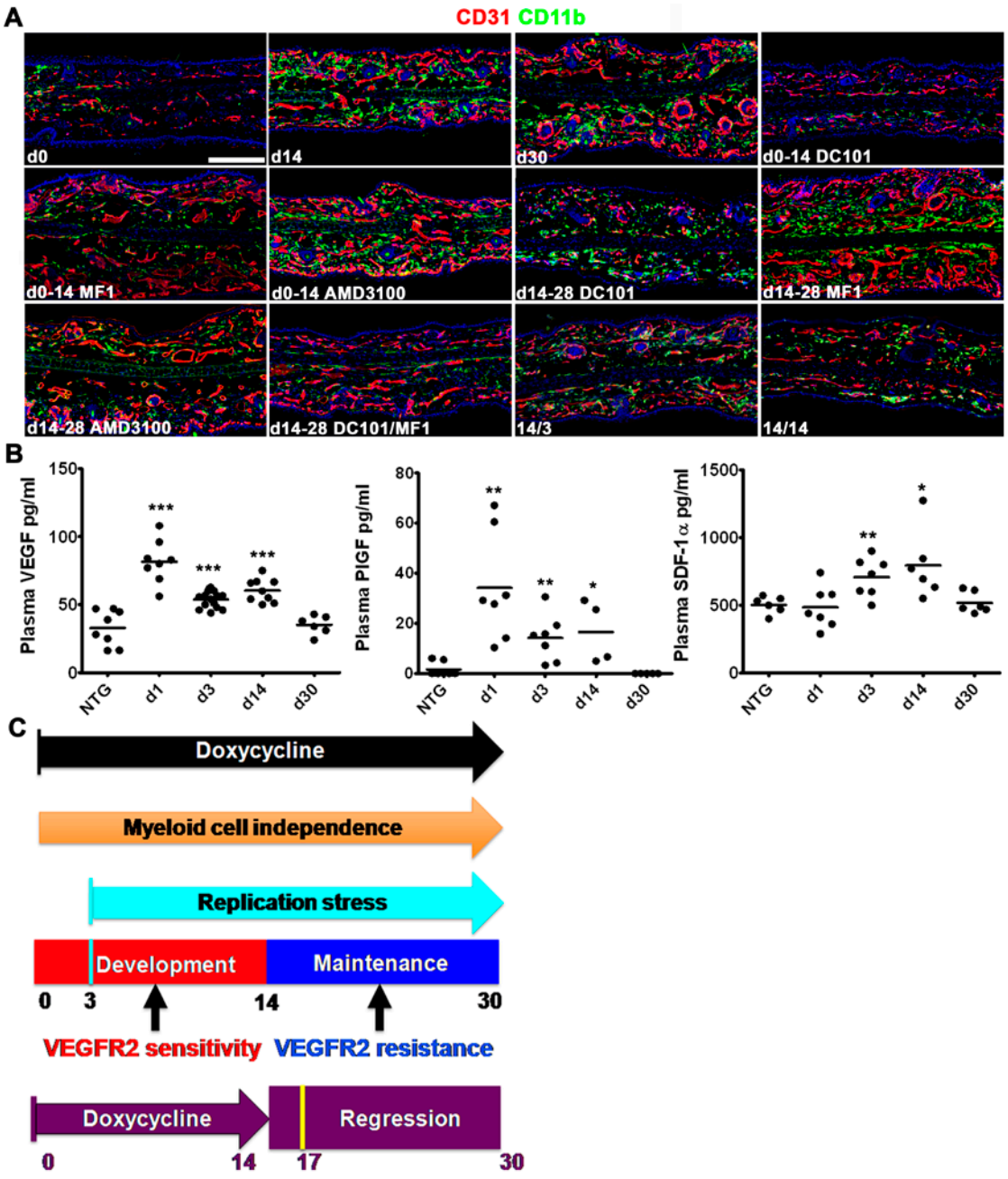

Fig. 29. Stage-specific regulation of stromal myeloid cell recruitment and retention, and model of epithelial neovascularization regulated by HIF-1. (A) Representative CD31/CD11b co-immunofluorescence demonstrating recruitment and stromal accumulation of CD11b myeloid cells during the TetON-HIF-1 DOX d0–14 neovascular development stage, with HIF-1-dependent retention of these cells from d14–28. Myeloid

cell recruitment is dependent on either VEGFR1 (MF1) or VEGFR2 (DC101), but independent of CXCR4 (AMD3100) signaling. Note that in MF1-treated TetON-HIF-1 mice neovascular development proceeds despite marked inhibition of myeloid cell recruitment. DOX d14–28 myeloid cell retention is independent of either VEGFR1 or VEGFR2, but dependent on signaling from both receptors. Myeloid cell retention is only partially inhibited by AMD3100 (even less evident in CD45 immunofluorescence, Fig. S8). Note the persistence of maintenance stage neovasculature despite profound stromal myeloid depletion in the d14–28 DC101/MF1 inhibitor cocktail treated TetON-HIF-1 mice. Marked stromal myeloid cell depletion following 3 (14/3) and 14 (14/14) days of DOX withdrawal. (B) Plasma VEGF (left), PIGF (middle) and SDF1 (right) expression levels in TetON-HIF-1 mice and DOX NTG controls determined by ELISA. (C) Continuous HIF-1 activation produces multistage intrinsically regulated neovascular development, maintenance, and transgene dependent regression. Mechanisms of myeloid cell recruitment and retention were stage-specific. Resistance to VEGFR2 immunoblockade was also stage-specific. The cyan bar indicates peak proliferation achieved at d3. The dark orange arrow depicts neovascular growth and maintenance independent of myeloid cells. The purple arrow denotes 14 days of continuous DOX induction, while the purple bar signifies 14 days of DOX withdrawal. The yellow bar peak indicates peak apoptosis and L-PAM-determined capillary luminal constriction three days post DOX withdrawal. TetON-HIF-1 data at each DOX day were compared with NTG or TetON-HIF-1 d0 data (data not shown), using unpaired Student's t-test (*P<0.05, **P<0.01 and *** P<0.001). Bars: 200 μm.

1.3 Discussion

Here, using detailed kinetic analysis, we discovered that neovascular development was intrinsically regulated by a DNA damage checkpoint in endothelial cells coincident with peak endothelial proliferation. Each neovascular stage also possessed distinctive vascular and myeloid cell responses to angiogenesis inhibitors (Fig. 29C). TetON-HIF-1 mice enabled development of L-PAM, which noninvasively and without intravenous contrast, mapped neovascular network architecture and vessel volumetric changes during emergence, maintenance, regression, or angiogenesis inhibitor responsiveness.

Cell autonomous inhibition of TetON-HIF-1 endothelial cell proliferation was surprising given the continuous microvessel exposure to elevated levels of angiogenic factors. Persistent VEGFR2 expression and activation was unexpected, because RTKs as a class are downregulated via internalization and degradation following growth factor activation.[108] However, VEGFR2 cell biology is complex, with contextual regulation of expression level, intracellular compartmentalization, and signaling.[99, 101, 109] Our study was a first in kind demonstration of *in-vivo* VEGFR2 internalization to paranuclear vesicles, consistent with either caveosomes or endosomes. These data suggested that VEGFR2 redistribution from the vesicular compartment to the plasma membrane could be responsible, in part, for the diminution of endothelial cell proliferative signaling in tissues as implied by several studies using cultured endothelial cells.[110-112] However, a more attractive mechanism for cell autonomous regulation of endothelial proliferation was induction of replication stress due to continuous endothelial cell stimulation by angiogenic growth factors, here predominantly VEGF.[113] Support for this hypothesis was based on several pieces of data, including persistent VEGFR2 expression and

phosphorylation, continuous cyclin D1 upregulation in endothelial cells, and induction and sustained expression of endothelial cell p21 and γH2AX. Localization of γH2AX to nuclear foci, consistent with DNA strand breaks, was also compelling data in support of replication stress.[114] Prior work demonstrated that γH2AX was required for neovascularization in ischemia and in growing tumors.[115] However that work suggested that γH2AX predominantly regulated endothelial proliferation during hypoxia. Here we demonstrated that replication stress and γH2AX were likely important for regulation of endothelial proliferation in normoxia and in response to continuous angiogenic factor stimulation. One possible mediator of endothelial cell replication stress is HIF-1α. HIF-1α can induce a DNA damage response, in the absence of hypoxia, due to inhibition of Nbs1, a crucial component of the MRN DNA repair complex.[116] As HIF-1 is also a part of a VEGF-mediated autocrine signaling loop in endothelial cells,[87] MRN inhibition may be responsible for γH2AX induction in our model, and will be investigated in future studies. Collectively, these studies and our data highlight the ability of conditional models of neovascularization to uncover endothelial cell regulation mechanisms that are independent of disease.

The endothelial-pericyte biology during epithelial HIF-1-mediated neovascularization was unanticipated. Lack of detectable "naked" endothelial tubes subsequently recruiting pericytes was contrary to studies of the neonatal rodent retina.[96, 117] However, coincident pericyte-endothelial envelopment during microvessel assembly and pericyte-mediated endothelial tip cell guidance during stromal invasion have both been reported.[118-120] Intimate microvessel envelopment was also unexpected as HIF-1 created a tumor-like angiogenic growth factor milieu, which has been correlated with

loose pericyte-endothelial association.[121] Most surprising was the dissociation of pericyte coverage, transgene-dependent neovascular regression, and VEGF inhibitor resistance. As such, pericytes and vessel "maturation" could have been evoked as an explanation for VEGFR2 inhibitor resistance. However extensive pericyte coverage was insufficient to maintain the neovasculature following HIF-transgene withdrawal.

Stage-specific alteration of VEGF receptor regulation of stromal myeloid cell recruitment and retention was also unanticipated. Prevention of stromal myeloid cell recruitment in the development stage by MF1 was consistent with known mobilization and chemotactic functions of VEGFR1 on hematopoietic precursors.[122] DC101's inhibition of d0-14 myeloid cell recruitment was consistent with an abrogation of both endothelial cell luminal receptor upregulation and VEGF proinflammatory functions.[90] In contrast, maintenance stage myeloid cell retention was resistant to either MF1 or DC101, but exquisitely sensitive to dual VEGFR1/VEGFR2 immunoblockade. Previous work demonstrated VEGFR2 expression on tumor infiltrating myeloid cells.[123] Our data now suggest a functional role for VEGFR2 expression in myeloid cell retention that will need to be tested in disease models. Equally surprising was the minimal effect of CXCR4 blockade, particularly on myeloid cell retention. These results were in contrast with the potent ability of CXCR4 blockade to decrease both stromal myeloid cell retention and microvascular density in ischemia, tumor xenografts, and conditional VEGF induction models.[79, 88, 107] Our study suggests that SDF-1 signaling requirement for myeloid retention is cell context, tissue, and disease dependent. Most surprising was the persistence of the HIF-1 microvasculature during maintenance stage DC101/MF-1-mediated myeloid cell depletion, as these cells are the source of multiple angiogenic

factors responsible for VEGF inhibitor evasion or amplification of therapeutic angiogenesis in preclinical tumor or ischemia models.[88, 107, 124, 125] As such, our work highlights the fact that myeloid cell accumulation in angiogenic tissues does not necessarily support neovascular persistence. Rather the bona fide ischemic or tumor microenvironment is required for proangiogenic myeloid cell subset production.

PAM, combining optical excitation and ultrasonic detection has multiple attractive features. First, the endogenous hemoglobin absorption contrast enables PAM to identify RBC-perfused microvasculature, the functional vascular subset responsible for tissue oxygen supply.[126] Second, the one-way ultrasonic path enhances tissue transparency because acoustic scattering in biological tissues is much weaker (1000 times less) than optical scattering. Third, the combination of the high nonradiative quantum yield of hemoglobin, the perfect 100% sensitivity of PAM to optical absorption, and the enhanced tissue transparency enables imaging sensitivity down to the single RBC level with a low laser exposure (contrast-to-noise ratio is ~100:1 with 570-nm laser excitation).[127] Fourth, the combination of the contrast-free preparation and low-level laser exposure enables noninvasive repetitive imaging of chronic processes including, but not limited to, temporal angiogenesis. With the present L-PAM, we were able to dissect neovascular elaboration in TetON-HIF-1 mice at the capillary level in the same animal for prolonged observation intervals (60 days, or more if necessary). The feature extraction capability of L-PAM enabled determination of the differential responsiveness of capillaries versus arteriovenous vessels to angiogenic inhibitors. Emergent translational L-PAM advances are focusing on imaging and therapy monitoring for skin

cancer, breast cancer, and internal yet endoscopically accessible organs such as esophagus, colon, and bladder in cancer patients.

1.4 Conclusion

In summary, the TetON-HIF-1 mouse model revealed novel aspects of neovascular regulation divergent from previous preclinical studies but strikingly convergent with clinical challenges, facing both angiogenesis inhibitors in cancer and vascular restoration in ischemia. L-PAM's ability to both longitudinally image neovascularization and to segment microvessel subset responses to angiogenesis inhibitors dynamics will be a boon to the study of ischemic and tumor neovascularization.

1.5 Supplementary Figures

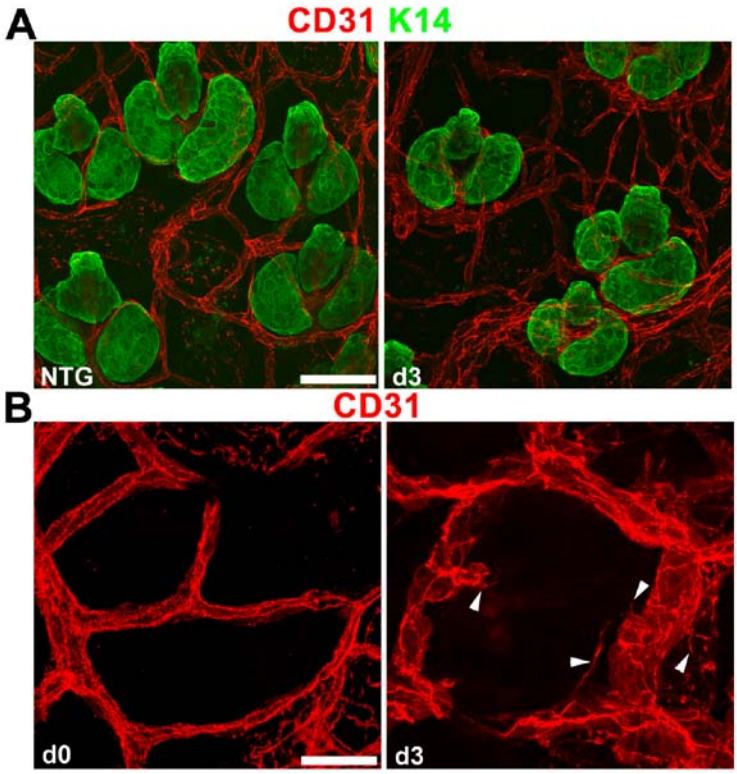

Fig. S1. Relationship of transgene expressing epithelial cells and neocapillary genesis in TetON-HIF-1 mice. (A) Representative ear whole mount demonstrating decoration of the K14/K5 (here K14) follicle outer root sheath keratinocytes and sebaceous glands (green) by CD31 (+) microvessel endothelial cells (red). Keratins -14 and -5 are coordinately expressed, and in TetON-HIF-1 mice the green cells express the HIF-1α transgene. (B) Representative whole mount CD31 immunofluorescence showing endothelial tip cells sprouting towards HIF-1-transgene expressing basal and sebaceous gland cells. Bars: (A), 50 μm; (B), 20 μm.

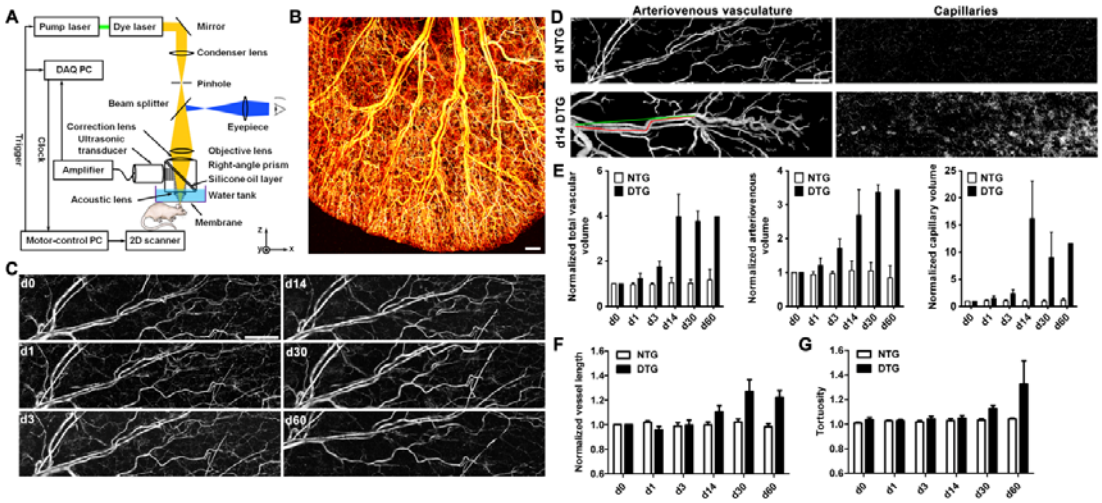

Fig. S2. Schematic of the L-PAM and differential capillary versus arteriovenous responsiveness to epithelial HIF-1 activation elucidated by L-PAM image extraction analysis. (A) A schematic of the L-PAM system. A short-pulsed laser beam is spatially filtered through a pinhole, and then is focused by a microscope objective to achieve micrometer resolution in living tissues. Wideband ultrasonic waves (referred to as photoacoustic waves) are induced as a result of transient thermoelastic expansion due to the laser excitation, and then detected by a high-frequency ultrasonic transducer to reveal

physiologically specific absorption properties of the tissue. (B) The depth-projected microvasculature of a DOX d14 TetON-HIF-1 mouse ear imaged with L-PAM. (C) Representative L-PAM images of an NTG mouse maintained on DOX from d0–60 demonstrates an unchanged microvasculature network. (D) Image extraction of L-PAM data to delineate arteriovenous truncal vessels (left column) versus capillaries in NTG and DOX d14 TetON-HIF-1 mice (right column). The capillaries are clustered consistent with localization in perifollicular microdomains as in Fig. 2C. (E) Quantitative analysis of extracted L-PAM data showing the initial increase and then plateau in vascular volume over time. Total vascular volume is biased by arteriovenous values, as they collectively comprise most of the total vascular volume. Note the marked differential fold elevation of capillary versus total vessel or arteriovenous volumes. These data are consistent with *de novo* development and persistence of perifollicular microdomains, in contrast to expansion and increased tortuosity of preexisting arteries, arterioles, veins and venules. (F). Vessel-axis tracing based on the extracted L-PAM data enables quantification of the vessel length (red curve in panel D) between two adjacent bifurcation points. (G). The ratio between the vessel length and the linear distance (green curve in panel D) represents vessel tortuosity. Bars: 500 µm.

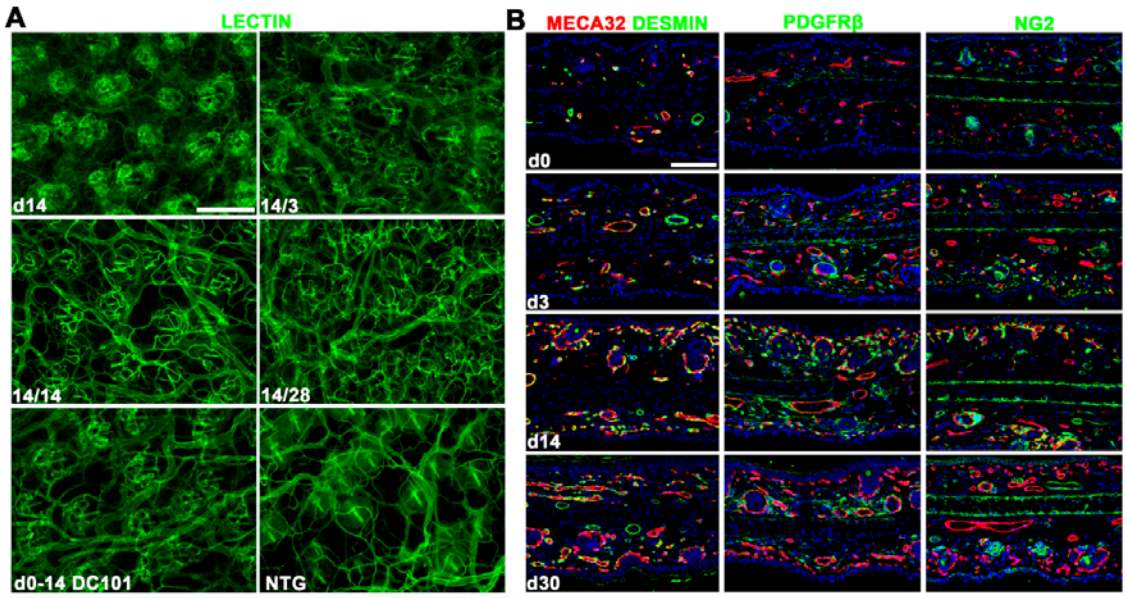

Fig. S3. Epithelial HIF-1 activation produces both transgene dependent and independent vessel subtypes, and dynamic alterations of pericyte marker expression over time. (A) FITC-*Lysopersicon esculentum* perfused ear whole mounts demonstrate perifollicular neocapillary development between d0–14, microvessel dropout evident by withdrawal day 3 (14/3), and persistence of the neovasculature that developed at a distance from the hair follicle units after 14 (14/14) or 28 (14/28) days of DOX withdrawal. DOX 0–14 VEGFR2 blockade (DC101) produces a similar microvascular pattern as 14 or 28d withdrawal with extensive central microdomain ablation. (B) Representative dual MECA32/Desmin (left column) or PDGFRβ (middle column) or NG2 (right column) immunofluorescent images. Desmin expression is persistent throughout the course of neovascular development and maintenance in TetON-HIF-1 mice. In contrast, HIF-1 activated pericytes incrementally express PDGFRβ and NG2 during the DOX d0–14 development stage, followed by downregulation of these markers during the DOX d14–30 maintenance stage. Bars: (A), 100 µm; (B), 200 µm.

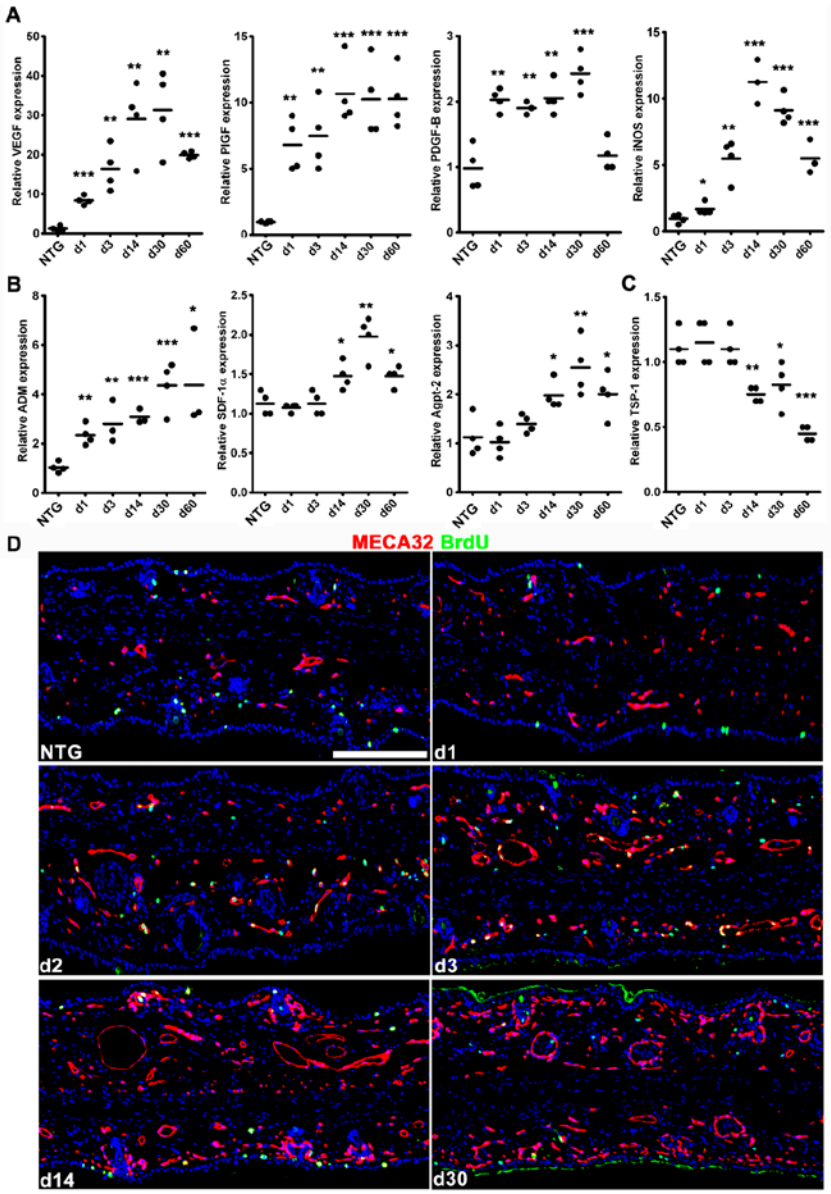

Fig. S4. DOX induction of HIF-1 pro- and anti-angiogenic target genes, and endothelial/perivascular cell proliferation. (A-C) RT-PCR determination of differential patterns of HIF-1 target gene mRNA upregulation (A-B), or diminution (C). (D) Dual MECA32/BrdU immunofluorescence demonstrating activation of endothelial proliferation 36–48hr following DOX provision, peak proliferation on d3 and decrease to baseline by d30–60. TetON-HIF-1 data at each DOX day were compared with NTG, using unpaired Student's t-test (***P<0.001, **p<0.01, * P<0.05). Bar: 200 μm.

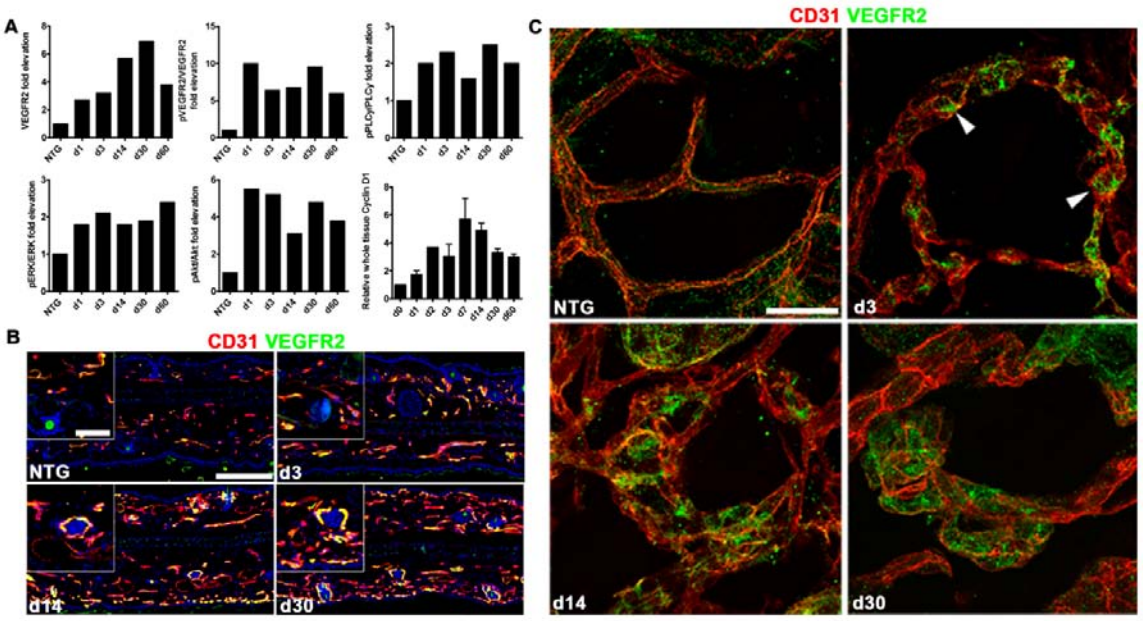

Fig. S5. Epithelial HIF-1 activation results in persistent VEGF-VEGFR2 signaling pathway activation. (A) Quantification of Western blot detection of total VEGFR2, differential phosphorylation of VEGFR2^{Y1173}, PLCγ^{Y783}, ERK$^{T202/204}$, AKT^{S473} and cyclin D1 induction and persistence. Immunoblots were adjusted for sample loading based on β-tubulin densitometry, and then ratios of phospho to total proteins were normalized to NTG DOX or d0 ratios. Graphs are representative of 2–4 independent experiments. (B) Dual CD31/VEGFR2 immunofluorescence shows progressive total VEGFR2 upregulation, with redistribution and persistent VEGFR2 expression in perifollicular endothelial cells. (C) Intracellular paranuclear vesicular localization of VEGFR2 (arrowheads) in TetON-HIF-1 mice on DOX d3 with more uniform distribution by DOX d14–30, determined by confocal microscopy of dual CD31/VEGFR2 immunofluorescence in ear whole mounts. Bars: (B), 200 μm, inset 50 μm; (C), 20 μm.

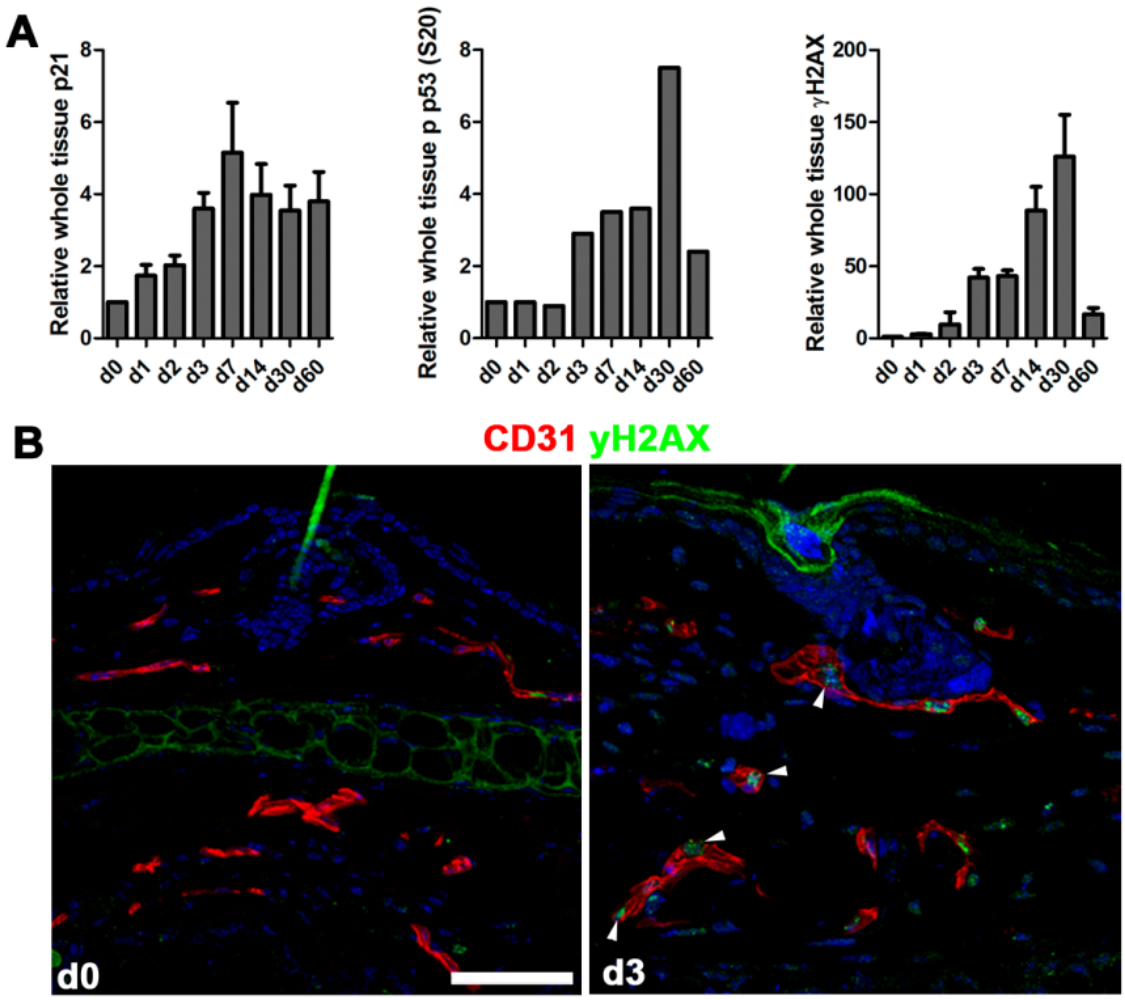

Fig. S6. Identification and quantification of endothelial cell replication stress in response to HIF-1 induction. (A) Quantification of immunoblots presented in Fig. 26. (B) Representative confocal fluorescent images of γH2AX localized to nuclear foci in d3 TetON-HIF-1 endothelial cells. TetON-HIF-1 data at each DOX day were compared with TetON-HIF-1 d0 data, using unpaired Student's t-test (***P<0.001, **p<0.01, * P<0.05). Bar: 50 µm.

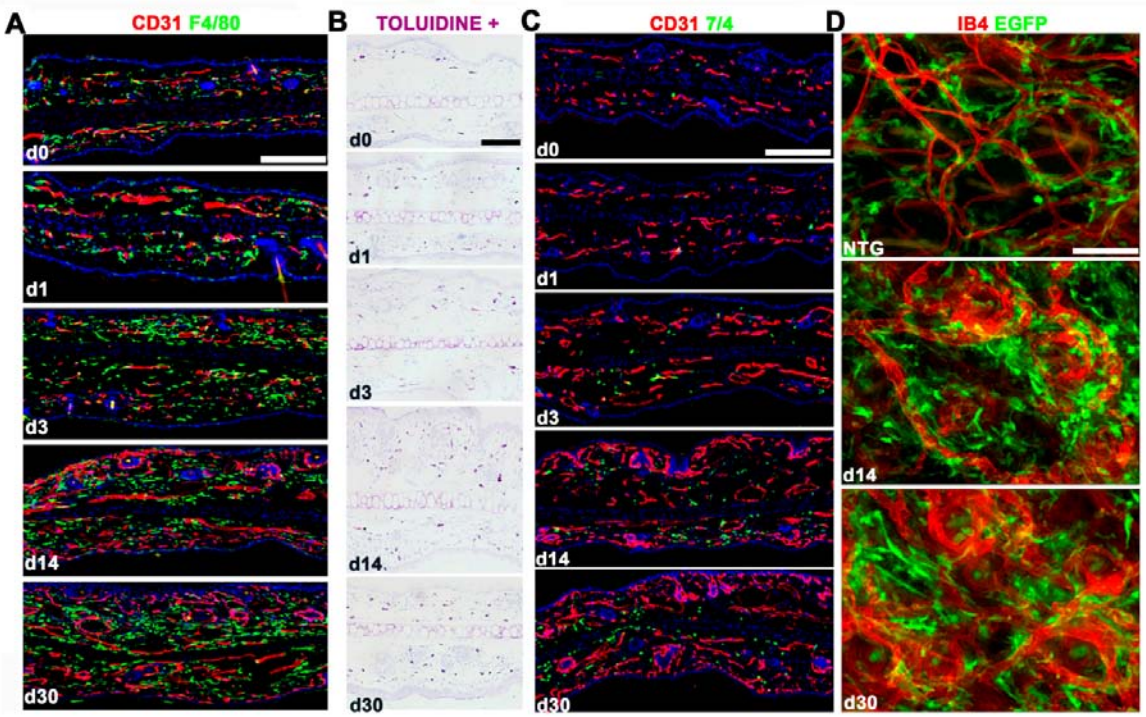

Fig. S7. DOX induction leads to stromal macrophage, mast cell, neutrophil, and bone marrow-derived cell recruitment. (A) Dual CD31/F4/80 immunofluorescence demonstrating d0–14 macrophage recruitment and d14-28 retention in TetON-HIF-1 transgenic mice. (B-C) Mast cells [toluidine blue (+)] are also recruited and retained from d0–30 (B), though to a lesser extent than 7/4(+) neutrophils (C). (D) Differential perivascular GFP(+) bone marrow derived cell recruitment and retention. *In-vivo* isolectin B4 (IB4) perfusion delineates the microvasculature. Bars: (A–C), 200 µm; (D), 100 µm.

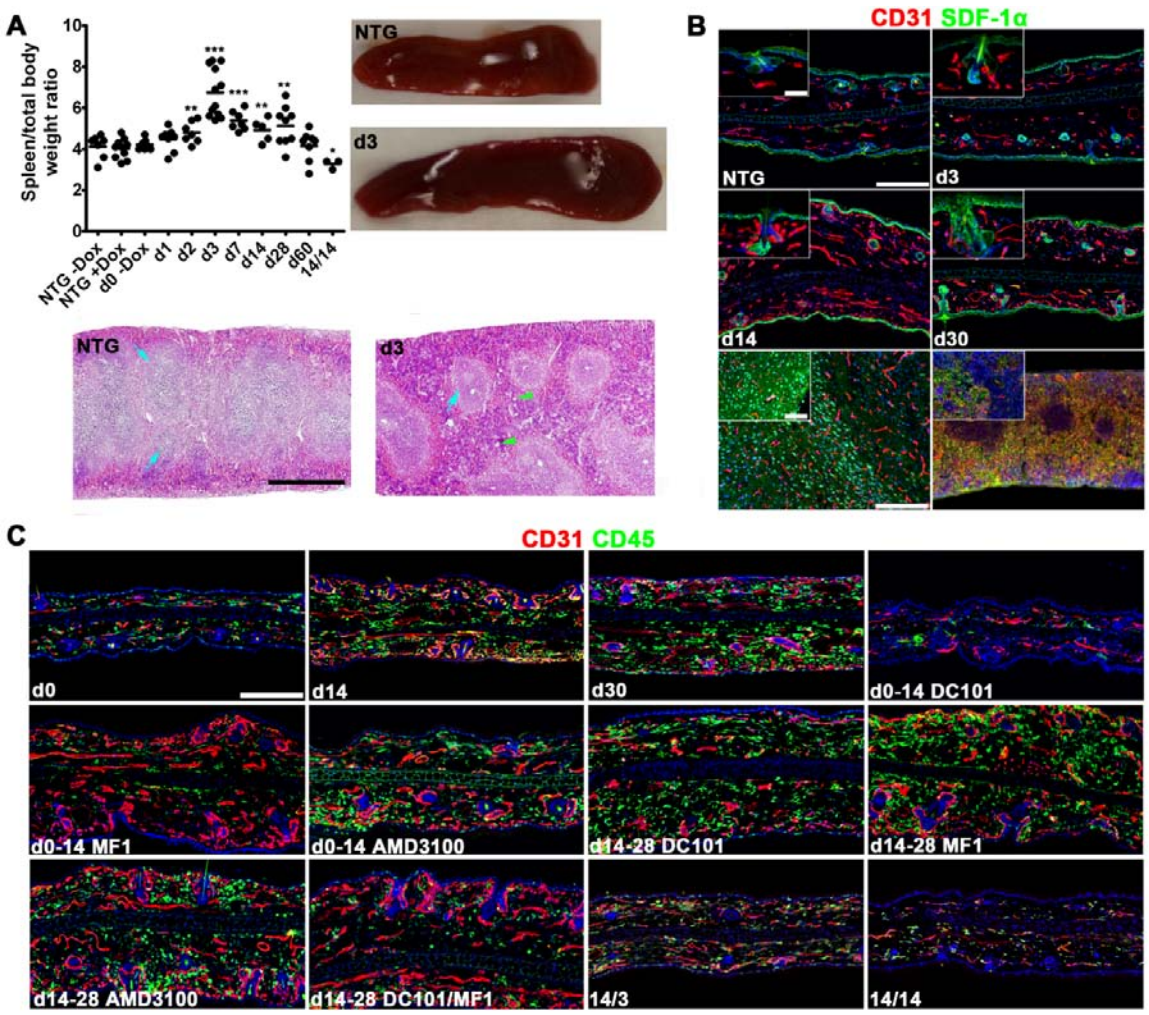

Fig. S8. DOX induction leads to splenomegaly, increased SDF-1α expression and stromal CD45+ myeloid cell recruitment. (A) Splenic weights in DOX-treated TetON-HIF-1 transgenic mice compared to treatment and time controls. Peak size is attained coincident with peak d3 endothelial cell proliferation (left panel). Representative spleens from either an NTG or a TetON-HIF-1 transgenic mouse both treated with DOX for 3d (right panel). Splenic histology from the corresponding DOX d3 NTG and TetON-HIF-1 mice (bottom right panel) showing cortical hyperplasia in the TetON-HIF-1 spleen (blue arrows, lymphoid follicles, green arrows, increased megakaryocytes). (B) Representative dual CD31/SDF-1 immunofluorescence of ear cross sections showing incremental SDF-1

expression from d3–14, plateauing at d30 in TetON-HIF-1 compared to NTG mice. Notably, SDF-1 upregulation is predominantly restricted to basal keratinocytes, with rare endothelial cell SDF-1 co-immunofluorescence (top four panels and insets). Robust SDF-1 expression in positive control tissues, brain (bottom left panel) and splenic cortex (bottom right panel). (C) Representative CD31/CD45 co-immunofluorescence demonstrating recruitment and stromal accumulation of CD45 myeloid cells during the TetON-HIF-1 DOX d0-14 neovascular development stage, with HIF-1-dependent retention of these cells from d14–28, similar to CD11b+ myeloid cell biology described in Figure 7A. Notably, myeloid cell retention is only slightly inhibited by AMD3100, Bars: (A-C), 200 µm. (B), 50 µm, upper four insets, 100 µm lower two insets.

2. VEGF is essential for HIF-mediated neovascularization*

To test the role of VEGF during epithelial HIF-1 induced neovascularization, we combined our previously described TetON-HIF-1 mice with K14-Cre transgenic and VEGF floxed knock-in mice.[93, 128-130] The final genotype of these composite mice is K14-rtTA:TRE:HIF-1α$^{P402A/P564A/N803A}$:K14-Cre:VEGF$^{f/f}$. The use of the HIF-1α triple mutant stabilized HIF-1 protein and rendered transcriptional activity insensitive to oxygen.[131] We designated this genotype as TetON-HIF1:VEGF$^{\Delta}$.

The segmentation capability of OR-PAM enabled determination of multiple parameters of vascular morphology including capillary volume as an indicator of angiogenesis, and arteriovenous (arteriolar/venular) volume, vessel length, diameter and tortuosity as measures of vascular remodeling. Serial PAM monitoring of individual mice from d0–60 of continuous DOX provision revealed that HIF-1 activation in TetON-HIF-1:VEGF$^{f/f}$ mice produced a marked 8-fold increase in capillary, a 3.5-fold elevation of arteriovenous and overall vascular volume (Fig. 30A and B). Three dimensional vessel segmentation analysis demonstrated abrogation of HIF-1-ediated vasodilatation and tortuosity induction in the absence of epithelial VEGF (Fig. 30B).

Topical phorbol ester induces angiogenesis via enhanced VEGF secretion from the activated epithelium.[132, 133] This is a transient phenomenon resolving within 3–4 days following single dose treatment. Previously, we discovered that germline transgenic mice constitutively expressing a stabilized HIF-1α mutant responded to single dose TPA challenge with a marked and prolonged stromal and intraepithelial neutrophil infiltrate

* Reprinted with permission from Sunday Oladipupo, Song Hu, Joanna Kovalski, Junjie Yao, Andrea C. Santeford, Rebecca E. Sohn, Konstantin Maslov, Lihong V. Wang, and Jeffrey M. Arbeit, "VEGF is essential for hypoxia-inducible factor mediated neovascularization but dispensible for endothelial sprouting," (Submitted).

persisting for three weeks.[134] Neutrophil recruitment was secondary to HIF-1 enhanced NfkB signaling and downstream chemokine production by transgenic keratinocytes. We capitalized on this strategy to determine if lack of HIF-1 mediated neovascularization in TetON-HIF1:VEGF$^{\Delta}$ vasculature could be rescued. TetON-HIF1:VEGF$^{\Delta}$ and TetON-HIF-1:VEGF$^{f/f}$ were DOX-induced for 14 days to prime the keratinocytes and stroma, and emulate germline constitutive activation. A single dose of topical TPA was followed by harvest of the ears 10 days later for immunofluorescence analysis. TPA treatment did not further augment VEGF expression or neovascularization in TetON-HIF-1:VEGF$^{f/f}$ mice (Fig. 31A–C). In contrast, single dose TPA in TetON-HIF1:VEGF$^{\Delta}$ mice produced a 2-fold increase in VEGF associated with a similar fold increase in neovessels. This partial rescue of HIF-1 mediated neovascularization in the absence of epithelial VEGF was associated with a marked influx of stromal neutrophils to levels similar to that of TPA-treated TetON-HIF-1:VEGF$^{f/f}$ mice. Restoration of the HIF-1 neovascular phenotype by chemokine-activated neutrophils was also associated an increase in capillary and total vessel volume, and in vessel tortuosity, as determined by OR-PAM (Fig. 31A and B).

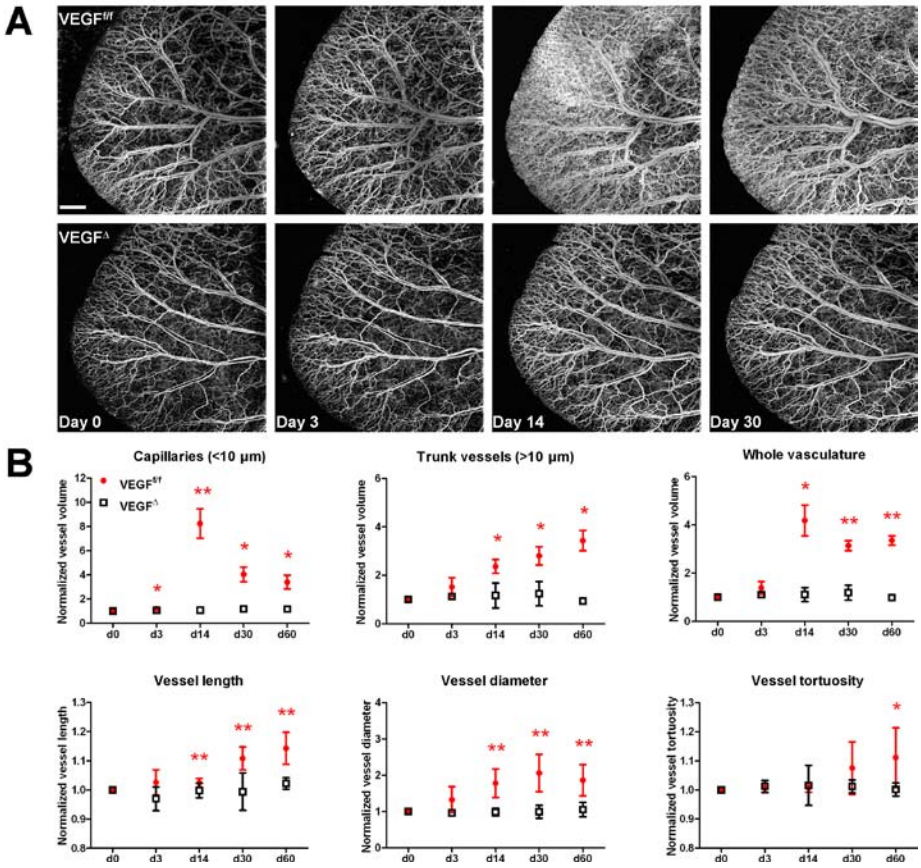

Fig. 30. TetON-HIF1:VEGF$^{\Delta}$ mice lacked vessel remodeling. (A) Angiogenesis determination and accompanying vascular remodeling by OR-PAM. OR-PAM was performed in the same VEGF$^{f/f}$ or VEGF$^{\Delta}$ transgenic mouse serially imaged for 60 days (d0–30 are represented). Increased capillary density (asterisk) is evident particularly by d14, whereas arteriovenous remodeling is detectable at d14 and prominent by d30 (arrow). (B) Quantification of (A) showing microvascular multi-parameter measurements from d0-60 (n=3 mice per time point, see Methods for more details). VEGF$^{f/f}$ or VEGF$^{\Delta}$ data at each DOX day were compared with VEGF$^{f/f}$ d0 data using the unpaired Student's t-test (*P<0.05, **P<0.01 and ***P<0.001). Scale bar: 500 μm.

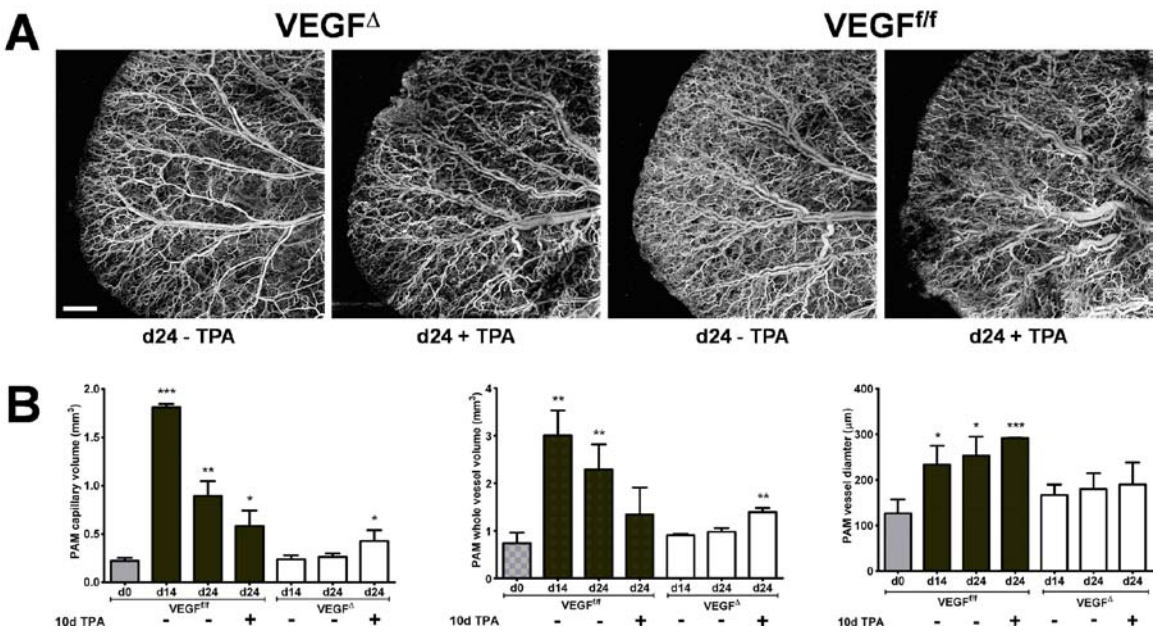

Fig. 31. Topical TPA rescues HIF-1 neovascularization in VEGF$^{\Delta}$ mice. (A) Angiogenesis determination and accompanying vascular remodeling in TPA-treated and non-treated VEGF$^{f/f}$ and VEGF$^{\Delta}$ mice by OR-PAM. TPA partially rescued both capillary volume and arteriovenous remodeling. (B) Quantification for vascular parameters in (A). (n=3 mice). *P<0.05, **P<0.01 and ***P<0.001. Scale bar: 500 μm.

3. Longitudinal OR-PAM of tumor neovascularization*

As a preliminary study, OR-PAM imaged the microvasculature and the vessel-by-vessel sO_2 of an A549 lung adenocarcinoma xenograft in a nude mouse ear (Fig. 32A–C). It is notable that the vessel sO_2 map of this tumor xenograft histotype is similar to those of other xenograft models, a central hypoxic/anoxic core and an adequately oxygenated peripheral rim.

Future study will focus on longitudinal determination of morphological (i.e., vessel diameter, length, tortuosity and volume) and functional (i.e., HbT, sO_2, and blood flow) changes within individual microvessels during the entire process of tumor growth within the same animal will provide the unprecedented ability to test hypotheses directed at how the functional properties of the tumor neovasculature affect specific features of tumor cell and tissue biology.

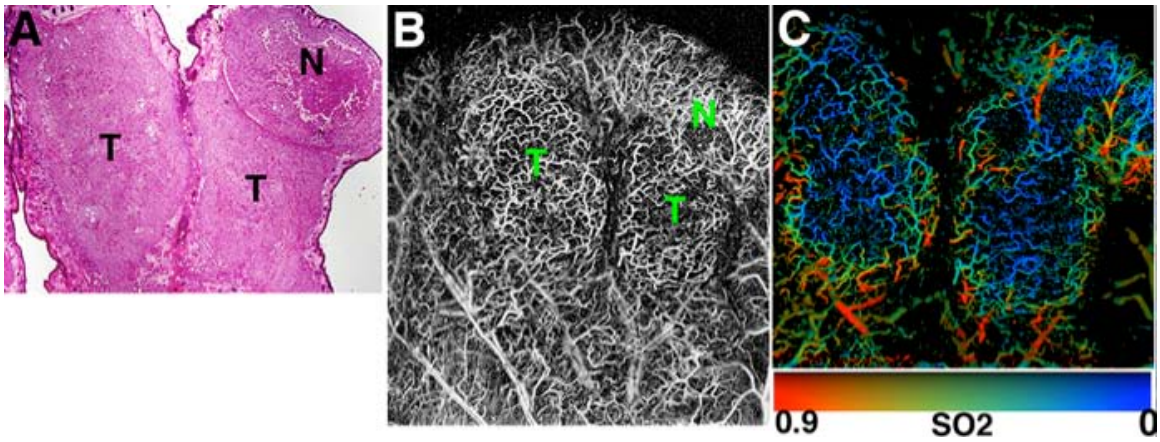

Fig. 32. (A) Coincident *en face* paraffin histopathology of an A549 lung adenocarcinoma tumor, (B) PAM imaged neovascular architecture and (C) vessel-by-vessel sO_2. T: tumor; N: necrosis. Color bar in (C) indicates sO_2 concentration.

* S. Hu et. al., Preliminary data.

IV. OR-PAM IN NEUROLOGY

1. Intravital microscopy of amyloid plaques in a transgenic mouse model*

1.1 Introduction

Amyloid-β, the primary constituent of senile plaques, is hypothesized to play a major role in the pathogenesis of AD, but the underlying mechanisms are still elusive. Recent advances in established clinical imaging modalities have permitted noninvasive imaging of amyloid deposits in patients.[135] However, the neuropathologic changes in AD are microscopic, and subtle changes due to disease progression or treatment may be undetectable by such clinical instruments because of their low spatial resolutions. Multiphoton microscopy, a commercially available laser scanning microscopy technique, allows imaging of amyloid plaques with high sensitivity and sub-micrometer resolution in animal models.[136] However, its applications are limited by the inability to image through the intact skull, thereby requiring cranial window preparations.

Here, we report the first application of OR-PAM towards imaging amyloid plaques in an AD transgenic mouse model. OR-PAM images of Congo-red-stained brain sections from these mice were virtually identical to fluorescence images. Moreover, *in vivo* OR-PAM images through a cranial window also showed high correlation with observations by multiphoton microscopy. As a new technology for *in vivo* amyloid plaque imaging, OR-PAM provides both the exogenous molecular contrast from the amyloid-specific Congo red dye and the endogenous absorption contrast from

* Reprinted with permission from S. Hu†, P. Yan†, K. Maslov, J.-M. Lee, and L. V. Wang, "Intravital imaging of amyloid plaques in a transgenic mouse model using optical-resolution photoacoustic microscopy," Opt. Lett. 34 (24), 3899–3901 (2009). † Authors contributed equally to this work.

hemoglobin, enabling simultaneous visualization of cerebral microvasculature without using angiographic dye.

1.2 Methods

Figure 33 shows a schematic of the OR-PAM system for intravital amyloid plaque imaging. To maximize the imaging sensitivity, optical illumination and ultrasonic detection in our OR-PAM system are configured confocally by an acoustic-optical beam splitter.[137] The beam splitter is nearly transparent to the optical illumination, but the oil-glass surface at the diagonal reflects almost all the ultrasonic signals to a 75 MHz ultrasonic transducer [V2022 (BC), Olympus NDT] attached to the vertical side of the bottom prism. The near-diffraction-limited optical focusing achieved by a commercial microscope objective (RMS4X, Thorlabs) determines the 5-μm lateral resolution of OR-PAM. An acoustic lens (NA: 0.46) is attached to the bottom of the beam splitter and immersed in a water tank to collect photoacoustic signals. A window is opened in the bottom of the water tank and sealed with an ultrasonically and optically transparent polyethylene membrane to expose the imaging site. For simplification, the water tank is not shown in Fig. 33. Two-dimensional mechanical scanning of the animal along the transverse plane, in combination with time-resolved ultrasonic detection, provides volumetric resolution. Hence, no depth scanning is necessary.

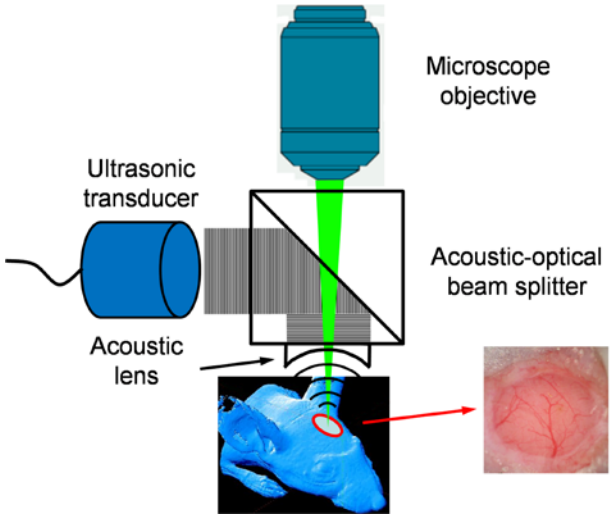

Fig. 33. Schematic of OR-PAM for amyloid plaque imaging. OR-PAM imaging and multiphoton imaging were performed through a cranial window preparation (inset).

1.3 Results and Discussion

In order to compare and validate OR-PAM with established fluorescence microscopy for imaging of amyloid plaques, a Congo-red-stained brain section from a 10 month-old APP/PS1 mouse (The Jackson Laboratory) was cover-slipped and examined using a fluorescence microscope (BX50, Olympus) equipped with a MicroFire® monochrome microscope digital CCD camera (Optronics) under Rhodamine excitation (496–540 nm). By measuring red fluorescence (520–625 nm), amyloid plaques were detected in APP/PS1 brain sections (Fig. 34A). A 1 × 1 mm ROI (enclosed by the red dashed box in Fig. 34A, and replotted in Fig. 34B for better comparison) was imaged by OR-PAM using a 523 nm wavelength (Fig. 34C). All amyloid plaques visualized using conventional fluorescence microscopy were observed with OR-PAM as well, suggesting that OR-PAM has the sensitivity and spatial resolution required to image amyloid plaques (a few representative plaques are paired up in Figs. 34B and 34C for comparison). The

main features of amyloid plaques in the two images were virtually identical (the correlation coefficient was calculated to be 0.95 based on both plaque size and location).

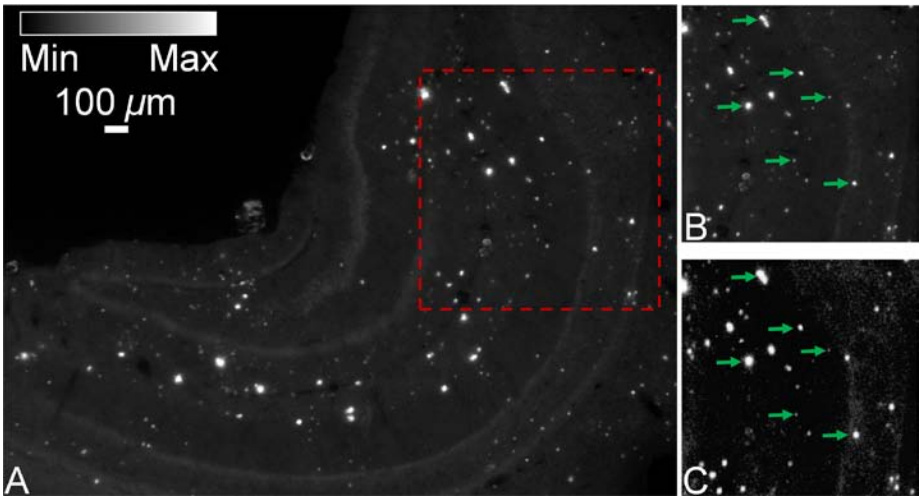

Fig. 34. *In vitro* imaging of a Congo-red-stained brain section from a 10-month-old APP/PS1 mouse. (A) The entire hippocampus imaged using conventional fluorescence microscopy. (B) A region of interest selected from (A) (boxed area). (C) The same region of interest imaged by OR-PAM for comparison. Arrows: plaques. Scale bar in (A) applies for (A–C).

To examine the plaque imaging capability of OR-PAM in living mice, OR-PAM images were directly compared with the images acquired by multiphoton microscopy. A 10-month-old APP/PS1 mouse was injected with Congo red through the cisterna magna to label amyloid plaques *in vivo*. Twenty-four hours after injection, an open-skull cranial window covered by a plastic coverslip was created over the parietal cortex, and dye labeling was confirmed by conventional fluorescence imaging (Fig. 35A). An ROI (enclosed by the red dashed box in Fig. 35A) containing a variety of amyloid plaques and blood vessels was selected for both dual-wavelength OR-PAM imaging and multiphoton

imaging (LSM 510 META NLO system, Zeiss). Two-photon fluorescence was generated with 800 nm excitation (Chameleon Ti: Sapphire laser, Coherent) and detected in the spectral range of 565–615 nm. A maximum-intensity-projection image (Fig. 35B) was generated by a *z*-stack image series acquired from the cranial window surface to a depth of ~200 μm into the cortex. The incremental *z*-step distance was 10 μm under a 10x water-immersion objective (NA: 0.33, Zeiss). For the dual-wavelength OR-PAM imaging, optical wavelengths of 570 nm (Fig. 35C) and 523 nm (Fig. 35D) were selected to differentiate the photoacoustic signals generated by hemoglobin and Congo-red-labeled amyloid plaques. Imaging depths of amyloid plaques and blood vessels were quantified to be 230 μm and 450 μm from the cortical surface, respectively. The absorption of Congo red at 523 nm is ~6 times higher than that at 570 nm;[138] however, the absorption of hemoglobin differs by only 1.4 times.[139] Moreover, at each wavelength, the optical absorption coefficients of HbO_2 and HbR are nearly equal, so the blood photoacoustic signals reflect the total hemoglobin concentration regardless of the blood oxygenation level. Based on these two characteristics, the photoacoustic image taken at 523 nm was linearly scaled to equalize the blood vessel signals with their counterparts taken at 570 nm, and then the two mutually normalized images were subtracted pixelwise to eliminate the blood signals and isolate the Congo-red-labeled amyloid plaques. Upon separating the distributions of the hemoglobin and the amyloid plaques, they were pseudocolored differently for clear visualization in both the MAP image (Fig. 35E) and the 3-D movie (data not shown). Images acquired using OR-PAM and multiphoton microscopy were directly compared, revealing excellent correlation in plaque distribution (arrows, Fig. 35B, D and E). A few small plaques visualized using multiphoton microscopy (Fig. 35B)

were not detected by the OR-PAM system (Fig. 35E), most likely due to the limited signal-to-noise ratio caused by the non-optimized excitation wavelength for Congo red detection and by the interference from the strong blood absorption. It should be noted that the imaged plaque sizes are slightly different as measured by the two imaging modalities. This likely reflects differences in imaging contrast and sensitivity between the two techniques; however, since each plaque can serve as its own control for time-lapsed imaging, measures of relative plaque growth are expected to be similar.

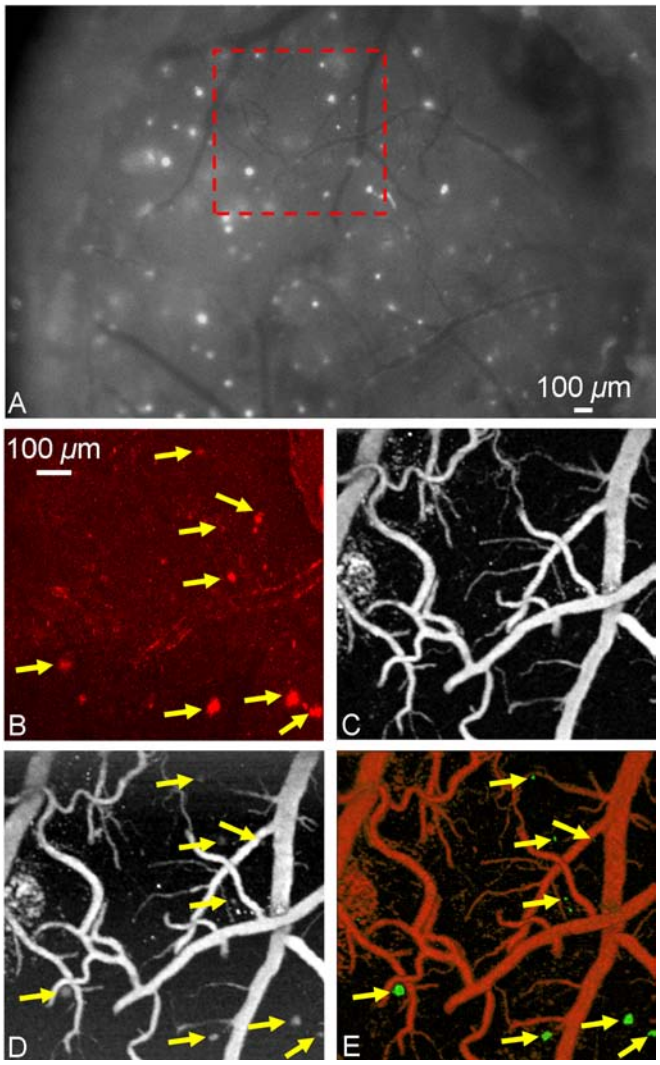

Fig. 35. *In vivo* brain imaging of a Congo-red-injected 10-month-old APP/PS1 mouse through a cranial window. (A) The exposed cortical brain region imaged using

conventional fluorescence microscopy through the cranial window. The region of interest marked by a red dashed box was imaged by (B) multiphoton microscopy, and OR-PAM at (C) 570 nm and (D) 523 nm, respectively. (E) The processed dual-contrast optical-resolution photoacoustic microscopic image, where amyloid plaques are colored green and blood vessels are colored red (volumetric visualization is available online as Media 1). Arrows: plaques. Scale bar in (B) applies for (B–E).

Although the current configuration of OR-PAM has successfully demonstrated the ability to image amyloid plaques *in vivo*, transcranial imaging (through an intact skull) is certainly more attractive for minimally-invasively monitoring AD progression and drug efficacy. OR-PAM has already been shown to be capable of imaging individual capillaries through intact skulls in living adult mice.[5] Thus, *in vivo* transcranial OR-PAM imaging of amyloid plaques, which are similar to or larger than capillaries, is highly likely with further optimization of imaging parameters and improvements in the optical absorption of amyloid-specific dyes as indicated below.

One possible improvement would take advantage of the fact that the absorption spectrum of Congo red peaks at 500–510 nm, where hemoglobin experiences a local absorption valley.[138, 139] Down-shifting the optical illumination wavelength of OR-PAM to 500–510 nm (not available in our current laser system) will increase the contrast between hemoglobin and Congo red by at least a factor of 4, which will help differentiate between amyloid plaques and blood vessels. Another possible improvement is to modify the current acoustic detection mechanism to avoid the unnecessary transformation of the photoacoustic signals from p- to sv-waves, and to apply an ultrasonic antireflection

coating to the acoustic lens. Still another improvement is suggested by the Fourier analysis of our transcranial mouse brain imaging data, which shows that decreasing the center frequency of the ultrasonic transducer from current 75 MHz to 40 MHz is expected to further increase the detected photoacoustic signals by 2 fold at the expense of spatial resolution.

Besides technical improvements to the OR-PAM system, developing amyloid-specific dyes absorbing at the NIR optical window of biological tissues (700–800 nm) would be expected to further enhance *in vivo* amyloid plaque imaging.[140] Tissue scattering and absorption within the NIR range are greatly reduced compared to that in the visible spectrum. Working in the NIR region with the aid of highly specific amyloid dyes will allow deeper tissue penetration and provide higher contrast between the targeted amyloid plaques and the surrounding tissues.

1.4 Conclusion

Advances in the above aspects will likely allow OR-PAM imaging of amyloid plaques through an intact mouse skull. This noninvasive imaging capability will eliminate the influence of the cranial window preparations on the underlying brain tissues. Recent studies suggest that invasive cranial window preparations may adversely influence underlying brain tissue behavior.[81, 141] Furthermore, imaging through intact skull would greatly expand the available regions for imaging, thereby reducing the numbers of animals needed to quantify plaque growth. Such a model would be very attractive as an *in vivo* screen for drug development.

2. Intravital microscopy of microvascular responses to cortical electrical stimulation*

2.1 Introduction

Neurovascular coupling links local neural activities with spatial-temporal changes in cerebral hemodynamics—including HbT, sO_2, and blood flow.[142, 143] This feature has been widely utilized by functional brain imaging techniques—such as MRI, DOT, and PAT—as a minimally invasive or non-invasive method to infer brain function.[60, 144-146]

However, exploring the mechanism of neurovascular coupling at the microscopic level remains challenging. Clinical neuroimaging modalities (such as MRI and DOT) lack the spatial resolution for microvascular imaging,[9] and high-resolution purely optical microscopy techniques (such as fluorescence microscopy and OCT) have limited access to hemodynamic parameters, especially sO_2.[1] PAT has the potential to overcome these limitations by enabling label-free quantification of cerebral hemodynamic changes in HbT, sO_2, and blood flow velocity at various spatial scales.[147] As a first-in-kind neurovascular study using photoacoustics, Wang et al. used PACT to observe the hemodynamic response of somatosensory cortex to mechanical stimulation of the rat whisker pad.[146] Providing a spatial resolution comparable to clinical modalities (200 μm), the early-version PACT was not able to image the microvasculature itself. Later with AR-PAM, Stein et al. demonstrated hemodynamic monitoring of individual vessels under hypoxic and hyperoxic challenges.[148] Although having a much refined resolution (70 μm laterally), AR-PAM still has difficulty in resolving distal microvessels and single

* Reprinted with permission from Vassiliy Tsytsarev†, Song Hu†, Junjie Yao, Konstantin Maslov, Dennis L. Barbour, and Lihong V. Wang, "Photoacoustic microscopy of microvascular responses to cortical electrical stimulation," J. Biomed. Opt. (Under review). † Authors contributed equally to this work.

capillaries, which are assumed to have the closest spatial correlation with neural activities.[64] Recently, Maslov et al. developed OR-PAM.[4] With diffraction-limited optical focusing, OR-PAM enables transcranial imaging of murine cerebral microvascular morphology and oxygenation at the resolution of individual capillaries.[5] Quantitative monitoring of microhemodynamics, such as vasodilatation, vasomotion, and changes in blood flow, has also been documented with this technique.[7, 12]

In this work, OR-PAM was used for the first time to explore neurovascular coupling at the microscopic level in a cortical electrical stimulation model. Direct electrical stimulation may cause cortical neurons to generate action potentials and synaptic release of various neurotransmitters, which can further react with nearby astrocytes, smooth muscle cells, and endothelial cells of the vessel wall.[142] The net effect of these reactions drives cortical vessels from the resting state to either vasoconstriction or vasodilatation. Alternatively, smooth muscle cells and astrocytes can directly respond to electrical stimulation:[149] direct electrical stimulation of smooth muscle cells may cause vasoconstriction, while direct electrical stimulation of astrocytes may result in intracellular calcium waves along the astrocytic syncytium, which may signal the release of various neuromodulators to direct blood vessels to regulate the metabolic supply by increasing or decreasing the local vessel capacity.[150, 151] Moreover, electrical stimulation of brain tissue temporarily increases extracellular potassium concentration, which can potentially cause neural hyperactivity. Increased neural activity requires more blood flow, which may result in vasodilatation.[142, 149, 151] Using OR-PAM, we observed both vasodilatation and vasoconstriction in response to cortical electrical stimulation. We further studied the electrical current dependence and the spatial-temporal characteristics

of these two types of microvascular responses, at both single-vessel and statistical (27 vessels in total) levels. The results indicate that OR-PAM provides sufficient spatial resolution and adequate temporal resolution to study the coupling between neural activities and individual cortical microvessels.

2.2 Methods

Experiments were performed on three animals using our reflection-mode OR-PAM system (Fig. 36a), which has been described in detail previously.[4, 5] Before each experiment, a Swiss Webster mouse (Hsd: ND4, 25–30 g; Harlan, Indianapolis, IN) was anesthetized by intraperitoneally administering a dose of 87 mg/kg ketamine and 13 mg/kg xylazine. The animal was placed into a custom-made stereotaxic imaging stage, and the left dorsal portion of the skull was exposed by removing the scalp and temporal muscle. A cranial opening (~4×4 mm^2) was made using a dental drill, and the exposed dura mater surface was cleaned with artificial cerebrospinal fluid. A monopolar tungsten electrode (impedance: 1 MΩ; tip diameter: 10 μm; MicroProbes for Life Science, Gaithersburg, MD) was introduced into the cortex to a depth of 0.1–0.2 mm through the opening to induce the preset electrical stimulation (Fig. 36b, c). Then, optically transparent ultrasonic gel was applied to the cranial opening for ultrasound coupling. Anesthesia was maintained using vaporized 1.0% isoflurane with an air flow rate of 1.0 L/min. The body temperature of the animal was kept at 37°C by a temperature-controlled heating pad.

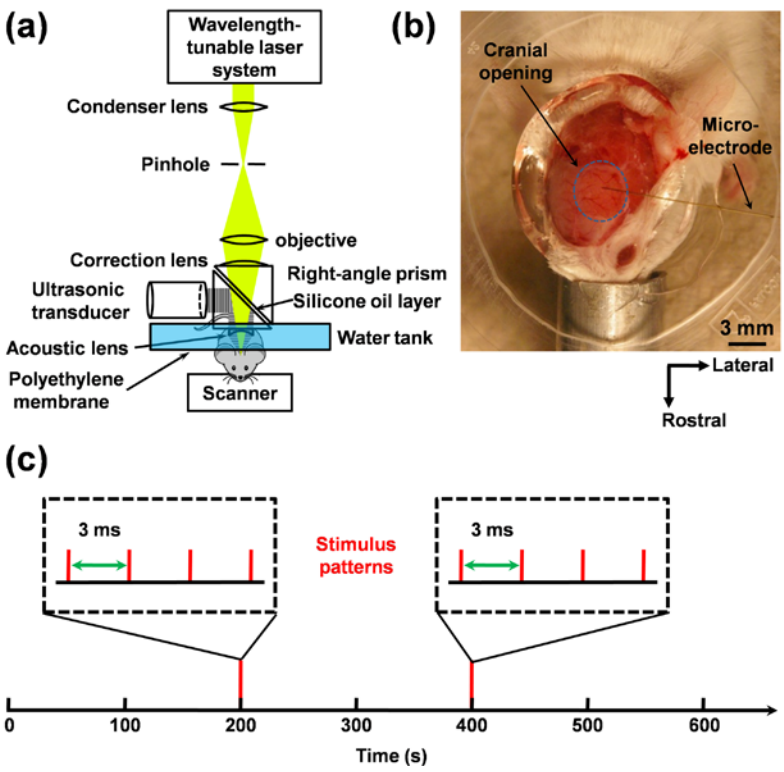

Fig. 36. (a) Schematic of the optical-resolution photoacoustic microscope. (b) Photograph of the exposed mouse brain surface with an introduced microelectrode. (c) Stimulation pattern.

During each experiment, we first used an isosbestic wavelength of 570 nm to image the vascular system structure in a 2×2 mm^2 cortical region through the cranial opening (Fig. 37, gray scale). Then, within a smaller ROI around the tip of the microelectrode, wavelengths of 570 nm and 578 nm were used to quantify sO_2.[152] The overlaid structural and sO_2 (functional) images are shown in Fig. 37. Upon observing the vascular system structure and sO_2 distribution, we randomly selected a B-scan crossing both arterioles and venules (indicated by the dashed line in Fig. 37) for hemodynamic monitoring with various stimulation intensities. Each monitoring trial lasted for 600 s

(300 B-scans at 570 nm), during which two identical electrical stimulation sequences were executed 200 s and 400 s after the first B-scan, respectively (Fig. 36c). Each stimulus consisted of a train of four identical square pulses (pulse duration: 0.3 ms; repetition rate: 300 Hz; current intensity: 100–400 μA) generated by a stimulator (A365; World Precision Instruments, Sarasota, FL) triggered by a function generator (DS345; Stanford Research Systems, Sunnyvale, CA). The time interval between two adjacent trials was 10 minutes.

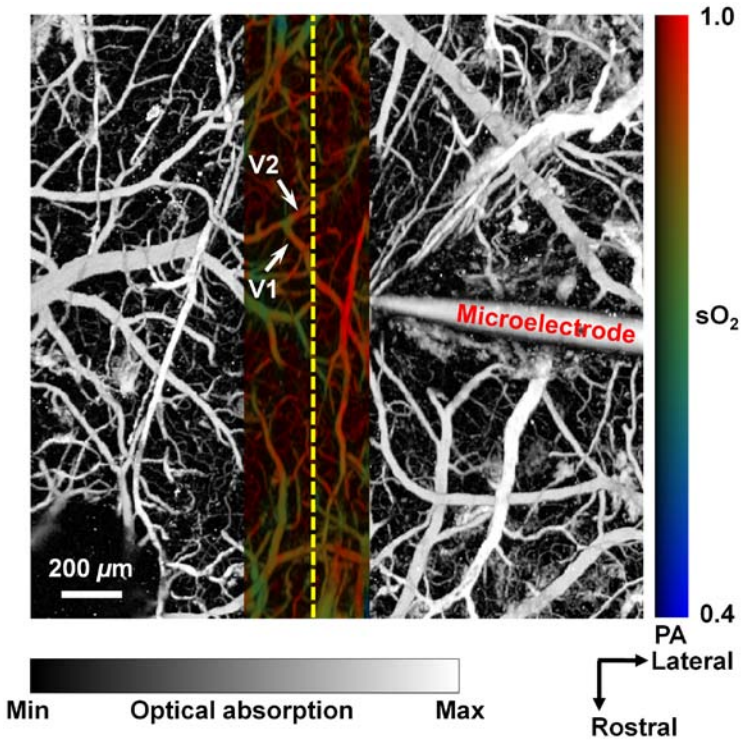

Fig. 37. Superimposed open-skull photoacoustic images of the mouse cortical microvasculature. The maximum-amplitude projection image acquired at 570 nm is shown in gray scale, and the vessel-by-vessel hemoglobin oxygen saturation mapping of a smaller region calculated from dual-wavelength measurements is shown in color scale. B-scan monitoring of the vascular response was performed along the yellow dashed line. V1 and V2 are the two microvessels studied in Fig. 38.

After image acquisition, photoacoustic amplitudes were extracted via the Hilbert transformation using the "hilbert" function in MATLAB (MathWorks, Natick, MA, USA). To distinguish vessels from background, we empirically set the amplitude threshold to be 3 dB above the noise level, which was defined as the standard deviation of the background noise amplitude. After converting the photoacoustic image into a binary image using the amplitude threshold, the cross section of each vessel was identified (i.e., segmentation) by 8-connected labeling using the Image Processing Toolbox in MATLAB. Because the transverse resolution of OR-PAM (5 μm) is much finer than the axial resolution (15 μm) and thus provides more accurate measurements, the vessel diameter was calculated along the transverse direction. The initial condition (baseline) was defined as the mean value of the vessel diameter before the first stimulation. To compensate for the slow baseline drift and the oblique angle subtended by the B-scan direction and the vessel axis, the time course of the vessel diameter was normalized to its baseline at each trial. Changes in vessel diameter were also normalized to the baseline. The duration of vasodilatation was defined as the period during which the vessel remained a response (in diameter) that is above 90% of the maximum response. The response time was defined as the period during which the vessel response changed monotonically from 10% to 90% of the maximum response; similarly, the recovery time was defined as the period during which the vessel response changed monotonically from 90% to 10% of the maximum response.

After each experiment, the animal was euthanized with an overdose of pentobarbital. All experimental animal procedures were carried out in conformance with the laboratory animal protocol approved by the School of Medicine Animal Studies

Committee of Washington University in St. Louis.

2.3 Results and Discussion

OR-PAM provides high spatial resolution, adequate temporal resolution, and a large FOV,[5, 7] allowing us to study the responses of individual vessels at different spatial locations simultaneously. The present study investigated a total of 30 microvessels within 1 mm of the stimulating electrode from 3 different animals. In response to intracortical electrical stimulation, 9 vessels showed only vasoconstriction, 15 showed only vasodilatation, 3 showed both, and the remaining 3 showed no response.

Figure 38 demonstrates the vasoconstriction and vasodilatation of the same microvessel (V1 in Fig. 37) in response to electrical stimulations at different current levels. At 100 μA, a distinct vasoconstriction appeared after each of the two stimuli [Fig. 38a). At 150 μA, the first stimulus produced a pronounced and prolonged vasodilatation, which prevented the vessel from recovering back to the resting state before the arrival of the second stimulus (Fig. 38b). Changes in vessel diameter were not clearly observed in the axial direction because the axial resolution (15 μm) of OR-PAM was not adequate to resolve such small changes. Note that the baseline diameters of the microvessel (defined as the average transverse dimension of the vessel prior to the first stimulation in each monitoring trial) were different between the two trials (the left panels in Fig. 38a, b), possibly due to the isoflurane anesthesia and the open-skull condition.[153] Also note that the vessel cross sections in Fig. 38 appeared elliptic because the B-scan crossed the vessel at an oblique angle rather than a right angle. However, by normalization on initial condition, the influence of these two effects on the quantification of relative changes in

vessel diameter can be eliminated.

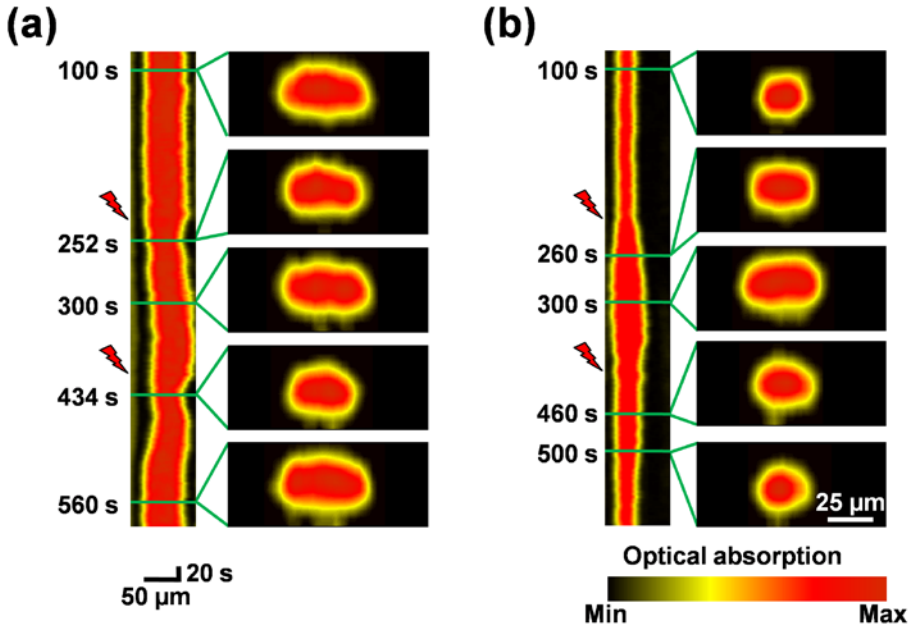

Fig. 38. B-scan monitoring of vasoconstriction and vasodilatation induced by direct electrical stimulations at (a) 100 µA and (b) 150 µA (B-scan rate is 0.5 Hz). In each panel, the left column is the time course of the change in vessel diameter (represented by the projection of the vessel cross section). The right column is the vessel cross-sectional image at different time points, indicated by the green lines. The red lightning symbol indicates the onset of the stimulation.

Figure 39a further shows the current-dependent response of microvessel V1. At 100 µA (purple curve in Fig. 39a), a rapid vasoconstriction was induced right after each stimulus, with as much as an 18% decrease in vessel diameter; however, higher stimulation currents (from 110 µA up to 400 µA) led to a transition from rapid vasoconstriction to prolonged vasodilatation, with a diameter increase of as high as 87%. The normalized maximum diameter changes of V1 at a variety of stimulation currents

were plotted in Fig. 39b (red squares) and fitted with the smoothing spline function (red curve) in MATLAB. According to the fitting curve, the critical stimulation intensity corresponding to the transition from vasoconstriction to vasodilatation was estimated to be ~107 μA. Besides the transition in vascular response, the amplitude and the duration of vasodilatation of V1 were found to be non-monotonic with the current intensity [red curves in Fig. 39b, c). This non-monotonic response likely suggests both coexistence and competition between the two vascular regulation mechanisms: current-induced smooth muscle contraction and neuroactivity-induced vasodilatation. Interestingly, the other daughter vessel (V2 in Fig. 37), which bifurcated from the same parent vessel as V1, showed very similar responses (blue curves in Fig. 39b, c). The Pearson correlation coefficients of the current-dependent vasodilatation amplitude and duration were calculated to be 0.89 (p = 0.001) and 0.73 (p = 0.06), respectively, using a standard function called “corrcoef” in MATLAB.

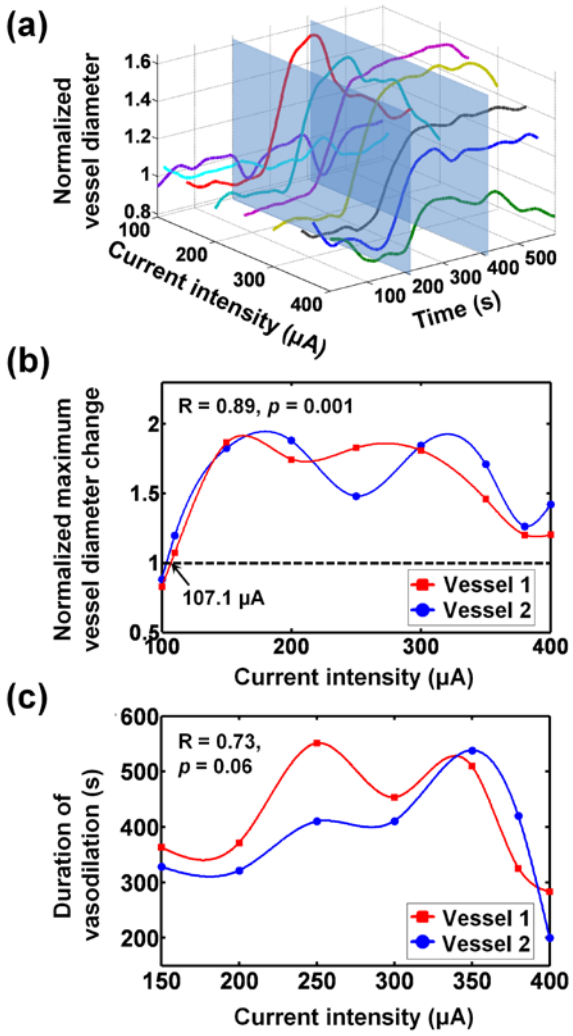

Fig. 39. Current-dependent vascular response studied in individual microvessels. (a) Time courses of the diameter change in V1 under various stimulation intensities. (b and c) Correlation of the current-dependent vascular responses of two daughter vessels (V1 and V2) bifurcated from the same parent vessel: (b) normalized maximum diameter change and (c) the duration of vasodilatation. The two semi-transparent planes in panel (a) indicate the time points of the two stimuli.

OR-PAM's large FOV enabled exploration of the spatial features of the microvascular response. All 27 microvessels that showed responses in the 3 experiments

were studied in this way (Fig. 40 and Table 4). When microvessels were within 300 μm of the electrode tip, there was a clear transition from vasoconstriction to vasodilatation with increased stimulation intensity (blue bars in Fig. 40a and Table 4a). Throughout this transition, both the response amplitude and the number of responding vessels were diminished, suggesting a transition in the balance between current-induced smooth muscle contraction and neuroactivity-induced vasodilatation (blue bars in Fig. 40a, b). However, in vessels that were farther from the electrode tip (>300 μm), vasodilatation became more dominant. Another observation was that the total number of responsive vessels decreased with increased distance from the electrode tip, which likely reflected the decay of stimulation intensity due to the radial current diffusion (Fig. 40b and Table 4b).

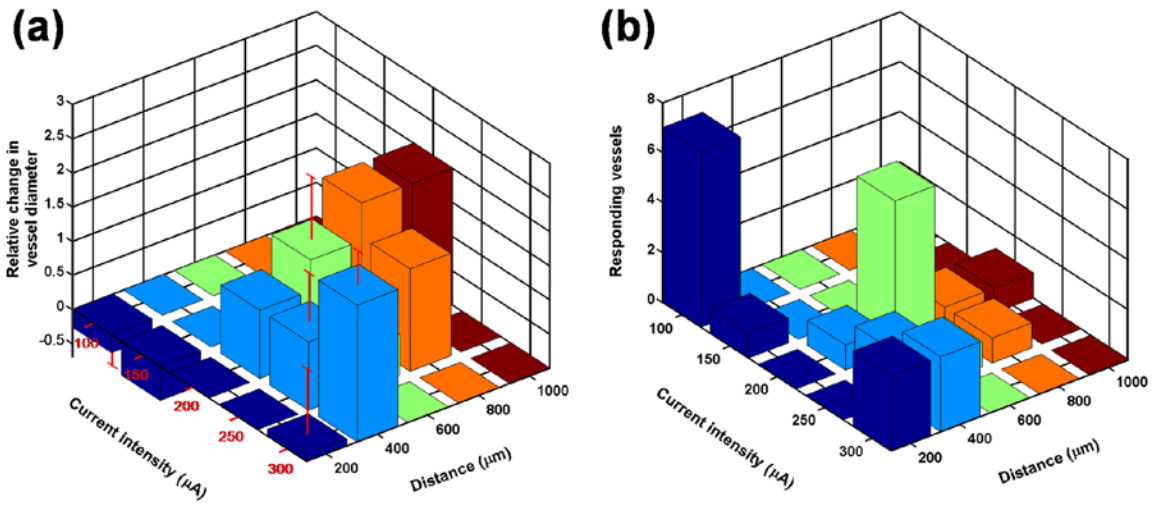

Fig. 40. Spatial characteristics of vasoconstriction and vasodilatation at different stimulation currents studied in 27 microvessels. (a) Relative change in vessel diameter vs. distance from the electrode tip. (b) Number of responding vessels vs. distance from the electrode tip. For clarification, the relative diameter changes and the numbers of responding vessels are listed in Table 4a and 4b, respectively.

Table 4. Spatial characteristics of vasoconstriction and vasodilatation at different stimulation currents studied in 27 microvessels.

(a) Relative change in vessel diameter vs. distance from the electrode tip. Values are in mean ± standard deviation format.

Current (μA) \ Distance (μm)	200	400	600	800	1000
100	-0.26±0.48	0	0	0	0
150	-0.50	0	0	0	0
200	0	1.00	1.45±0.92	2.00	2.00
250	0	1.00±0.71	0.60	1.50	0
300	0.10±0.95	2.00±0.50	0	0	0

(b) Number of responding vessels vs. distance from the electrode tip.

Current (μA) \ Distance (μm)	200	400	600	800	1000
100	7	0	0	0	0
150	1	0	0	0	0
200	0	1	6	1	1
250	0	2	1	1	0
300	3	3	0	0	0

The temporal features of vasodilatation and vasoconstriction were further studied statistically, as shown in Fig. 41 (9 vessels for vasoconstriction and 15 vessels for vasodilatation). For each vessel, vasoconstriction or vasodilatation occurring at the lowest stimulation current was chosen for study. The unpaired 1-tailed Wilcoxon Signed Rank Test showed that the response and recovery times of vasodilatation were significantly longer than those of vasoconstriction. Interestingly, although both the response phase of

vasodilation and the recovery phase of vasoconstriction represent the increase in vessel diameter, their time scales are quite different (the same situation for the recovery phase of vasodilation and the response phase of vasoconstriction). This likely suggests the different underlying mechanisms of the two types of vascular response: vasoconstriction, caused by the reaction of the smooth muscle cells, is much faster than vasodilatation, which is caused by other types of slow-response cells in the blood vessel wall.[149, 154]

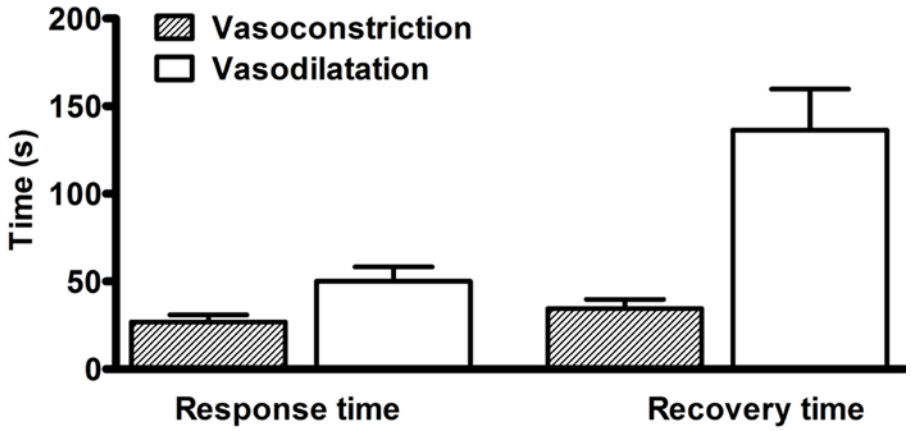

Fig. 41. Temporal characteristics of vasoconstriction (9 vessels) and vasodilatation (15 vessels). The response (rising/falling) time and recovery time of vasodilatation are compared with those of vasoconstriction, using the 1-tailed Wilcoxon Signed Rank Test. The response and recovery times of vasodilatation are statistically significantly longer than those of vasoconstriction (*p* values for both response and recovery cases are 0.005).

Responses of individual microvessels in a mouse cortex to intracortical electrical stimulation were studied with OR-PAM. The relatively small fluctuation (±10%) in the baseline vessel diameter during each OR-PAM monitoring suggested that the neurovascular system remained at a resting state under consistent physiological conditions (Fig. 39). However, this balance could be broken down by electrical-

stimulation-induced vasoconstriction or vasodilatation, depending on stimulation intensity and other factors.

The dual reaction of some vessels to electrical stimulation suggests that vasoconstriction and vasodilatation result from different cellular regulations, which is consistent with the literature.[150] The distinct spatial characteristics of vasoconstriction and vasodilatation (Fig. 40) suggest that vasoconstriction may be due to the direct stimulation of smooth muscle cells and thus decays rapidly with increased distance from the stimulation source, while vasodilatation mainly may result from metabolic regulation and shows a much weaker spatial dependence. The pronounced difference between the temporal features of vasoconstriction and vasodilatation (Fig. 41) reflects the different underlying mechanisms: vasoconstriction, caused by direct electrical stimulation of smooth muscle cells, is related to mechanical features of vessel walls and can be executed in a short time,[143, 155] while vasodilatation, caused by the various neurotransmitters and neuromodulators, may take longer because of the relatively slow transmission speed of neuromodulator signals.

2.4 Conclusion

In summary, label-free OR-PAM was used to the spatial-temporal characteristics and current dependence of the microvascular response to cortical electrical stimulation. The high spatial resolution enables analyzing single vessel responses, and the large FOV allows simultaneous imaging of multiple microvessels for studying correlation and performing statistical analysis. OR-PAM is a promising tool for *in vivo* studies of neurovascular coupling at the microscopic level.

3. Longitudinal transcranial monitoring of ischemic stroke*

Ischemic stroke refers to the death of brain tissue resulting from an inadequate supply of blood and oxygen due to blockage of a major artery. As a result of ischemic stroke, the affected area of the brain is unable to function properly, which may lead to body paralysis, communication difficulty, or vision impairment. A major obstacle in understanding the underlying mechanism of stroke is the lack of an imaging tool to noninvasively or minimally invasively monitor cerebral hemodynamics, covering the entire span of the stroke period.

As a preliminary study, transcranial OR-PAM longitudinally imaged the microvasculature and the vessel-by-vessel sO_2 in an adult Swiss Webster mouse subject to a 40-min MCA occlusion (Fig. 42). OR-PAM observed that, during 40-min MCA occlusion, the average sO_2 within arteries and veins dropped ~20% and ~45%, respectively. After reperfusion, the vessel sO_2 recovered back to normal values. In contrast, the regional oxygen extraction fraction increased 41% during MCA occlusion, indicating that the stroke tissue was oxygen-starving (Table 5).

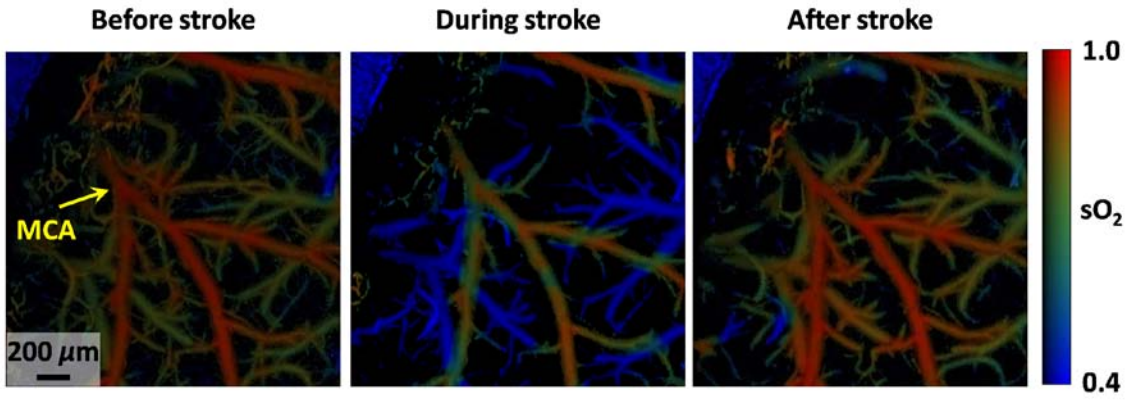

Fig. 42. Longitudinal OR-PAM of MCA-occlusion-induced cerebral sO_2 changes.

* S. Hu et. al., Preliminary data.

Table 5. Functional changes in cortical vasculature due to 40-min MCA occlusion.

	Before (%)	During (%)	After (%)
Average arterial sO_2	93	76	91
Average venous sO_2	72	27	73
Oxygen extraction fraction	23	64	20

Future study will focus on longitudinal, transcranial monitoring of morphological (i.e., vessel diameter) and functional (i.e., HbT, sO_2, and blood flow) changes in cortical vessels due to ischemic stroke induction. It will provide the unprecedented ability to study the intrinsic tissue mechanisms of ischemic brain injury and explore more effective neuroprotective therapies.

V. CONCLUSIONS AND PERSPECTIVES*

OR-PAM has potentially broad applications in biomedical imaging, yet much effort still needs to be invested to mature this technology. Three potential directions of future OR-PAM development are anticipated:

- Optical detection of photoacoustic waves. Current acoustic detection in OR-PAM is based on piezoelectric transducers, which require good tissue contact and generally involve water in acoustic coupling. This configuration leads to system complexity and experimental inconvenience. Moreover, the detection sensitivity of the transducer falls off with its element size. Higher detection frequency is achieved at the expense of SNR. To overcome these limitations, noncontact optical methods for ultrasonic detection need to be explored.
- Integrating OR-PAM with AR-PAM for multi-scale imaging. As shown in Fig. 1, OR-PAM and AR-PAM are highly complementary in terms of spatial resolution and tissue penetration. Combining them together would enable users to select an optimal trade-off between the spatial resolution and the penetration depth for different applications.
- Integrating OR-PAM with multiphoton fluorescence microscopy for neurovascular imaging. OR-PAM and multiphoton microscopy have similar penetration depths in soft brain tissues.[5] Combining them would enable direct visualization of the interaction between neuron activities and vascular dynamics.

* Modified with permission from S. Hu, K. Maslov, and L. V. Wang, "Three-dimensional optical-resolution photoacoustic microscopy," in *Biomedical Optical Imaging Techniques: Design and Applications*, J. M. Zavislan and R. Liang, Ed., Springer (under review).

Being one of the most actively studied optical microscopy technologies, OR-PAM has experienced a dramatic development within the last few years. We are looking forward to seeing OR-PAM in the mainstream.

REFERENCES

1. S. Hu and L. V. Wang, "Photoacoustic imaging and characterization of the microvasculature," J. Biomed. Opt. 15(1), 011101 (2010).
2. K. Maslov, G. Stoica and L. V. Wang, "In vivo dark-field reflection-mode photoacoustic microscopy," Opt. Lett. 30(6), 625-627 (2005).
3. H. F. Zhang, K. Maslov, G. Stoica and L. V. Wang, "Functional photoacoustic microscopy for high-resolution and noninvasive in vivo imaging," Nat. Biotechnol. 24(7), 848-851 (2006).
4. K. Maslov, H. F. Zhang, S. Hu and L. V. Wang, "Optical-resolution photoacoustic microscopy for in vivo imaging of single capillaries," Opt. Lett. 33(9), 929-931 (2008).
5. S. Hu, K. Maslov, V. Tsytsarev and L. V. Wang, "Functional transcranial brain imaging by optical-resolution photoacoustic microscopy," J. Biomed. Opt. 14(4), 040503 (2009).
6. S. Hu, K. Maslov and L. V. Wang, "In vivo functional chronic imaging of a small animal model using optical-resolution photoacoustic microscopy," Med. Phys. 36(6), 2320-2323 (2009).
7. S. Hu, K. Maslov and L. V. Wang, "Noninvasive label-free imaging of microhemodynamics by optical-resolution photoacoustic microscopy," Opt. Express 17(9), 7688-7693 (2009).
8. S. Hu, B. Rao, K. Maslov and L. V. Wang, "Label-free Photoacoustic Ophthalmic Angiography," Opt. Lett. 35(1), 1-3 (2010).
9. S. Hu and L. V. Wang, "Neurovascular photoacoustic tomography," Front.

Neuroenerg. 2(10), doi:10.3389/fnene.2010.00010 (2010).

10. S. Hu, P. Yan, K. Maslov, J.-M. Lee and L. V. Wang, "Intravital imaging of amyloid plaques in a transgenic mouse model using optical-resolution photoacoustic microscopy," Opt. Lett. 34(24), 3899-3901 (2009).
11. S. L. Jiao, M. S. Jiang, J. M. Hu, A. Fawzi, Q. F. Zhou, K. K. Shung, C. A. Puliafito and H. F. Zhang, "Photoacoustic ophthalmoscopy for in vivo retinal imaging," Opt. Express 18(4), 3967-3972 (2010).
12. J. J. Yao, K. I. Maslov, Y. F. Shi, L. A. Taber and L. H. V. Wang, "In vivo photoacoustic imaging of transverse blood flow by using Doppler broadening of bandwidth," Opt. Lett. 35(9), 1419-1421 (2010).
13. V. Tsytsarev, S. Hu, J. Yao, K. Maslov, D. L. Barbour and L. V. Wang, "Photoacoustic microscopy of microvascular responses to cortical electrical stimulation," J. Biomed. Opt. (under review).
14. A. A. Oraevsky and A. A. Karabutov, "Optoacoustic Tomography," in *Biomedical Photonics Handbook* T. Vo-Dinh, Ed., CRC Press, New York (2003).
15. H. F. Zhang, K. Maslov and L. V. Wang, "In vivo imaging of subcutaneous structures using functional photoacoustic microscopy," Nat. Protoc. 2(4), 797-804 (2007).
16. A. C. Guyton and J. E. Hall, Textbook of medical physiology, Saunders, Philadelphia (2000).
17. S. Basu, J. A. Nagy, S. Pal, E. Vasile, I. A. Eckelhoefer, V. S. Bliss, E. J. Manseau, P. S. Dasgupta, H. F. Dvorak and D. Mukhopadhyay, "The neurotransmitter dopamine inhibits angiogenesis induced by vascular permeability factor/vascular endothelial growth factor," Nat. Med. 7(5), 569-574 (2001).

18. D. A. Elson, G. Thurston, L. E. Huang, D. G. Ginzinger, D. M. McDonald, R. S. Johnson and J. M. Arbeit, "Induction of hypervascularity without leakage or inflammation in transgenic mice overexpressing hypoxia-inducible factor-1alpha," Genes. Dev. 15(19), 2520-2532 (2001).

19. V. P. Zharov, E. I. Galanzha, E. V. Shashkov, N. G. Khlebtsov and V. V. Tuchin, "In vivo photoacoustic flow cytometry for monitoring of circulating single cancer cells and contrast agents," Opt. Lett. 31(24), 3623-3625 (2006).

20. M. L. Li, J. T. Oh, X. Y. Xie, G. Ku, W. Wang, C. Li, G. Lungu, G. Stoica and L. V. Wang, "Simultaneous molecular and hypoxia imaging of brain tumors in vivo using spectroscopic photoacoustic tomography," Proc. IEEE 96(3), 481-489 (2008).

21. "Laser Institute of America, American National Standard for Safe Use of Lasers ANSI Z136.1–2000," American National Standards Institute Inc., New York, NY (2000).

22. L. E. Kinsler, Fundamentals of acoustics, Wiley, New York (2000).

23. L. M. Brekhovskikh, Waves in layered media, Academic Press, New York (1980).

24. M. D. Stern, "In vivo evaluation of microcirculation by coherent light scattering," Nature 254(5495), 56-58 (1975).

25. J. E. Tooke, "Microvasculature in diabetes," Cardiovasc. Res. 32(4), 764-771 (1996).

26. B. I. Levy, G. Ambrosio, A. R. Pries and H. A. Struijker-Boudier, "Microcirculation in hypertension: a new target for treatment?," Circulation 104(6), 735-740 (2001).

27. O. Bongard, H. Bounameaux and B. Fagrell, "Effects of oxygen inhalation on skin microcirculation in patients with peripheral arterial occlusive disease," Circulation 86(3), 878-886 (1992).

28. D. M. McDonald and P. Baluk, "Significance of blood vessel leakiness in cancer," Cancer Res. 62(18), 5381-5385 (2002).

29. L. Kuo, M. J. Davis, M. S. Cannon and W. M. Chilian, "Pathophysiological Consequences of Atherosclerosis Extend into the Coronary Microcirculation - Restoration of Endothelium-Dependent Responses by L-Arginine," Circulation Res. 70(3), 465-476 (1992).

30. D. Hasdai, R. J. Gibbons, D. R. Holmes, Jr., S. T. Higano and A. Lerman, "Coronary endothelial dysfunction in humans is associated with myocardial perfusion defects," Circulation 96(10), 3390-3395 (1997).

31. C. Iadecola, "Neurovascular regulation in the normal brain and in Alzheimer's disease," Nat. Rev. Neurosci. 5(5), 347-360 (2004).

32. D. M. McDonald and P. L. Choyke, "Imaging of angiogenesis: from microscope to clinic," Nat. Med. 9(6), 713-725 (2003).

33. A. M. Iga, S. Sarkar, K. M. Sales, M. C. Winslet and A. M. Seifalian, "Quantitating therapeutic disruption of tumor blood flow with intravital video microscopy," Cancer Res. 66(24), 11517-11519 (2006).

34. E. Laemmel, M. Genet, G. Le Goualher, A. Perchant, J. F. Le Gargasson and E. Vicaut, "Fibered confocal fluorescence microscopy (Cell-viZio) facilitates extended imaging in the field of microcirculation. A comparison with intravital microscopy," J. Vasc. Res. 41(5), 400-411 (2004).

35. D. Kleinfeld, P. P. Mitra, F. Helmchen and W. Denk, "Fluctuations and stimulus-induced changes in blood flow observed in individual capillaries in layers 2 through 4 of rat neocortex," Proc. Natl. Acad. Sci. 95(26), 15741-15746 (1998).

36. M. C. Pierce, D. J. Javier and R. Richards-Kortum, "Optical contrast agents and imaging systems for detection and diagnosis of cancer," Int. J. Cancer. 123(9), 1979-1990 (2008).

37. W. Groner, J. W. Winkelman, A. G. Harris, C. Ince, G. J. Bouma, K. Messmer and R. G. Nadeau, "Orthogonal polarization spectral imaging: a new method for study of the microcirculation," Nat. Med. 5(10), 1209-1212 (1999).

38. A. Bauer, S. Kofler, M. Thiel, S. Eifert and F. Christ, "Monitoring of the sublingual microcirculation in cardiac surgery using orthogonal polarization spectral imaging: preliminary results," Anesthesiology 107(6), 939-945 (2007).

39. H. F. Zhang, K. Maslov, G. Stoica and L. V. Wang, "Functional photoacoustic microscopy for high-resolution and noninvasive in vivo imaging," Nat. Biotechnol. 24(7), 848-851 (2006).

40. H. F. Zhang, K. Maslov and L. V. Wang, "In vivo imaging of subcutaneous structures using functional photoacoustic microscopy," Nat. Protoc. 2(4), 797-804 (2007).

41. K. Maslov, H. F. Zhang, S. Hu and L. V. Wang, "Optical-resolution photoacoustic microscopy for in vivo imaging of single capillaries," Opt. Lett. 33(9), 929-931 (2008).

42. C. Aalkaer and H. Nilsson, "Vasomotion: cellular background for the oscillator and for the synchronization of smooth muscle cells," Br. J. Pharmacol. 144(5), 605-616 (2005).

43. G. O. von Mering, C. B. Arant, T. R. Wessel, S. P. McGorray, C. N. Bairey Merz, B. L. Sharaf, K. M. Smith, M. B. Olson, B. D. Johnson, G. Sopko, E. Handberg, C. J. Pepine and R. A. Kerensky, "Abnormal coronary vasomotion as a prognostic

indicator of cardiovascular events in women: results from the National Heart, Lung, and Blood Institute-Sponsored Women's Ischemia Syndrome Evaluation (WISE)," Circulation 109(6), 722-725 (2004).

44. H. Nilsson and C. Aalkjaer, "Vasomotion: mechanisms and physiological importance," Mol. Interv. 3(2), 79-89, 51 (2003).

45. S. Bertuglia, A. Colantuoni, G. Coppini and M. Intaglietta, "Hypoxia- or hyperoxia-induced changes in arteriolar vasomotion in skeletal muscle microcirculation," Am. J. Physiol. 260(2 Pt 2), H362-372 (1991).

46. K. Lorentz, A. Zayas-Santiago, S. Tummala and J. J. Derwent, "Scanning laser ophthalmoscope-particle tracking method to assess blood velocity during hypoxia and hyperoxia," Adv. Exp. Med. Biol. 614(253-261 (2008).

47. L. V. Wang, "Prospects of photoacoustic tomography," Med. Phys. 35(12), 5758-5767 (2008).

48. H. Fang, K. Maslov and L. V. Wang, "Photoacoustic Doppler effect from flowing small light-absorbing particles," Phys. Rev. Lett. 99(18), 184501 (2007).

49. R. K. Jain, L. L. Munn and D. Fukumura, "Dissecting tumour pathophysiology using intravital microscopy," Nat. Rev. Cancer 2(4), 266-276 (2002).

50. D. Fukumura and R. K. Jain, "Imaging angiogenesis and the microenvironment," APMIS 116(7-8), 695-715 (2008).

51. K. Deisseroth, G. Feng, A. K. Majewska, G. Miesenbock, A. Ting and M. J. Schnitzer, "Next-generation optical technologies for illuminating genetically targeted brain circuits," J. Neurosci. 26(41), 10380-10386 (2006).

52. A. Zepeda, C. Arias and F. Sengpiel, "Optical imaging of intrinsic signals: recent

developments in the methodology and its applications," J. Neurosci. Methods 136(1), 1-21 (2004).

53. H. F. Zhang, K. Maslov, M. Sivaramakrishnan, G. Stoica and L. H. V. Wang, "Imaging of hemoglobin oxygen saturation variations in single vessels in vivo using photoacoustic microscopy," Appl. Phys. Lett. 90(5), 3 (2007).

54. D. Malonek and A. Grinvald, "Interactions between electrical activity and cortical microcirculation revealed by imaging spectroscopy: implications for functional brain mapping," Science 272(5261), 551-554 (1996).

55. R. R. Anderson and J. A. Parrish, "Selective photothermolysis: precise microsurgery by selective absorption of pulsed radiation," Science 220(4596), 524-527 (1983).

56. A. F. Falabella and R. S. Kirsner, Wound Healing Talyor & Francis, Boca Raton (2005).

57. S. A. Masino and R. D. Frostig, "Quantitative long-term imaging of the functional representation of a whisker in rat barrel cortex," Proc. Natl. Acad. Sci. 93(10), 4942-4947 (1996).

58. X. Wang, Y. Pang, G. Ku, X. Xie, G. Stoica and L. V. Wang, "Noninvasive laser-induced photoacoustic tomography for structural and functional in vivo imaging of the brain," Nat. Biotechnol. 21(7), 803-806 (2003).

59. A. Grinvald and R. Hildesheim, "VSDI: a new era in functional imaging of cortical dynamics," Nat. Rev. Neurosci. 5(11), 874-885 (2004).

60. R. D. Frostig, E. E. Lieke, D. Y. Ts'o and A. Grinvald, "Cortical functional architecture and local coupling between neuronal activity and the microcirculation revealed by in vivo high-resolution optical imaging of intrinsic signals," Proc. Natl.

Acad. Sci. 87(16), 6082-6086 (1990).

61. R. K. Wang, S. L. Jacques, Z. Ma, S. Hurst, S. R. Hanson and A. Gruber, "Three dimensional optical angiography," Opt. Express 15(7), 4083-4097 (2007).

62. E. W. Stein, K. Maslov and L. V. Wang, "Noninvasive, in vivo imaging of blood-oxygenation dynamics within the mouse brain using photoacoustic microscopy," J. Biomed. Opt. 14(2), 020502 (2009).

63. K. Maslov, H. F. Zhang, S. Hu and L. V. Wang, "Optical-resolution confocal photoacoustic microscopy," Proc. SPIE 6856 (2008).

64. E. M. Hillman, A. Devor, M. B. Bouchard, A. K. Dunn, G. W. Krauss, J. Skoch, B. J. Bacskai, A. M. Dale and D. A. Boas, "Depth-resolved optical imaging and microscopy of vascular compartment dynamics during somatosensory stimulation," Neuroimage 35(1), 89-104 (2007).

65. X. Wang, X. Xie, G. Ku, L. V. Wang and G. Stoica, "Noninvasive imaging of hemoglobin concentration and oxygenation in the rat brain using high-resolution photoacoustic tomography," J. Biomed. Opt. 11(2), 024015 (2006).

66. A. B. W. G. Zijlstra, and O. W. van Assendelft, Visible and Near Infrared Absorption Spectra of Human and Animal Hemoglobin, Determination and Application, VSP, Amsterdam, The Netherlands (2000).

67. H. Kobayashi and N. Takizawa, "Oxygen saturation and pH changes in cremaster microvessels of the rat," Am. J. Physiol. 270, H1453-1461 (1996).

68. A. G. Tsai, P. C. Johnson and M. Intaglietta, "Oxygen gradients in the microcirculation," Physiol. Rev. 83(3), 933-963 (2003).

69. E. Vovenko, "Distribution of oxygen tension on the surface of arterioles, capillaries

and venules of brain cortex and in tissue in normoxia: an experimental study on rats," Pflugers Arch. 437(4), 617-623 (1999).

70. X. Wang, D. L. Chamberland and G. Xi, "Noninvasive reflection mode photoacoustic imaging through infant skull toward imaging of neonatal brains," J. Neurosci. Methods 168(2), 412-421 (2008).

71. J. Laufer, D. Delpy, C. Elwell and P. Beard, "Quantitative spatially resolved measurement of tissue chromophore concentrations using photoacoustic spectroscopy: application to the measurement of blood oxygenation and haemoglobin concentration,"Phys. Med. Biol. 52(1), 141-168 (2007).

72. F. Helmchen and W. Denk, "Deep tissue two-photon microscopy," Nat. Methods 2(12), 932-940 (2005).

73. "Summary Health Statistics for U.S. Adults: National Health Interview Survey," (2007).

74. L. P. Aiello, R. L. Avery, P. G. Arrigg, B. A. Keyt, H. D. Jampel, S. T. Shah, L. R. Pasquale, H. Thieme, M. A. Iwamoto, J. E. Park and et al., "Vascular endothelial growth factor in ocular fluid of patients with diabetic retinopathy and other retinal disorders," New. Engl. J. Med. 331(22), 1480-1487 (1994).

75. B. R. Hurley and C. D. Regillo, Fluorescein Angiography: General Principles and Interpretation in Retinal Angiography and Optical Coherence Tomography (ed. J. Fernando Arevalo), Springer, New York (2009).

76. "Laser Institute of America, American National Standard for Safe Use of Lasers ANSI Z136.1–2007," American National Standards Institute Inc., New York, NY (2007).

77. Z. Xie, S. Jiao, H. F. Zhang and C. A. Puliafito, "Laser-scanning optical-resolution photoacoustic microscopy," Opt. Lett. 34(12), 1771-1773 (2009).

78. J. A. Nagy, S. C. Shih, W. H. Wong, A. M. Dvorak and H. F. Dvorak, "Chapter 3. The adenoviral vector angiogenesis/lymphangiogenesis assay," Methods Enzymol. 444, 43-64 (2008).

79. M. Grunewald, I. Avraham, Y. Dor, E. Bachar-Lustig, A. Itin, S. Jung, S. Chimenti, L. Landsman, R. Abramovitch and E. Keshet, "VEGF-induced adult neovascularization: recruitment, retention, and role of accessory cells," Cell 124(1), 175-189 (2006).

80. T. L. Phung, K. Ziv, D. Dabydeen, G. Eyiah-Mensah, M. Riveros, C. Perruzzi, J. Sun, R. A. Monahan-Earley, I. Shiojima, J. A. Nagy, M. I. Lin, K. Walsh, A. M. Dvorak, D. M. Briscoe, M. Neeman, W. C. Sessa, H. F. Dvorak and L. E. Benjamin, "Pathological angiogenesis is induced by sustained Akt signaling and inhibited by rapamycin," Cancer Cell 10(2), 159-170 (2006).

81. P. Yan, A. W. Bero, J. R. Cirrito, Q. Xiao, X. Hu, Y. Wang, E. Gonzales, D. M. Holtzman and J. M. Lee, "Characterizing the appearance and growth of amyloid plaques in APP/PS1 mice," J. Neurosci. 29(34), 10706-10714 (2009).

82. B. J. Vakoc, R. M. Lanning, J. A. Tyrrell, T. P. Padera, L. A. Bartlett, T. Stylianopoulos, L. L. Munn, G. J. Tearney, D. Fukumura, R. K. Jain and B. E. Bouma, "Three-dimensional microscopy of the tumor microenvironment in vivo using optical frequency domain imaging," Nat. Med. 15(10), 1219-1223 (2009).

83. E. B. Rankin and A. J. Giaccia, "The role of hypoxia-inducible factors in tumorigenesis," Cell Death Differ. 15(4), 678-685 (2008).

84. C. J. Schofield and P. J. Ratcliffe, "Signalling hypoxia by HIF hydroxylases,"

Biochem. Biophys. Res. Commun. 338(1), 617-626 (2005).

85. G. L. Semenza, "Targeting HIF-1 for cancer therapy," Nat. Rev. Cancer 3(10), 721-732 (2003).

86. M. M. Hickey and M. C. Simon, "Regulation of angiogenesis by hypoxia and hypoxia-inducible factors," Curr. Top. Dev. Biol. 76(217-257 (2006).

87. N. Tang, L. Wang, J. Esko, F. J. Giordano, Y. Huang, H. P. Gerber, N. Ferrara and R. S. Johnson, "Loss of HIF-1alpha in endothelial cells disrupts a hypoxia-driven VEGF autocrine loop necessary for tumorigenesis," Cancer Cell 6(5), 485-495 (2004).

88. R. Du, K. V. Lu, C. Petritsch, P. Liu, R. Ganss, E. Passegue, H. Song, S. Vandenberg, R. S. Johnson, Z. Werb and G. Bergers, "HIF1alpha induces the recruitment of bone marrow-derived vascular modulatory cells to regulate tumor angiogenesis and invasion," Cancer Cell 13(3), 206-220 (2008).

89. J. Arbeit, "Transgenic models of epidermal neoplasia and multi-stage carcinogenesis," Cancer Surveys 26, 7-34 (1996).

90. Y. P. Xia, B. Li, D. Hylton, M. Detmar, G. D. Yancopoulos and J. S. Rudge, "Transgenic delivery of VEGF to mouse skin leads to an inflammatory condition resembling human psoriasis," Blood 102(1), 161-168 (2003).

91. G. Thurston, C. Suri, K. Smith, J. McClain, T. N. Sato, G. D. Yancopoulos and D. M. McDonald, "Leakage-resistant blood vessels in mice transgenically overexpressing angiopoietin-1," Science 286(5449), 2511-2514 (1999).

92. L. Dan, Y. Shi-long, L. Miao-li, L. Yong-ping, M. Hong-jie, Z. Ying and W. Xiang-gui, "Inhibitory effect of oral doxycycline on neovascularization in a rat corneal alkali burn model of angiogenesis," Curr. Eye Res. 33(8), 653-660 (2008).

93. I. Diamond, T. Owolabi, M. Marco, C. Lam and A. Glick, "Conditional gene expression in the epidermis of transgenic mice using the tetracycline-regulated transactivators tTA and rTA linked to the keratin 5 promoter," J. Invest. Dermatol. 115(5), 788-794 (2000).

94. S. Hu, K. Maslov and L. V. Wang, "Noninvasive label-free imaging of microhemodynamics by optical-resolution photoacoustic microscopy," Opt. Express 17(9), 7688-7693 (2009).

95. K. Gaengel, G. Genove, A. Armulik and C. Betsholtz, "Endothelial-mural cell signaling in vascular development and angiogenesis," Arterioscler. Thromb. Vasc. Biol. 29(5), 630-638 (2009).

96. L. E. Benjamin, I. Hemo and E. Keshet, "A plasticity window for blood vessel remodelling is defined by pericyte coverage of the preformed endothelial network and is regulated by PDGF-B and VEGF," Development 125(9), 1591-1598 (1998).

97. G. Bergers and S. Song, "The role of pericytes in blood-vessel formation and maintenance," Neuro. Oncol. 7(4), 452-464 (2005).

98. K. R. Laderoute, R. M. Alarcon, M. D. Brody, J. M. Calaoagan, E. Y. Chen, A. M. Knapp, Z. Yun, N. C. Denko and A. J. Giaccia, "Opposing effects of hypoxia on expression of the angiogenic inhibitor thrombospondin 1 and the angiogenic inducer vascular endothelial growth factor," Clin. Cancer Res. 6(7), 2941-2950 (2000).

99. M. Duval, S. Bedard-Goulet, C. Delisle and J. P. Gratton, "Vascular endothelial growth factor-dependent down-regulation of Flk-1/KDR involves Cbl-mediated ubiquitination. Consequences on nitric oxide production from endothelial cells," J. Biol. Chem. 278(22), 20091-20097 (2003).

100. B. Olszewska-Pazdrak, T. W. Hein, P. Olszewska and D. H. Carney, "Chronic hypoxia attenuates VEGF signaling and angiogenic responses by downregulation of KDR in human endothelial cells," Am. J. Physiol. Cell Physiol. 296(5), C1162-1170 (2009).

101. B. Q. Shen, D. Y. Lee, H. P. Gerber, B. A. Keyt, N. Ferrara and T. F. Zioncheck, "Homologous up-regulation of KDR/Flk-1 receptor expression by vascular endothelial growth factor in vitro," J. Biol. Chem. 273(45), 29979-29985 (1998).

102. L. Witte, D. J. Hicklin, Z. Zhu, B. Pytowski, H. Kotanides, P. Rockwell and P. Bohlen, "Monoclonal antibodies targeting the VEGF receptor-2 (Flk1/KDR) as an anti-angiogenic therapeutic strategy," Cancer Metastasis Rev. 17(2), 155-161 (1998).

103. Y. Wu, Z. Zhong, J. Huber, R. Bassi, B. Finnerty, E. Corcoran, H. Li, E. Navarro, P. Balderes, X. Jimenez, H. Koo, V. R. Mangalampalli, D. L. Ludwig, J. R. Tonra and D. J. Hicklin, "Anti-vascular endothelial growth factor receptor-1 antagonist antibody as a therapeutic agent for cancer," Clin. Cancer Res. 12(21), 6573-6584 (2006).

104. C. Murdoch, A. Giannoudis and C. E. Lewis, "Mechanisms regulating the recruitment of macrophages into hypoxic areas of tumors and other ischemic tissues," Blood 104(8), 2224-2234 (2004).

105. G. Bergers and D. Hanahan, "Modes of resistance to anti-angiogenic therapy," Nat. Rev. Cancer 8(8), 592-603 (2008).

106. M. A. Moore, K. Hattori, B. Heissig, J. H. Shieh, S. Dias, R. G. Crystal and S. Rafii, "Mobilization of endothelial and hematopoietic stem and progenitor cells by adenovector-mediated elevation of serum levels of SDF-1, VEGF, and angiopoietin-1," Ann. N. Y. Acad. Sci. 938, 36-45; discussion 45-37 (2001).

107. D. J. Ceradini, A. R. Kulkarni, M. J. Callaghan, O. M. Tepper, N. Bastidas, M. E. Kleinman, J. M. Capla, R. D. Galiano, J. P. Levine and G. C. Gurtner, "Progenitor cell trafficking is regulated by hypoxic gradients through HIF-1 induction of SDF-1," Nat. Med. 10(8), 858-864 (2004).

108. S. Mukherjee, M. Tessema and A. Wandinger-Ness, "Vesicular trafficking of tyrosine kinase receptors and associated proteins in the regulation of signaling and vascular function," Circ. Res. 98(6), 743-756 (2006).

109. A. J. Singh, R. D. Meyer, H. Band and N. Rahimi, "The carboxyl terminus of VEGFR-2 is required for PKC-mediated down-regulation," Mol. Biol. Cell 16(4), 2106-2118 (2005).

110. L. Labrecque, I. Royal, D. S. Surprenant, C. Patterson, D. Gingras and R. Beliveau, "Regulation of vascular endothelial growth factor receptor-2 activity by caveolin-1 and plasma membrane cholesterol," Mol. Biol. Cell 14(1), 334-347 (2003).

111. M. G. Lampugnani, F. Orsenigo, M. C. Gagliani, C. Tacchetti and E. Dejana, "Vascular endothelial cadherin controls VEGFR-2 internalization and signaling from intracellular compartments," J. Cell Biol. 174(4), 593-604 (2006).

112. R. Bhattacharya, N. Kang-Decker, D. A. Hughes, P. Mukherjee, V. Shah, M. A. McNiven and D. Mukhopadhyay, "Regulatory role of dynamin-2 in VEGFR-2/KDR-mediated endothelial signaling," FASEB J. 19(12), 1692-1694 (2005).

113. V. G. Gorgoulis, L. V. Vassiliou, P. Karakaidos, P. Zacharatos, A. Kotsinas, T. Liloglou, M. Venere, R. A. Ditullio, Jr., N. G. Kastrinakis, B. Levy, D. Kletsas, A. Yoneta, M. Herlyn, C. Kittas and T. D. Halazonetis, "Activation of the DNA damage checkpoint and genomic instability in human precancerous lesions," Nature

434(7035), 907-913 (2005).

114. J. S. Dickey, C. E. Redon, A. J. Nakamura, B. J. Baird, O. A. Sedelnikova and W. M. Bonner, "H2AX: functional roles and potential applications," Chromosoma 118(6), 683-692 (2009).

115. M. Economopoulou, H. F. Langer, A. Celeste, V. V. Orlova, E. Y. Choi, M. Ma, A. Vassilopoulos, E. Callen, C. Deng, C. H. Bassing, M. Boehm, A. Nussenzweig and T. Chavakis, "Histone H2AX is integral to hypoxia-driven neovascularization," Nat. Med. 15(5), 553-558 (2009).

116. K. K. To, O. A. Sedelnikova, M. Samons, W. M. Bonner and L. E. Huang, "The phosphorylation status of PAS-B distinguishes HIF-1alpha from HIF-2alpha in NBS1 repression," EMBO J. 25(20), 4784-4794 (2006).

117. A. Uemura, S. Kusuhara, H. Katsuta and S. Nishikawa, "Angiogenesis in the mouse retina: a model system for experimental manipulation," Exp. Cell Res. 312(5), 676-683 (2006).

118. U. Ozerdem and W. B. Stallcup, "Early contribution of pericytes to angiogenic sprouting and tube formation," Angiogenesis 6(3), 241-249 (2003).

119. S. Morikawa, P. Baluk, T. Kaidoh, A. Haskell, R. K. Jain and D. M. McDonald, "Abnormalities in pericytes on blood vessels and endothelial sprouts in tumors," Am. J. Pathol. 160(3), 985-1000 (2002).

120. V. Nehls, K. Denzer and D. Drenckhahn, "Pericyte involvement in capillary sprouting during angiogenesis in situ," Cell Tissue Res. 270(3), 469-474 (1992).

121. J. Andrae, R. Gallini and C. Betsholtz, "Role of platelet-derived growth factors in physiology and medicine," Genes. Dev. 22(10), 1276-1312 (2008).

122. K. Hattori, S. Dias, B. Heissig, N. R. Hackett, D. Lyden, M. Tateno, D. J. Hicklin, Z. Zhu, L. Witte, R. G. Crystal, M. A. Moore and S. Rafii, "Vascular endothelial growth factor and angiopoietin-1 stimulate postnatal hematopoiesis by recruitment of vasculogenic and hematopoietic stem cells," J. Exp. Med. 193(9), 1005-1014 (2001).

123. S. P. Dineen, K. D. Lynn, S. E. Holloway, A. F. Miller, J. P. Sullivan, D. S. Shames, A. W. Beck, C. C. Barnett, J. B. Fleming and R. A. Brekken, "Vascular endothelial growth factor receptor 2 mediates macrophage infiltration into orthotopic pancreatic tumors in mice," Cancer Res. 68(11), 4340-4346 (2008).

124. M. De Palma, M. A. Venneri, R. Galli, L. Sergi Sergi, L. S. Politi, M. Sampaolesi and L. Naldini, "Tie2 identifies a hematopoietic lineage of proangiogenic monocytes required for tumor vessel formation and a mesenchymal population of pericyte progenitors," Cancer Cell 8(3), 211-226 (2005).

125. F. Shojaei, X. Wu, A. K. Malik, C. Zhong, M. E. Baldwin, S. Schanz, G. Fuh, H. P. Gerber and N. Ferrara, "Tumor refractoriness to anti-VEGF treatment is mediated by CD11b+Gr1+ myeloid cells," Nat. Biotechnol. 25(8), 911-920 (2007).

126. L. V. Wang, "Multiscale photoacoustic microscopy and computed tomography," Nat. Photonics 3(9), 503-509 (2009).

127. S. Hu, B. Rao, K. Maslov and L. V. Wang, "Label-free photoacoustic ophthalmic angiography," Opt. Lett. 35(1-3 (2010).

128. R. Bekeredjian, C. B. Walton, K. A. MacCannell, J. Ecker, F. Kruse, J. T. Outten, D. Sutcliffe, R. D. Gerard, R. K. Bruick and R. V. Shohet, "Conditional HIF-1alpha expression produces a reversible cardiomyopathy," PLoS ONE 5(7), e11693 (2010).

129. J. Jonkers, R. Meuwissen, H. van der Gulden, H. Peterse, M. van der Valk and A.

Berns, Nat. Genet. 29(4), 418-425 (2001).

130. H. P. Gerber, K. J. Hillan, A. M. Ryan, J. Kowalski, G. A. Keller, L. Rangell, B. D. Wright, F. Radtke, M. Aguet and N. Ferrara, "VEGF is required for growth and survival in neonatal mice," Development 126(6), 1149-1159 (1999).

131. W. G. Kaelin Jr and P. J. Ratcliffe, "Oxygen Sensing by Metazoans: The Central Role of the HIF Hydroxylase Pathway," Mol. Cell 30(4), 393-402 (2008).

132. J. Kishimoto, R. Ehama, Y. Ge, T. Kobayashi, T. Nishiyama, M. Detmar and R. E. Burgeson, "In vivo detection of human vascular endothelial growth factor promoter activity in transgenic mouse skin," Am. J. Pathol. 157(1), 103-110 (2000).

133. P. B. Morris, T. Hida, P. J. Blackshear, G. K. Klintworth and J. L. Swain, "Tumor-promoting phorbol esters induce angiogenesis in vivo," Am. J. Physiol. 254, C318-322 (1988).

134. M. Scortegagna, C. Cataisson, R. J. Martin, D. J. Hicklin, R. D. Schreiber, S. H. Yuspa and J. M. Arbeit, "HIF-1alpha regulates epithelial inflammation by cell autonomous NFkappaB activation and paracrine stromal remodeling," Blood 111(7), 3343-3354 (2008).

135. C. Wu, V. W. Pike and Y. Wang, "Amyloid imaging: from benchtop to bedside," Curr. Top. Dev. Biol. 70, 171-213 (2005).

136. W. E. Klunk, B. J. Bacskai, C. A. Mathis, S. T. Kajdasz, M. E. McLellan, M. P. Frosch, M. L. Debnath, D. P. Holt, Y. Wang and B. T. Hyman, "Imaging Abeta plaques in living transgenic mice with multiphoton microscopy and methoxy-X04, a systemically administered Congo red derivative," J. Neuropath. Exp. Neur. 61(9), 797-805 (2002).

137. S. Hu, K. Maslov and L. V. Wang, "In vivo functional chronic imaging of a small animal model using optical-resolution photoacoustic microscopy," Med. Phys. 36(6), 2320-2323 (2009).

138. C. L. Nie, X. S. Wang, Y. Liu, S. Perrett and R. Q. He, "Amyloid-like aggregates of neuronal tau induced by formaldehyde promote apoptosis of neuronal cells," BMC Neurosci. 8, 9 (2007).

139. S. L. Jacques and S. A. Prahl, http://omlc.ogi.edu/spectra/hemoglobin/index.html (1998).

140. M. Hintersteiner, A. Enz, P. Frey, A. L. Jaton, W. Kinzy, R. Kneuer, U. Neumann, M. Rudin, M. Staufenbiel, M. Stoeckli, K. H. Wiederhold and H. U. Gremlich, "In vivo detection of amyloid-beta deposits by near-infrared imaging using an oxazine-derivative probe," Nat. Biotechnol. 23(5), 577-583 (2005).

141. H. T. Xu, F. Pan, G. Yang and W. B. Gan, "Choice of cranial window type for in vivo imaging affects dendritic spine turnover in the cortex," Nat. Neurosci. 10(5), 549-551 (2007).

142. N. J. Allen and B. A. Barres, "Neuroscience: Glia - more than just brain glue," Nature 457(7230), 675-677 (2009).

143. M. Y. Inyushin, A. B. Vol'nova and D. N. Lenkov, "Use of a Simplified Method of Optical Recording to Identify Foci of Maximal Neuron Activity in the Somatosensory Cortex of White Rats," Neurosci. Behav. Physiol. 31(2), 201-205 (2001).

144. K. Uludag, D. J. Dubowitz, E. J. Yoder, K. Restom, T. T. Liu and R. B. Buxton, "Coupling of cerebral blood flow and oxygen consumption during physiological activation and deactivation measured with fMRI," Neuroimage 23(1), 148-155 (2004).

145. J. P. Culver, T. Durduran, D. Furuya, C. Cheung, J. H. Greenberg and A. G. Yodh, "Diffuse optical tomography of cerebral blood flow, oxygenation, and metabolism in rat during focal ischemia," J. Cereb. Blood Flow Metab. 23(8), 911-924 (2003).

146. X. Wang, Y. Pang, G. Ku, X. Xie, G. Stoica and L. V. Wang, "Noninvasive laser-induced photoacoustic tomography for structural and functional in vivo imaging of the brain," Nat. Biotechnol. 21(7), 803-806 (2003).

147. L. V. Wang, "Multiscale photoacoustic microscopy and computed tomography," Nat. Photon. 3, 503-509 (2009).

148. E. W. Stein, K. Maslov and L. V. Wang, "Noninvasive, in vivo imaging of blood-oxygenation dynamics within the mouse brain using photoacoustic microscopy," J. Biomed. Opt. 14(2), 020502 (2009).

149. V. Tsytsarev, K. Premachandra, D. Takeshita and S. Bahar, "Imaging cortical electrical stimulation in vivo: fast intrinsic optical signal versus voltage-sensitive dyes," Opt. Lett. 33(9), 1032-1034 (2008).

150. M. R. Metea and E. A. Newman, "Glial cells dilate and constrict blood vessels: a mechanism of neurovascular coupling," J. Neurosci. 26(11), 2862-2870 (2006).

151. M. Zonta, M. C. Angulo, S. Gobbo, B. Rosengarten, K. A. Hossmann, T. Pozzan and G. Carmignoto, "Neuron-to-astrocyte signaling is central to the dynamic control of brain microcirculation," Nat. Neurosci. 6(1), 43-50 (2003).

152. H. F. Zhang, K. Maslov, M. Sivaramakrishnan, G. Stoica and L. H. V. Wang, "Imaging of hemoglobin oxygen saturation variations in single vessels in vivo using photoacoustic microscopy," Appl. Phys. Lett. 90(5), 3 (2007).

153. D. A. Schwinn, R. W. McIntyre and J. G. Reves, "Isoflurane-induced vasodilation:

role of the alpha-adrenergic nervous system," Anesth. Analg. 71(5), 451-459 (1990).

154. B. Cauli, X. K. Tong, A. Rancillac, N. Serluca, B. Lambolez, J. Rossier and E. Hamel, "Cortical GABA interneurons in neurovascular coupling: relays for subcortical vasoactive pathways," J. Neurosci. 24(41), 8940-8949 (2004).

155. L. Leybaert, "Neurobarrier coupling in the brain: a partner of neurovascular and neurometabolic coupling?," J. Cereb. Blood Flow Metab. 25(1), 2-16 (2005).

VITA

Song Hu received his B.S. and M.S. in the Department of Electronic Engineering from Tsinghua University, China, in 2002 and 2005, respectively. In Fall 2005, he started to pursue his Ph.D. in the Department of Electrical Engineering at University of Southern California and transferred to the Department of Biomedical Engineering at Washington University in St. Louis in Fall 2006. His research topics included photoacoustic imaging, optical coherence tomography, tissue optics, and their applications in vascular biology, dermatology, and neurology. He received his Ph.D. in Biomedical Engineering at Washington University in St. Louis in December 2010.

Song Hu

Department of Biomedical Engineering

Washington University in St. Louis

One Brookings Dr. St. Louis, MO 63130

Tel: 314-935-4911

Fax: 314-935-7448

Email: shu@biomed.wustl.edu